

**Composite Inorganic Membranes for Gas Separations:  
Chemical Vapor Deposition of Hydrogen Permselective Oxide  
Membranes and Preparation of Supported Zeolite NaA Films**

Thesis by  
Michael Tsapatsis

*In Partial Fulfillment of the Requirements  
for the Degree of  
Doctor of Philosophy*

California Institute of Technology

Pasadena, California

1994

(Defended January 10, 1994)

ia

στην Χαρούλα

## Acknowledgments

It is with my deepest appreciation that I acknowledge my advisor, Professor George Gavalas for his thoughtful suggestions and steady encouragement. Daily interaction with him greatly enriched my graduate education. His patience and support during difficult moments are greatly appreciated.

I would like to thank Professor Mark Davis for treating me as a member of his group and introducing me to a fascinating area of research. I am looking forward to our future interaction.

During these four years at Caltech many people have helped me through discussion, criticism and experimental assistance. I thank Dr. S.W. Nam for his help at the early stages of this work, Dr. S. Kim for useful discussions and assistance, Professors Flagan and Giapis for interesting suggestions, Chick Nakawatasse for assistance in setting up the experimental system, Gabor Faludi for excellent glassblowing and Donna Johnson for always offering me a helping hand in numerous tasks. I am indebted to Paul Carpenter and Carol Garland for their assistance in the microscope labs. For their interest and help in my professional growth I thank Professors Gavalas, Bailey, Davis, Flagan and Giapis.

I gratefully acknowledge the California Institute of Technology, the Department of Energy, the National Science Foundation and the North American Membrane Society for financial support.

I would like to express my deepest gratitude to my close friends Jeff Morris, Edye Udell and Professor Nick Panagiotacopulos and his family for their love and support.

I have the luck to be part of a wonderful family which I thank for the understanding and constant support.

This work is dedicated to the memory of my wife and fellow graduate student, Chariklia Economou. Chara was the joy of my life for ten years and made everything possible with her love, support and understanding.

## Abstract

Hydrogen-perselective membranes were synthesized by chemical vapor deposition of SiO<sub>2</sub>, TiO<sub>2</sub>, Al<sub>2</sub>O<sub>3</sub>, and B<sub>2</sub>O<sub>3</sub> layers within the pores of Vycor tubes. The deposition involved reaction of SiCl<sub>4</sub>, etc., with water at 100-800 °C depending on the chloride and the reaction geometry. The reactants were passed either through the bore of the support tube (one sided geometry) or separately through the bore and the outside surface of the support tube (opposing reactants geometry). Permeable SiO<sub>2</sub> and B<sub>2</sub>O<sub>3</sub> layers could be formed in either the one-sided or the two-sided (opposing reactants) geometry, while deposition of TiO<sub>2</sub> and Al<sub>2</sub>O<sub>3</sub> layers was achieved only in the two-sided geometry. The permeances at 450 °C were 0.3 and 0.1 cm<sup>3</sup>/cm<sup>2</sup>-min-atm for SiO<sub>2</sub> membranes produced in the one-sided geometry and two-sided geometries respectively. The H<sub>2</sub>:N<sub>2</sub> permeance ratios were 500-5000. The TiO<sub>2</sub> and Al<sub>2</sub>O<sub>3</sub> membranes had somewhat lower permeance and H<sub>2</sub>:N<sub>2</sub> ratios. Annealing at high temperatures causes densification of the deposited material as evidenced by increased activation energy for H<sub>2</sub> permeation and correspondingly reduced permeance. The presence of H<sub>2</sub>O vapor accelerates the densification process. The densified membranes had a H<sub>2</sub> permeance as high as 0.1 cm<sup>3</sup>(STP)/min-atm-cm<sup>2</sup> at 500 °C and a H<sub>2</sub>/N<sub>2</sub> permeance ratio above 500.

Silica, titania and alumina layers deposited in an opposing reactants geometry were characterized by scanning electron microscopy (SEM) and electron microprobe analysis (EPMA). The layers are asymmetric, having a long tail towards the side of the chloride flow and a sharp boundary at the other side. The deposit thickness is several tenths of microns while the totally plugged region is of order of one micron. Silica deposit layers prepared in the one-sided geometry were examined by transmission electron microscopy (TEM), SEM, and EPMA. When the deposit was confined inside the pores of the Vycor substrate, the membranes were mechanically stable, but when it extended substantially outside of the porous matrix, the stresses induced by thermal cycling led to crack formation

and propagation. Electron microscopy revealed that the SiO<sub>2</sub> deposit density is maximum in a region about 0.5 μm thick adjacent to the bore surface and gradually declines to zero within a depth of about 10 μm from the surface. The thin region of maximum deposit density is responsible for permselectivity, for it essentially blocks the permeation of nitrogen and larger molecules while allowing substantial permeation of hydrogen. This region contains about 10% by volume trapped voids and as a result has relatively high permeability as suggested by percolation theory.

A mathematical model is developed for SiO<sub>2</sub> deposition in porous Vycor using SiCl<sub>4</sub> hydrolysis. The model describes reaction, diffusion and evolution of the pore structure due to accumulation of the solid product. The deposition reaction is described by transient heterogeneous kinetics in terms of the concentrations of silanol and chloride groups in the product layer as well as the concentrations of the gaseous reactants. Pore structure evolution was modeled by incorporating results of percolation theory in a continuum model. The model is capable of generating deposit profiles in good agreement with the experiment. It is shown that for typical deposition conditions the pseudosteady state approximation for surface species could lead to erroneous predictions. Pore connectivity interruption at a nonzero void fraction leads to thinner deposits and shorter deposition times for pore plugging compared to the corresponding ones for an infinitely connected medium.

The growth of zeolite NaA films on various inorganic substrates from a clear solution with composition 10 Na<sub>2</sub>O - 0.2 Al<sub>2</sub>O<sub>3</sub> - 1SiO<sub>2</sub> - 200 H<sub>2</sub>O was followed by XRD, SEM and TEM. Deposition geometries and conditions are identified for the development of uniform polycrystalline thin (<5μm) films consisting of intergrown crystals of zeolite NaA on porous and nonporous Al<sub>2</sub>O<sub>3</sub> disks. The films exhibit high crystallinity good adhesion to the substrate and thermal stability. The deposition technique demonstrates potential for developing molecular sieve membranes.

## Table of Contents

Acknowledgments.....	ii
Abstract.....	iii
List of Tables.....	ix
List of Figures.....	x
<b>Chapter 1 Introduction.....</b>	<b>1</b>
1.1 Overview.....	2
1.2 Outline of Thesis.....	5
1.2.1 Hydrogen Permselective Inorganic Composite Membranes.....	5
1.2.2 Zeolite NaA Thin Films.....	6
References.....	8
<b>Chapter 2 Synthesis of Hydrogen Permselective SiO<sub>2</sub>, TiO<sub>2</sub>, Al<sub>2</sub>O<sub>3</sub>, B<sub>2</sub>O<sub>3</sub> Membranes from the Chloride Precursors.....</b>	<b>12</b>
Abstract.....	13
2.1 Introduction.....	14
2.2 Experimental.....	16
2.2.1 Materials.....	16
2.2.2 Apparatus.....	17
2.2.3 Pretreatment.....	17
2.2.4 Deposition.....	17
2.2.5 Permeation Rate Measurements.....	18
2.2.6 SEM and EPMA.....	19
2.3 Results and Discussion.....	19
2.3.1 SiO <sub>2</sub> Deposition.....	19
2.3.2 TiO <sub>2</sub> Deposition.....	20

2.3.4	Al <sub>2</sub> O <sub>3</sub> Deposition.....	22
2.3.5	B <sub>2</sub> O <sub>3</sub> Deposition.....	22
2.3.6	SEM and Electron Microprobe Analysis.....	23
2.3.7	Reaction Mechanism.....	25
2.4	Conclusions.....	27
	Acknowledgment.....	28
	Literature Cited.....	29

<b>Chapter 3</b>	<b>A Kinetic Model of Membrane Formation by CVD of SiO<sub>2</sub> and Al<sub>2</sub>O<sub>3</sub>.....</b>	<b>46</b>
	Abstract.....	47
3.1	Introduction.....	48
3.2	Experimental Techniques.....	50
	3.2.1 Apparatus.....	50
	3.2.2 Scanning Electron Microscopy (SEM).....	51
3.3	Experimental Results.....	51
3.4	Model Formulation.....	54
	3.4.1 Reaction Mechanism for SiO <sub>2</sub> Formation.....	54
	3.4.2 Reaction Mechanism for Al <sub>2</sub> O <sub>3</sub> Formation.....	55
	3.4.3 Formulation of Kinetics and Species Balances.....	56
3.5	Numerical Results and Discussion.....	60
3.6	Conclusions.....	64
	Acknowledgments.....	65
	Literature Cited.....	66
	Notation.....	69
<b>Chapter 4</b>	<b>Structure and Aging Characteristics of H<sub>2</sub>-permselective SiO<sub>2</sub>-Vycor Membranes.....</b>	<b>85</b>

Abstract.....	86
4.1 Introduction.....	87
4.2 Experimental Techniques.....	90
4.2.1 CVD System.....	90
4.2.2 SEM, EPMA, TEM.....	90
4.2.3 Thermal and Hydrothermal Treatment.....	91
4.3 Results and Discussion.....	92
4.3.1 Effect of H <sub>2</sub> O and SiCl <sub>4</sub> Concentrations.....	92
4.3.2 Effect of Deposition Temperature.....	94
4.3.3 Thermal and Hydrothermal Treatment.....	94
4.3.4 Characterization of the Permselective Layer.....	96
4.3.5 Effect of Trapped Porosity on the H <sub>2</sub> Permeance.....	98
4.3.6 Estimation of Membrane Permeability Based on Percolation Theory.....	99
4.4 Conclusions.....	102
Acknowledgment.....	103
References.....	104

## **Chapter 5 Mathematical Modeling of SiO<sub>2</sub> Deposition in Porous Vycor.**

### **Effects of Transient Heterogeneous Kinetics and Pore**

#### **Connectivity Evolution..... 124**

Abstract.....	125
5.1 Introduction.....	126
5.2 Model Formulation.....	128
5.3 Numerical Results and Discussion.....	136
5.4 Conclusions.....	139
Acknowledgments.....	140
References.....	141

Notation.....	143
<b>Chapter 6 A Study on the Formation of Supported Zeolite NaA Films from a Clear Solution.....</b>	<b>153</b>
Abstract.....	154
6.1 Introduction.....	155
6.2 Experimental .....	156
6.2.1 Synthesis of Zeolite NaA from a Clear Solution.....	156
6.2.2 Preparation of Supported Zeolite NaA Films.....	157
6.2.3 Characterization.....	157
6.3 Results and Discussion.....	158
6.3.1 Synthesis of Zeolite NaA Powder from a Clear Solution.....	158
6.3.2 Film Preparation.....	160
6.3.2.1 Film Growth After the Deposition of Seeds.....	160
6.3.2.2 In-situ Film Preparation.....	161
Acknowledgment.....	163
References.....	164
<b>Chapter 7 Conclusions.....</b>	<b>179</b>

## List of Tables

Table 2.1	Conditions of Deposition and Permeances of the Resulting Membranes.	31
Table 2.2	One-Sided Deposition Experiments Which Did Not Result in Pore Plugging Within Two Hours of Reaction.....	32
Table 3.1	Model Parameter Values.....	71
Table 4.1	Hydrogen Permeance Evolution During Heat Treatment at 550 °C Under Dry Nitrogen.....	108
Table 4.2	Conditions of Deposition and Permeances of the Resulting Membranes as Deposited and After Heat Treatments in Dry and Wet Nitrogen.....	109
Table 4.3	Void Fractions and Mean Radii at Various Positions Across the Membrane (Estimated from TEM).....	110
Table 6.1	Diffusivity and Henry Coefficient for O <sub>2</sub> and N <sub>2</sub> in Zeolite NaA and Estimated Permeabilities.....	156

## List of Figures

Figure 1.1	Plot of diffusivity and pore size for porous media. From reference (11)	10
Figure 1.2	Correlation between pore size of molecular sieves and the diameter of various molecules. Reproduced from reference (12).....	11
Figure 2.1a	Schematic of the reactor system for opposing reactants deposition.....	33
Figure 2.1b	Schematic of reactant inlet for one-sided deposition.....	34
Figure 2.2	Permeances at deposition temperatures for hydrogen (- - -) and nitrogen (—) versus time of deposition by SiCl <sub>4</sub> and H <sub>2</sub> O reaction. a: opposing reactants geometry at 700 °C (■); and 800 °C (□). Reactant streams were 7% H <sub>2</sub> O-N <sub>2</sub> and 30% SiCl <sub>4</sub> -N <sub>2</sub> . b: one-sided deposition at 600 °C (■) and 400 °C (□). Reactant stream was 4% H <sub>2</sub> O - 15% SiCl <sub>4</sub> in N <sub>2</sub> .....	35
Figure 2.3	Schematic of concentration profiles in opposing reactants deposition....	36
Figure 2.4	Arrhenius plots for H <sub>2</sub> and N <sub>2</sub> permeances of SiO <sub>2</sub> membranes.....	37
Figure 2.5	Nitrogen (□, ■) and hydrogen (○, ●) permeation coefficients of TiO <sub>2</sub> membranes during deposition at 450 °C (—) and 600 °C (- - -). Reactants: 20% TiCl <sub>4</sub> -N <sub>2</sub> and 12% H <sub>2</sub> O-N <sub>2</sub> .....	38
Figure 2.6	Permeances measured at deposition temperatures for hydrogen (- - -) and nitrogen (—) versus time of AlCl <sub>3</sub> + H <sub>2</sub> O reaction at 450 °C (○), 700 °C(Δ), 800 °C (□). Reactant streams were 7% H <sub>2</sub> O-N <sub>2</sub> and 20% AlCl <sub>3</sub> -N <sub>2</sub> in opposing reactants geometry.....	39

Figure 2.7	Hydrogen and nitrogen permeances at 150 °C during deposition of B <sub>2</sub> O <sub>3</sub> at 150 °C in opposing reactants geometry. Reactant streams: 10% BCl <sub>3</sub> -N <sub>2</sub> and 10% H <sub>2</sub> O-O <sub>2</sub> .....	40
Figure 2.8	Hydrogen permeances of a B <sub>2</sub> O <sub>3</sub> membrane deposited at 150 °C and annealed under dry N <sub>2</sub> at 400 °C overnight (■), 300 °C (□) overnight, 150 °C overnight (●) and exposed to laboratory air at room temperature for 23 days (o). Calculated activation energies are given on the figure..	41
Figure 2.9	Scanning electron micrographs of tube cross sections containing TiO <sub>2</sub> deposited at 600 °C (a,b) and at 450 °C (c).....	42
Figure 2.10	EPMA linescan of tube cross sections containing TiO <sub>2</sub> layers deposited at 600 °C (a) and 450 °C (b).....	44
Figure 2.11	EPMA linescan of a tube cross section containing an Al <sub>2</sub> O <sub>3</sub> layer deposited by AlCl <sub>3</sub> hydrolysis at 800 °C in an opposing reactants geometry. Reactant streams were 7% H <sub>2</sub> O-N <sub>2</sub> and 20% AlCl <sub>3</sub> -N <sub>2</sub> .....	45
Figure 3.1	Schematic of deposition system.....	72
Figure 3.2	Evolution of N <sub>2</sub> permeance (measured at deposition temperature) for : Alumina deposition at 450 °C (●) and 800 °C (Δ), using 8% H <sub>2</sub> O-N <sub>2</sub> and 20% AlCl <sub>3</sub> -N <sub>2</sub> in opposing reactants geometry. Silica deposition at 800°C (O) and 700 °C (■), using 7% H <sub>2</sub> O-N <sub>2</sub> and 30% SiCl <sub>4</sub> -N <sub>2</sub> in opposing reactants geometry.....	73
Figure 3.3a	SEM micrograph of an Al <sub>2</sub> O <sub>3</sub> membrane at two different magnifications (bars are 100 μm at left and 10 μm at right). Membrane prepared at 450 °C by opposing reactants deposition with 20% AlCl <sub>3</sub> -N <sub>2</sub> and 7% H <sub>2</sub> O-N <sub>2</sub> .....	74

Figure 3.3b	Mass ratio of $\text{Al}_2\text{O}_3$ (deposit) to $\text{SiO}_2$ (substrate) obtained by electron microprobe analysis of a membrane prepared at $800\text{ }^\circ\text{C}$ by opposing reactants deposition with 20% $\text{AlCl}_3\text{-N}_2$ and 7% $\text{H}_2\text{O-N}_2$ .....	75
Figure 3.4	Electron microprobe analysis of Vycor cross-sections subjected to $\text{Al}_2\text{O}_3$ deposition in the opposing reactants geometry at $450\text{ }^\circ\text{C}$ with 20% $\text{AlCl}_3\text{-N}_2$ and 7% $\text{H}_2\text{O-N}_2$ for 3 min (O), 10 min ( $\diamond$ ) and 15 min ( $\Delta$ )...	76
Figure 3.5	Electron microprobe line scan of a tube cross-section after $\text{SiO}_2$ deposition in opposing reactants geometry using 30% $\text{SiCl}_4\text{-N}_2$ and 7% $\text{H}_2\text{O-N}_2$ , for 1 hr.....	77
Figure 3.6	Electron microprobe line scan of a tube cross-section subjected to $\text{Al}_2\text{O}_3$ deposition after pretreatment by $\text{AlCl}_3$ .....	78
Figure 3.7	Simulated evolution of $\text{SiO}_2$ deposit at $800\text{ }^\circ\text{C}$ in opposing reactants geometry using the parameter values given in Table 3.1 except $C_{10} = 0.3\text{ atm/RT}$ , $C_{20} = 0.07\text{ atm/RT}$ (as in the experiments of Fig. 3.5). ( $\bullet$ ) Data of Fig. 3.5 replotted for comparison.....	79
Figure 3.8	Simulated density profiles of the $\text{SiO}_2$ layers at the end of deposition, for three different values of $k_2/k_1$ . The corresponding deposition times are given in the Figure. Parameters values are given in Table 3.1.....	80
Figure 3.9	Effect of condensation reactions (Eqs. 3.4 and 3.5) on deposit profiles at the end of deposition.....	81
Figure 3.10	Simulated density profiles for different values of initial OH concentrations.....	82

Figure 3.11	Effect of chloride concentration on deposit profile.....	83
Figure 3.12	Simulated density profiles of SiO <sub>2</sub> layers at the end of deposition for four different combinations of reaction orders $\alpha$ and $\beta$ using the rate expression $r = k C_{10}^{\alpha} C_{20}^{\beta}$ . Deposition conditions are those of the experiment shown in Fig. 3.5.....	84
Figure 4.1	Evolution of H <sub>2</sub> and N <sub>2</sub> permeances during OSG deposition at 600 °C. Reactant stream was 2.7% SiCl <sub>4</sub> and 13% H <sub>2</sub> O in N <sub>2</sub> .....	111
Figure 4.2	Time to pore plugging, $t_p$ , for various combinations of SiCl <sub>4</sub> and H <sub>2</sub> O concentrations at 600 °C.....	112
Figure 4.3	SEM micrographs of the bore surface of Vycor tubes. <b>a</b> : before deposition, <b>b</b> : after 15 minutes of deposition (time to pore plugging) at 600 °C. Reactant stream was 2.7% SiCl <sub>4</sub> and 13% H <sub>2</sub> O in N <sub>2</sub> .....	113
Figure 4.4	SEM micrographs of the bore surface of Vycor tubes. <b>a</b> : after 15 minutes of deposition (time to pore plugging); <b>b</b> : after 30 minutes of deposition, and <b>c</b> : after 50 min of deposition at 600 °C. Reactant stream was 2.7%/SiCl <sub>4</sub> and 13% H <sub>2</sub> O in N <sub>2</sub> .....	114
Figure 4.5	SEM microphotograph of the bore of a Vycor tube after OSG deposition at 600 °C with 8.7% SiCl <sub>4</sub> and 13% H <sub>2</sub> O in N <sub>2</sub> immediately after pore plugging. <b>a</b> : reactor entrance, <b>b</b> : reactor exit.....	115
Figure 4.6	Morphology of cracks developed during thermal cycling of membranes with substantial deposition at the outside surface. <b>a</b> : planar view, <b>b</b> : cross section.....	116
Figure 4.7	Arrhenius plot of 1/ $t_p$ for OSG deposition using 2.7% SiCl <sub>4</sub> and	

	13% H <sub>2</sub> O.....	117
Figure 4.8	Evolution of H <sub>2</sub> permeance at 600 °C, K(t), and its activation energy during thermal treatment under dry N <sub>2</sub> at 550 °C. K <sub>0</sub> : permeance immediately after pore plugging. Membrane formed by a 5 min deposition at 750 °C using 2.7% SiCl <sub>4</sub> and 13% H <sub>2</sub> O.....	118
Figure 4.9	Transmission Electron Micrograph of untreated porous Vycor glass....	119
Figure 4.10	Transmission Electron Micrograph of untreated Vycor with the binary image (the pore structure in black) and the pore chord distribution.....	120
Figure 4.11	Transmission Electron Micrograph of thin sections of the composite membrane at various distances from the side of reactants flow. Deposition conditions: T = 600 °C, 13% H <sub>2</sub> O and 2.7% SiCl <sub>4</sub> in N <sub>2</sub> ...	121
Figure 4.12	Void fraction normalized by initial void fraction, $\varepsilon/\varepsilon_0$ , versus distance from the side of reactants flow. Deposition conditions as in Figure 4.11.....	122
Figure 4.13	Transmission Electron Micrograph of the membrane region close to the side of reactants flow (region of maximum deposition). Deposition conditions as in Figure 4.11.....	123
Figure 5.1	Accessibility functions of various lattices.....	146
Figure 5.2	Predicted permeance evolution of inert gas for ORG deposition at 800 °C, using 10% water and 30% chloride. Parameters used: $v = 40\text{cm}^3/\text{mol}$ ( <b>a<sub>1</sub>,a<sub>2</sub></b> ) and $33\text{cm}^3/\text{mol}$ ( <b>b<sub>1</sub>, b<sub>2</sub></b> ), $S_{\text{OH}}^0 = 3/\text{nm}^2$ , $S^*(\text{OH}+\text{Cl}) = 5/\text{nm}^2$ . Lattices used : $z = \infty$ ( <b>a<sub>2</sub>,b<sub>2</sub></b> ), and decorated Bethe lattice ( $z=3,d=4$ ) ( <b>a<sub>1</sub>,b<sub>1</sub></b> ). .....	147

- Figure 5.3 Deposit profiles at the end of deposition from the simulations of Figure 5.2. **a**<sub>1</sub>:(z=3,d=4), v=40cm<sup>3</sup>/mol; **a**<sub>2</sub>:(z=∞), v=40cm<sup>3</sup>/mol; **b**<sub>1</sub>:(z=3,d=4), v=40cm<sup>3</sup>/mol; **b**<sub>2</sub>:(z=∞), v=40cm<sup>3</sup>/mol..... 148
- Figure 5.4 Influence of the kinetic parameter  $S^*_{(OH+Cl)}$  on the deposit profiles. **a**: $S^*_{(OH+Cl)}=5/nm^2$  (time for pore plugging=34.5min), **b**: $S^*_{(OH+Cl)}=10/nm^2$  (time for pore plugging=32.5min), using v=40cm<sup>3</sup>/mol and a (z=3,d=4)lattice. Other parameters as in Figure 5.2 149
- Figure 5.5 Influence of initial OH concentration on the deposit profiles. **a**:1.5OH/nm<sup>2</sup> (time for pore plugging=29min), **b**:3OH/nm<sup>2</sup> (time for pore plugging=34.5min). Using  $S^*_{(OH+Cl)}=5/nm^2$  and other parameters as in Figure 5.4..... 150
- Figure 5.6 **a**:deposit profile at the end of deposition after dehydroxylation (time for pore plugging=66.5min), **b**:corresponding profile at the end of deposition without prior dehydroxylation (plugging time=39min). Using  $S^*_{(OH+Cl)}=5/nm^2$ , v=33cm<sup>3</sup>/mol and other parameters as in Figure 5.4..... 151
- Figure 5.7 Influence of deposition temperature on deposit profiles. **a**:400 °C, **b**:600 °C, **c**:700 °C, **d**:800 °C. Using 3OH/nm<sup>2</sup> and other parameters as in Figure 5.6..... 152
- Figure 6.1 Schematic of the arrangement of the substrate and synthesis mixture for the development of zeolite NaA films on porous and nonporous substrates..... 166
- Figure 6.2 SEM micrographs of the particles collected after crystallization at 70 °C for: a, 1hr 15min; b, 1hr 40min; c, 2hrs 10min; d, 2hrs 45min; e, 3hrs;

- f, 3hrs 30min..... 167
- Figure 6.3 SEM micrographs of the precipitated cake after crystallization at 70 °C:  
**a:** 8hrs 35min, top view of the precipitate side facing the synthesis mixture (opposite to the Teflon bottle), **b:** 8hrs 35min, cross section 100  $\mu\text{m}$  away from the top side, **c:** 8hrs 35min, bottom side, **d:** 17hrs 30min, top side..... 169
- Figure 6.4 SEM micrographs of films of zeolite NaA formed after crystallization at 70 °C for 10hrs 30min: **a:** bottom side of the precipitated cake, **b:** film collected from the vertical walls of the Teflon vessel. The smooth side facing the Teflon wall is shown..... 170
- Figure 6.5 XRD patterns from the powder collected after crystallization at 70 °C for: 1hr 15min, 2hrs 25min, 2hrs 45min, 3hrs 30min, 4hrs, 8hrs 35min, and 17hrs 30 min (from the bottom to the top of the Figure)..... 171
- Figure 6.6 Top view SEM micrographs of film grown after deposition of seeds (see text): **a:** just after the filtration of suspended particles, **b:** after 6 30min cycles of contact with clear solution at 70 °C, **c:** after 12 30min cycles of contact with clear solution at 70 °C, **d:** deposit as in Figure 6.6c after scratching the top layer..... 172
- Figure 6.7 XRD patterns of  $\alpha\text{-Al}_2\text{O}_3$  disks treated for various times at 70 °C in contact with the crystallizing solution in the arrangement shown in Figure 6.1. From bottom to top of the Figure: 2hrs, 3hrs, 4hrs, 5hrs, 6hrs..... 173
- Figure 6.8 Top view SEM micrographs of deposits on  $\alpha\text{-Al}_2\text{O}_3$  non porous disks

after crystallization at 70 °C in the arrangement shown in Figure 6.1:  
**a:** Al<sub>2</sub>O<sub>3</sub> substrate, **b:** 2hrs 45min, **c:** 3hrs 30 min, **d:** 5hrs, **e:** 6hrs,  
**f:** 8hrs, **g:** lower magnification of (6.8.a), **h:** lower magnification of  
 (6.8.e)..... 174

Figure 6.9 Cross section SEM micrographs of disks treated as described in Figure  
 6.8: **a:** 6hrs, **b:** 8hrs..... 176

Figure 6.10 Top view SEM micrographs of films developed after 6hrs at 70 °C with  
 rotation speed: **a:** 6 rpm, **b:** 45 rpm..... 177

Figure 6.11 Cross section SEM micrograph of film developed on porous Al<sub>2</sub>O<sub>3</sub>  
 after 7hrs at 70 °C..... 178

# **CHAPTER 1**

## **Introduction**

## 1.1 OVERVIEW

Gas separation makes up a large and costly component of industrial processes. Thus development of novel efficient separations can have a large impact on well established processes in the energy and fuels industry. Moreover, new energy saving processes are waiting such developments. Synthesis gas and/or hydrogen production from coal gasification, natural gas separation and purification (CH<sub>4</sub> from CO<sub>2</sub>, N<sub>2</sub>, H<sub>2</sub>S, etc.), combustion with pure O<sub>2</sub> or O<sub>2</sub> enriched air to eliminate or reduce NO<sub>x</sub> emissions, straight vs. branched hydrocarbons separations in refinery operations and water alcohol separations are some of the long list of such processes.

Membrane separations, due to their inherent energy efficiency, simplicity and compact character (1), have been the subject of much industrial and academic research (1), (2), (3), (4). Although cost comparison of separation processes depends on the specific application, in a number of economic analyses by industrial researchers the membrane processes, in general, were shown to be more economical than conventional methods such as cryogenics and adsorption (PSA, TSA) (3), (4), (5).

The most important requirements for membrane applications are sufficient *selectivity* and *permeance* as well as thermal and structural *stability*, and resistance towards chemicals.

*Selectivity*, often represented as the permeance ratio of two gases, is the ability of the membrane to separate a given gas mixture into its components. For highly selective separations one has to use either the inherent ability of a dense material to be more permeable to a certain gas from a mixture of gases or differences in the velocity of gases flowing through a porous material.

Various crystalline and amorphous dense materials are known for their permselective properties. Transport processes in crystalline materials are continuous

displacements of vacant sites by mobile atoms usually in ionic form, called vacancy mechanism (6). Oxygen ion diffusion in crystalline zirconia (7) is an example.

Transport processes in amorphous materials are usually governed by solution diffusion phenomena often following Henry's and Fick's laws. Various theories try to explain transport mechanisms (8,9). The relative fast diffusion of helium, neon and hydrogen in amorphous silica is well known (8). Amorphous silica is composed of a three dimensional network of silicon-oxygen tetrahedra containing holes which make up its free volume (10). Gas atoms or molecules when dissolved in silica glass lodge in these holes and diffuse by jumping from one hole to the other. Small molecules like hydrogen can diffuse faster than larger molecules (oxygen, nitrogen, etc.) because they experience less interatomic forces when they try to penetrate the glass network.

Figure 1.1 is a plot of diffusivity and pore size for porous media (11). Transport processes in pores exceeding  $1000\text{\AA}$  cannot be used for gas separation. In pores between  $10\text{\AA}$  to  $1000\text{\AA}$ , gas transport is governed by Knudsen diffusion and the velocity ratio of two gases is inversely proportional to the square root of their molecular weights. Therefore, membranes with pores in that range provide acceptable selectivity only when two gases in a mixture have significant differences in molecular weights. Due to the limited range of selectivity, industrial application is narrowly bounded.

It is in the configurational regime where major changes in diffusivities can occur with minor differences in the diffusing molecules structure and, therefore, the materials operating in that regime, called molecular sieves, are of major importance for selective separations. Zeolites and non aluminosilicate molecular sieves are crystalline solids containing channels of molecular dimension as part of their crystalline structure. Figure 1.2 is a correlation between the pore structure of molecular sieves and the diameter of various molecules (12) that illustrates the separation potential of these materials. Separation by size exclusion is the ideal separation mechanism, but separations based on differences in

interactions of diffusing species with the solid matrix can be very effective. In the configurational regime the pore sizes are smaller than the mean free path in Knudsen flow and a molecule will collide more often with the wall. Non crystalline micropores materials like carbon molecular sieves are also known, but their structure is not as well defined (13).

*Permeance* or permeability coefficient,  $K$ , is the flux of the permeating gas,  $J$ , normalized with the surface area of the membrane,  $S$ , and the driving force,  $\Delta P$ , across the membrane:

$$K = J / (S \cdot \Delta P)$$

The permeability coefficient further normalized with the membrane thickness,  $L$ , is called permeability,  $A$ , and is a property of the membrane material:

$$A = K L$$

In order to achieve high permeance through a membrane material of a given permeability, the membrane thickness should be minimized.

As inferred by the above discussion, depending on the material selection, dense or molecular sieve membranes will have high selectivities for certain gas couples by proper membrane material selection. These high selectivities, though, are usually coupled with very low permeabilities and therefore, membrane thicknesses of the order of  $1\mu\text{m}$  or less are desirable in order to achieve adequate permeances. In order to secure its mechanical stability, the membrane structure has to be configured in a composite (asymmetric) form consisting of a highly permeable, usually porous support and an ultrathin layer of the non porous separating material.

Organic (polymeric) membranes have been commercial for a numbers of years, but recently there is a growing interest for highly selective inorganic membranes due to their unique *stability* characteristics (2) unmatched by organic membranes, namely, chemical stability in corrosive atmospheres and high temperature tolerance. High temperature tolerance will allow for inorganic membranes to be incorporated in membrane-reactor

configurations where species can be separated at the same time they are produced without disturbing the reaction process. Simultaneous reaction and product separation achieved through a membrane-reactor can drastically improve the conversion of many equilibrium limited reactions. In some cases, membranes can also be used to add a reactant in a controlled way along a reactor to suppress undesirable side reactions; for instance, in partial oxidations control of oxygen concentration along the reactor can be achieved by an oxygen semipermeable membrane. The effort to develop effective membrane reactors has become more active recently; several reports on the concept and experiments with membrane reactors for various reactions have been published (14).

Although the concepts of membrane reactors and high temperature membrane separations have been established, commercial applications of such processes rely on our ability to fabricate membrane structures, a technology underdeveloped for inorganic materials.

## **1.2 OUTLINE OF THESIS**

This thesis is an effort towards the development of inorganic composite membranes for common gases separations. The primary contribution of this work is the development of composite amorphous SiO<sub>2</sub>-porous glass membranes for hydrogen separation at high temperatures. Efforts towards other dense oxide and zeolite membranes are also described.

### ***1.2.1 Hydrogen Permselective Inorganic Composite Membranes***

Gavalas et al. (15) introduced an H<sub>2</sub> permselective membrane made by chemical vapor deposition (CVD) of a thin SiO<sub>2</sub> film in porous Vycor glass. These films were deposited using SiH<sub>4</sub> oxidation. Although the technique produced highly selective membranes, low permeance and stability problems were noticed (16). The objective of this

work was to develop chemical processes effective for the formation of SiO<sub>2</sub> and other oxide thin films in porous glass. In *Chapter 2* of this thesis, the chemical vapor deposition of silica, alumina, boria and titania using chloride hydrolysis is presented. The characteristics of the deposited layers and the permselective properties of the composite membranes are discussed with emphasis on the different CVD geometries and proposed reaction mechanisms. *Chapter 3* contains further characterization of the deposits and the development of a mathematical model describing the deposition process with emphasis on the kinetics of deposition. *Chapter 4* contains results from stability testing of the membranes and a rather detail characterization of the deposited layer by electron microscopy. Membrane stability and permeance are correlated with its microstructure. In *Chapter 5* the mathematical model presented in *Chapter 3* is refined by including concepts of percolation theory in the description of pore structure evolution and a more realistic description of deposition kinetics.

### ***1.2.2 Zeolite NaA Thin Films***

Although amorphous oxide membranes are permselective for hydrogen, they are not promising for separations of mixtures of bigger molecules like oxygen and nitrogen due to the very low permeability of these larger molecules. The separation properties of zeolites stand out among those of other inorganic materials due to their applicability to a variety of gas mixtures, high selectivity and ability to function over a wide temperature range from ambient to as high as 500 °C. The applicability to specific gas mixtures can be controlled by the choice of zeolite structure and by exchanging with different cations the same zeolite structure. All currently commercial separation processes based on zeolites work in cycles, first adsorbing one or more components from a mixed feed stream and then regenerating the sorbent. Development of zeolite membranes would make it possible to replace the complicated and energetically ineffective adsorption-desorption cycles by steady-state,

continuous, separation. Other applications like membrane reactors would also be developed. *Chapter 6* describes the development of thin supported polycrystalline films of zeolite NaA and their potential application for the development of membranes able to separate O<sub>2</sub> from N<sub>2</sub>.

**REFERENCES**

1. Hsieh, H.P., " Inorganic Membranes," *AIChE Symposium Ser.* **261 (84)**, 1 (1988).
2. Armor, J.N., "Catalysis with Permselective Inorganic Membranes," *Applied Catalysis* **49**, 1 (1989).
3. Spillman, R.W., "Economics of Gas Separation Membranes," *Chem. Eng. Prog.* **85 (1)**, 41 (1989).
4. Schendel, R.L., "Using Membranes for Separating Acid Gas and Hydrocarbons," *Chem. Eng. Prog.* **80 (5)**, 39 (1984).
5. Schendel, R.L., C.L. Mariz, and J.Y. Mak, "Is Permeation Competitive?" *Hydrocarb. Proc.* **62 (8)**, 58 (1983).
6. Borg, R.J. and G.J. Dienes, *An Introduction to Solid State Diffusion*, p. 53, Academic Press Inc. (1988).
7. Cales, B. and J.F. Baumard, "Oxygen Semipermeability and Electronic Conductivity in Calcia-Stabilized Zirconia," *J. Material Sci.* **17 (11)**, 3243 (1982).
8. Shelby, J.E., Molecular Solubility and Diffusion, *Treatise of Materials Science and Technology* Vol.17, Academic Press, New York (1979).

9. Doremus, R.H., *Modern Aspects of Vitreous State*, p.1, Butterworth & Co. (1962).
10. Willey, J.D., "Silica," *Kirk-Othmer Encycl. Chem. Technol.* 3rd ed., Vol. 20, p. 749, John Wiley, New York (1980).
11. Venuto, P.B., "Organic Catalysis over Zeolites: A Perspective of Reaction Paths within Micropores," Review presented at the Symposium on New Catalytic Chemistry Utilizing Molecular Sieves, ACS National Meeting, Chicago, August 22-27, 1993; to be published as part of Symposium proceedings in *Microporous Materials* (J. Weitcamp, Ed.), Elsevier.
12. Davis, M.E., "New Vistas in Zeolite and Molecular Sieve Catalysis," *Acc. Chem. Res.* **26** (3), 111-115 (1993).
13. Koresh, J.E. and A. Soffer, "Molecular Sieve Carbon Permselective Membrane. Part I. Presentation of a New Device for Gas Mixture Separation," *Sep. Sci. Technol.* **18**, 723 (1983).
14. Hsieh, H.P., "Inorganic Membrane Reactors," *Catal. Rev.* **33**, 1 (1991).
15. Gavalas, G.R., C. E. Megiris and S. W. Nam, "Deposition of H<sub>2</sub>-permselective SiO<sub>2</sub> films, *Chem. Eng. Sci.*," **44**, 1829 (1989).
16. Nam, S.W. and G. R. Gavalas, "Stability of H<sub>2</sub>-permselective SiO<sub>2</sub> films formed by chemical vapor deposition," *AIChE Symp. Ser.*, **85** (268), 68-74 (1989).

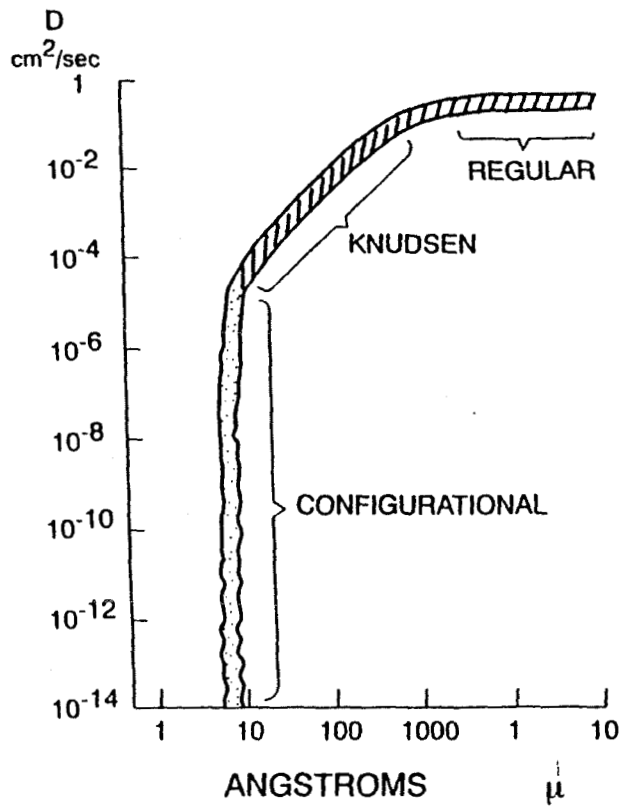


Figure 1.1 Plot of diffusivity and pore size for porous media. From reference (11).

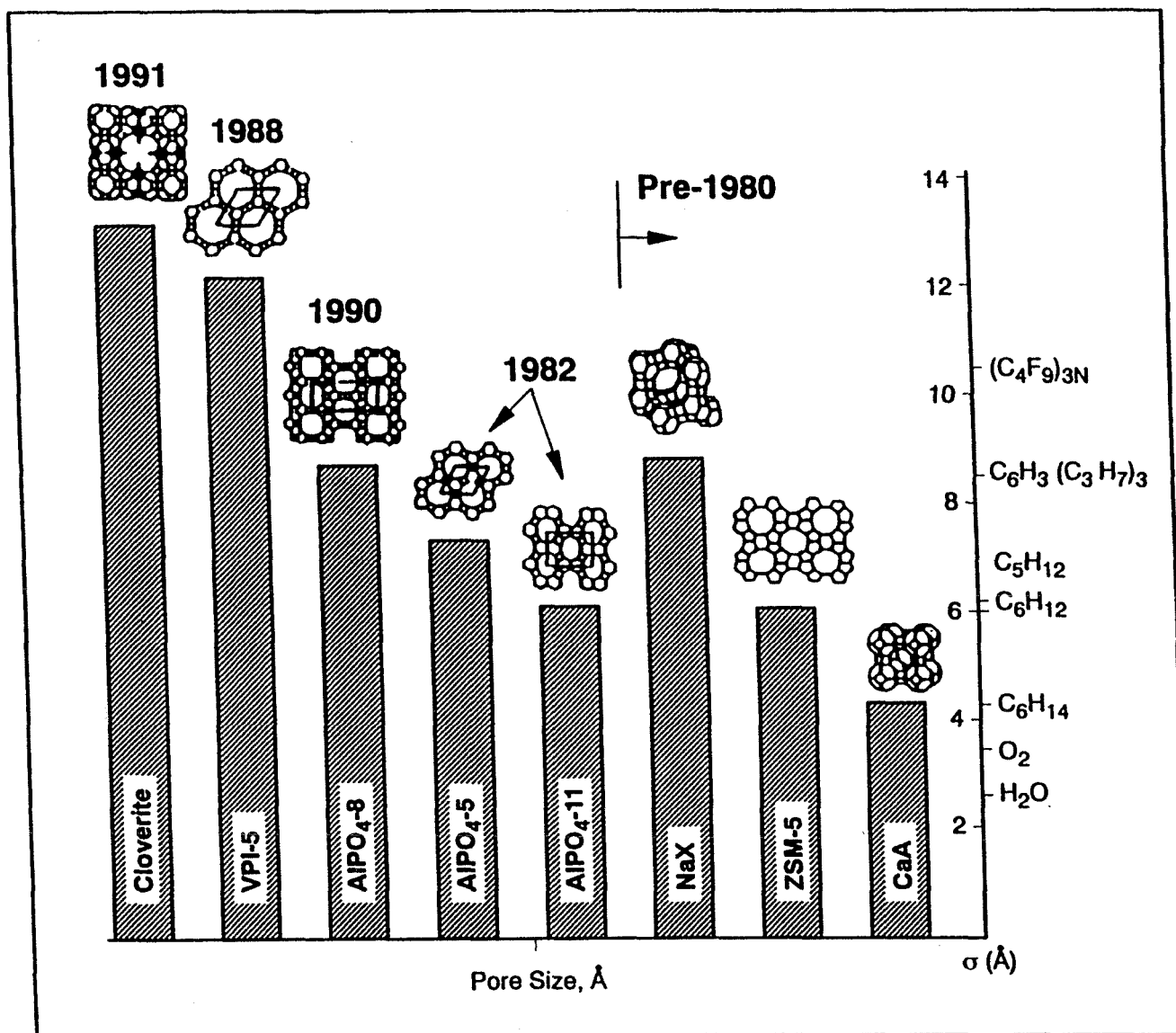


Figure 1.2 Correlation between pore size of molecular sieves and the diameter of various molecules. Reproduced from reference (12).

## CHAPTER 2

# **Synthesis of Hydrogen Permselective SiO<sub>2</sub>, TiO<sub>2</sub>, Al<sub>2</sub>O<sub>3</sub>, B<sub>2</sub>O<sub>3</sub> Membranes from the Chloride Precursors**

Published *I&EC Res.* **30**, 2152 (1991)

# Synthesis of Hydrogen Permselective $\text{SiO}_2$ , $\text{TiO}_2$ , $\text{Al}_2\text{O}_3$ , $\text{B}_2\text{O}_3$ Membranes from the Chloride Precursors

Michael Tsapatsis, Soojin Kim, SukWoo Nam and George Gavalas

*Department of Chemical Engineering, California Institute of Technology,*

*Pasadena, CA 91125*

## ABSTRACT

Hydrogen-perselective membranes were synthesized by chemical vapor deposition of  $\text{SiO}_2$ ,  $\text{TiO}_2$ ,  $\text{Al}_2\text{O}_3$ , and  $\text{B}_2\text{O}_3$  layers within the pores of Vycor tubes. The deposition involved reaction of  $\text{SiCl}_4$ , etc., with water at 100-800 °C depending on the chloride and the reaction geometry. Permselective  $\text{SiO}_2$  layers could be formed in either the one-sided or the two-sided (opposing reactants) geometry, while deposition of  $\text{TiO}_2$  and  $\text{Al}_2\text{O}_3$  layers was achieved only in the two-sided geometry. The permeances at 450 °C were 0.3 and 0.1  $\text{cm}^3/\text{cm}^2\text{-min-atm}$  for  $\text{SiO}_2$  membranes produced in the one-sided geometry and two-sided geometries respectively. The  $\text{H}_2:\text{N}_2$  permeance ratios were 1000-5000. The  $\text{TiO}_2$  and  $\text{Al}_2\text{O}_3$  membranes had somewhat lower permeance and  $\text{H}_2:\text{N}_2$  ratios. The membranes were characterized by scanning electron microscopy and electron microprobe analysis. A reaction mechanism is suggested involving heterogeneous reactions of chloride and water molecules with hydroxyl and chloride groups in the growing deposit layer.

## 2.1 INTRODUCTION

Inorganic membranes have recently attracted interest for use to high temperature gas separations coupled with reaction in a "membrane-reactor" configuration. The close coupling of reaction and product separation can greatly increase the yield or selectivity of equilibrium-limited reactions. Several classes of materials have attractive separation properties and have been investigated as membrane materials. Amorphous oxides such as SiO<sub>2</sub>, B<sub>2</sub>O<sub>3</sub>, and GeO<sub>2</sub> have been known to be highly selective for permeation of helium and hydrogen (Lieby and Chen, 1960; Shelby, 1979; Boyd and Thompson, 1980). But the absolute permeability of these oxides is low; therefore, a membrane would have to consist of a thin film of the selective oxide supported on a highly permeable material, preferably a slender tube or capillary.

During the last few years we have been developing hydrogen permselective membranes by chemical vapor deposition of an amorphous oxide layer within the walls of porous Vycor tubes, the latter serving as the support element. The amorphous oxides that we have worked with are SiO<sub>2</sub>, TiO<sub>2</sub>, Al<sub>2</sub>O<sub>3</sub>, and B<sub>2</sub>O<sub>3</sub>. Originally we carried out deposition of SiO<sub>2</sub> using silane oxidation



In our most recent work we have used chloride hydrolysis to deposit SiO<sub>2</sub> and the other oxides:



Our initial experiments employed low pressure silane ( $\text{SiH}_4$ ) oxidation to deposit films on porous Vycor tubes. The films produced under these standard CVD conditions were porous consisting of partially fused  $\text{SiO}_2$  particles 0.5-1  $\mu\text{m}$  in diameter. After one hour of deposition there was no measurable change in the permeation rates of  $\text{H}_2$  or  $\text{N}_2$ , and no change was observed by sintering at 800 °C. Sintering of the porous film at temperatures above 800 °C was not attempted, for along with the porosity of the deposited film it would have eliminated the porosity of the Vycor support.

At that point we changed the reaction geometry introducing the two reactants, at ordinary pressures, from opposite sides of the tube wall. The reactants diffuse towards each other and react within the porous matrix. Once the pores are plugged, the reaction ceases and the resulting nonporous layer, imbedded within the porous wall, constitutes the  $\text{H}_2$  permselective barrier. The results of our work with  $\text{SiH}_4$  oxidation have been reported (Gavalas et al., 1989; Nam and Gavalas, 1989; Gavalas and Megiris, 1990).

The temperature of 450 °C used in the opposing reactants oxidation of silane could not be varied significantly without adversely affecting the nature of deposition. If the temperature was decreased below 400 °C, the reaction rate became too low producing a thick film with low permeation rates. At temperatures above 500 °C, pyrolysis of silane to elemental silicon became significant, plugging the pores of the support tube over a broad region and eliminating the permeability altogether. When the films produced at 450 °C were subjected to higher temperatures, e.g., 600 °C, especially in the presence of water vapor, they suffered densification accompanied by decrease of permeation rates and sometimes decrease of selectivity as well. However, when the film deposition had taken place with water vapor added to the silane and oxygen reactants, subsequent thermal exposure to higher temperatures and water vapor caused a decrease of permeability but left the selectivity unchanged.

If deposition could be carried out at higher temperatures, e.g., 700 °C, the film produced would be denser and, therefore, more stable to temperatures at least as high as 600 °C, at which the films produced by silane oxidation suffered significant densification. The reaction between  $\text{SiCl}_4$  and  $\text{H}_2\text{O}$  is suitable for this purpose. The chloride is also safe from the standpoint of explosion, but is highly corrosive in the presence of humidity. In this paper we report our membrane synthesis work using the hydrolysis of  $\text{SiCl}_4$ ,  $\text{TiCl}_4$ ,  $\text{AlCl}_3$ , and  $\text{BCl}_3$ .

Our experiments with  $\text{SiCl}_4$  hydrolysis have shown that one-sided deposition and opposing reactants deposition are both suitable for the formation of permselective layers. In fact, one-sided deposition produces thinner layers having higher permeation rates. However, permselective layers of  $\text{TiO}_2$  and  $\text{Al}_2\text{O}_3$  could only be made by opposing reactants deposition.

The purpose of this paper is to present experimental results on the formation of  $\text{SiO}_2$ ,  $\text{TiO}_2$ ,  $\text{Al}_2\text{O}_3$  and  $\text{B}_2\text{O}_3$  layers by the hydrolysis of the respective chlorides and discuss qualitatively the structure of these layers and the differences between the opposing reactants and the one-sided deposition.

## 2.2 EXPERIMENTAL

### 2.2.1 *Materials*

Porous Vycor (Code 7930) tubes of 5 mm outside diameter, 1.1 mm wall thickness, 0.28 void fraction and 40 Å mean pore diameter were supplied by Corning, Inc. Nonporous quartz tubes were welded from either side of a 30 cm long porous Vycor tube to permit connection with metal fittings as shown in Figure 2.1.

Silicon tetrachloride (99.999%, Aldrich Chem. Co.), aluminum chloride (99.99%, Aldrich Chem. Co.), Boron trichloride (Matheson) and titanium chloride (99.9% Aldrich

Chem. Co.) were used throughout these studies. High purity  $N_2$ ,  $O_2$ ,  $H_2$  gas supplied by Matheson were further purified by Altech gas purifiers.

### 2.2.2 Apparatus

A schematic diagram of the apparatus for deposition and permeation rate measurement is shown in Figures 2.1a and 2.1b. The reactor, placed in a furnace, consists of a porous Vycor tube (substrate) concentric to an outer nonporous quartz tube of 12 mm inner diameter.

### 2.2.3 Pretreatment

Before reaction the tubes were heated at 100 °C and 200 °C under  $N_2$  flow to remove adsorbed water and then at 600 °C under oxygen flow for several hours in order to remove any adsorbed organic impurities.

### 2.2.4 Deposition

The reactants (liquid chloride and water) were introduced into the reactor, either separately to the inner and annulus region of the reactor for opposing reactants deposition or both into the inner region for one-sided reactant deposition. In either case the reactants were carried by  $N_2$  streams flowing through bubblers with a constant flowrate of 50 ml (STP)/min. For  $Al_2O_3$  depositions, an  $AlCl_3$  sublimator was used in place of the chloride bubbler.

The concentrations of the reactants were controlled by adjusting their vapor pressures by regulating the temperatures of the bubblers. Because the flowrates of the  $N_2$  streams through the bubbler were low, it was assumed that the carrier gases was in each case saturated with the reactants.

For B<sub>2</sub>O<sub>3</sub> depositions a BCl<sub>3</sub> lecture bottle was used and the gaseous chloride stream was diluted with N<sub>2</sub> to the desired concentration.

The reaction took place at atmospheric pressure. A series of 10 to 15 minute reactions each followed by purging with N<sub>2</sub> and permeation rate measurements was carried out for each experiment.

Typical concentrations used throughout this study for the opposing reactants geometry were around 10% chloride in N<sub>2</sub> and 10% water in N<sub>2</sub>. For one-sided depositions, concentrations were varied from 1 to 10%. Exact values are given later for each experiment.

### ***2.2.5 Permeation Rate Measurements***

The permeation rates to various gases were determined by a bubble flowmeter while the pressure difference between the compartments separated by the membrane was maintained at 30 psia. Permeation rates below the limit which can be measured by the bubble flowmeter were measured using a mass spectrometer and a sensitive pressure transducer connected to a computer. In the latter case, the inside of the membrane was maintained at 2 atm under flow while the outer annulus was initially evacuated. The annulus was then isolated from vacuum and its transient pressure measured by the pressure transducer or the mass spectrometer. The permeance was then determined from the following equations, assuming the validity of ideal gas law:

$$K [\text{cm}^3(\text{STP})/\text{cm}^2 \text{ atm min}] = dV/dt/S \Delta P \quad (2.6)$$

$$dV/dt = C dP/dt \quad (2.7)$$

where  $S$  is the surface area of the membrane,  $\Delta P$  is the pressure difference across the membrane,  $dP/dt$  the pressure rise in the annulus, and  $C$  is the calibration factor established between the pressure transducer and the bubble flowmeter.

### **2.2.6 SEM and EPMA**

SEM analysis was conducted using a CamScan electron microscope operating at 20 kV and with resolution of 500 Å. The samples were prepared by first casting small sections of the Vycor tube containing the deposited oxide and then polishing and coating with carbon or gold. Because of difficulties in sample preparation, it was not attempted to use the instrument at its highest resolution. The cross section of the tube was also examined by a JEOL 733 Superprobe electron microprobe by wavelength dispersive spectroscopy.

## **2.3 RESULTS AND DISCUSSION**

### **2.3.1 SiO<sub>2</sub> Deposition**

Table 2.1 presents deposition conditions and final permeation properties for several oxide membranes. Concentrating for the moment on the SiO<sub>2</sub> membranes, we note that the membranes produced by one-sided deposition have significantly higher permeation coefficients than those produced in the opposing reactants geometry. Opposing reactants deposition at 600 °C for as many as 5 hours was not sufficient for complete pore plugging and useful results were obtained only at 700 and 800 °C. Figure 2.2a shows the evolution of H<sub>2</sub> and N<sub>2</sub> permeances during deposition at 700 and 800 °C in the opposing reactants geometry. At 700 °C essentially complete pore plugging is attained within 3 hours, although continuing deposition after that time leads to further reduction in the permeances, especially that of N<sub>2</sub>, evidently due to densification and, possibly, slow thickening of the

already formed layer. At 800 °C the reaction is faster requiring about 1 hour for complete pore plugging. In one-sided deposition, by contrast, at 600 °C pore plugging is complete in less than 10 minutes, and even at 400 °C pore plugging takes less than 90 minutes. Figure 2.2b shows the evolution of H<sub>2</sub> and N<sub>2</sub> permeances during one-sided deposition at 600 °C and 400 °C.

The sharply different rates of the one-sided and opposing reactants deposition is due to the different level of reactant concentrations at the location of maximum deposition rate. In one-sided deposition, pore plugging occurs at or near the external surface where the reactant concentrations are near their free stream values. In the opposing reactant deposition, the reactant concentrations at the location of maximum rate are small fractions of their boundary values as shown schematically in Figure 2.3. The faster the reaction, the lower these concentrations and, hence, the larger the difference between the one-sided and the opposing reactants geometries.

Permeances of H<sub>2</sub> and N<sub>2</sub> through a SiO<sub>2</sub> film deposited at 800 °C were measured at 450 °C, 600 °C, and 800 °C, and the measurements plotted on an Arrhenius diagram (Figure 2.4) yielded activation energies of 37 kJ/mol for H<sub>2</sub> and 60 kJ/mol for N<sub>2</sub>. In earlier experiments with SiO<sub>2</sub> films produced by silane oxidation, we found that the activation energy for hydrogen permeation depends on the thermal history of the material, being as low as 6 kJ/mol for fresh films deposited in the absence of water vapor. The value of 37 kJ/mol for the film deposited at 800 °C is very close to that measured for fused quartz (Lee, 1963).

### **2.3.2 TiO<sub>2</sub> Deposition**

Table 2.1 includes several experiments of TiO<sub>2</sub> deposition and the permeation properties of the resulting films. The evolution of hydrogen and nitrogen permeation rates during TiO<sub>2</sub> deposition at 450 and 600°C is shown in Figure 2.5. Note that the

permeation rates were measured at the temperature of deposition. These rates are only slightly lower than those of the SiO<sub>2</sub> films produced in the opposing reactants geometry. The H<sub>2</sub>:N<sub>2</sub> permeation ratio varies from 200 to 1500 depending on the deposition time and temperature.

The TiO<sub>2</sub> films deposited at 800 °C had much lower permeance and H<sub>2</sub>:N<sub>2</sub> ratios. It is well known that in CVD of TiO<sub>2</sub> the deposition temperature strongly affects the crystallinity of the oxide deposited. There is also evidence from previous work that in TiO<sub>2</sub> supported on SiO<sub>2</sub>, the transition from the amorphous phase to anatase and the transition from anatase to rutile occurs at much higher temperatures than in the case of bulk TiO<sub>2</sub>. Reichmann and Bell (1987) have found such evidence in their investigation of the chemistry by which small crystallites of TiO<sub>2</sub> are produced on a silica support. They reported that although there is no chemical interaction between TiO<sub>2</sub> and SiO<sub>2</sub>, the silica support stabilizes the amorphous TiO<sub>2</sub> with respect to the phase transformation to anatase up to a calcination temperature above 550 °C, whereas bulk material is converted to anatase well below that temperature. They also found that the transition temperature from anatase to rutile is much higher in the presence of the silica support. There is no previous literature on the permeation of H<sub>2</sub> and N<sub>2</sub> through TiO<sub>2</sub>, but it is reasonable to assume that the amorphous oxide is more permeable than the crystalline material. The permeation measurements listed in Table 2.1 suggest that at some temperature between 600 and 800 °C, the deposited TiO<sub>2</sub> becomes crystalline resulting in lower hydrogen permeation. This possibility is consistent with some recent transmission electron microscopy observations we made on a TiO<sub>2</sub> layer deposited at 600 °C and subsequently heated at 800°C. The diffraction pattern of that layer was characteristic of the anatase structure.

The TiO<sub>2</sub> films listed in Table 2.1 and Figure 2.5 were all obtained in the opposing reactants geometry. Deposition experiments were also carried out in the one-sided mode under the conditions listed in Table 2.2. None of these experiments resulted in a significant

reduction of the  $N_2$  or  $H_2$  permeation; therefore, none produced a dense layer plugging the Vycor pores. The difference between  $SiO_2$  and  $TiO_2$  deposition is discussed in the section on deposition mechanism.

#### 2.3.4 $Al_2O_3$ Deposition

$Al_2O_3$  films were deposited by means of  $AlCl_3$  hydrolysis, reaction (3) in the opposing reactants geometry. Depositions were carried out at 450, 700, and 800 °C. The results are shown in Figure 2.6 and Table 2.1. As shown in Table 2.1, the permeance of hydrogen at 450 °C of  $Al_2O_3$  films deposited at 700 °C and 800 °C is substantially below that of the  $SiO_2$  films. The  $H_2:N_2$  permeation ratio was at most 400, also lower than that of  $SiO_2$ . The best results were obtained for films deposited at 450 °C and densified by annealing at 700 °C. In these films the  $H_2:N_2$  permeation ratio increased to 1000, but the permeation coefficient of hydrogen remained lower than that of  $SiO_2$  films. A few experiments listed in Table 2.2, conducted in one-sided geometry, did not produce pore plugging.

#### 2.3.5 $B_2O_3$ Deposition

$B_2O_3$  films were deposited by means of  $BCl_3$  hydrolysis, reaction (2). It was found that the hydrolysis reaction takes place over a wide temperature range (50 °C - 800 °C). However, the Vycor tubes containing  $B_2O_3$  layers deposited or annealed at temperatures above 500 °C have small  $H_2$  permeances, smaller than  $0.01 \text{ cm}^3(\text{STP})/\text{cm}^2\text{-atm-min}$  at 800 °C. Films deposited between 100-450 °C have hydrogen permeances as high as  $0.2 \text{ cm}^3(\text{STP})/\text{cm}^2\text{-atm-min}$  at 450 °C and  $0.03 \text{ cm}^3(\text{STP})/\text{cm}^2\text{-atm-min}$  at 150 °C. At the latter temperature the hydrogen permeation through  $SiO_2$  layers was negligible. Unfortunately, the permeances of the boria membranes decreased significantly upon heating these membranes at temperatures of 500 °C or higher. Figure 2.7 shows the

evolution of  $H_2$  and  $N_2$  permeances during  $B_2O_3$  deposition at  $150\text{ }^\circ\text{C}$ . When the  $B_2O_3$  films were exposed to laboratory humid air for several weeks, they developed boric acid whiskers and subsequently cracked due to interaction of water with  $B_2O_3$ . Figure 2.8 shows the effect of densification due to the heat treatment of a film deposited at  $150\text{ }^\circ\text{C}$ , as well as the dramatic increase in permeability after exposure to humid air for 23 days.

### **2.3.6 SEM and Electron Microprobe Analysis**

SEM of several sectioned tubes that had been treated by  $SiO_2$  deposition did not give any indication of the deposited  $SiO_2$  layer. Since the porous Vycor substrate is  $>96\%$   $SiO_2$ , and the deposited material pure  $SiO_2$ , the only effect of deposition is to increase the  $SiO_2$  density by about 16% (the void fraction) at the region of complete pore plugging which could be less than  $1\text{ }\mu\text{m}$  wide. A smaller increase in density would be distributed over a wider region of partial pore plugging. Evidently these differences are not discernible by SEM.

SEM and EPMA of tubes subjected to  $TiO_2$  deposition gave clear indication of the location and width of the region of  $TiO_2$  deposition. Figure 2.9a shows a typical electron backscattering micrograph of a polished cross section of a Vycor tube bearing an internal  $TiO_2$  layer deposited at  $600\text{ }^\circ\text{C}$ . The large fissure near the lower left is a crack generated by the cutting or polishing. The  $TiO_2$  deposit is the band of lines about  $100\text{ }\mu\text{m}$  below the top which in this case is the inside of the tube. The band is about  $30\text{-}40\text{ }\mu\text{m}$  thick and consists of a series of parallel lines. Figure 2.9b shows the  $TiO_2$  band at higher magnification. Figure 2.9c shows a polished cross section of a Vycor tube carrying a  $TiO_2$  layer deposited at  $450\text{ }^\circ\text{C}$ . The layer in the middle is again about  $100\text{ }\mu\text{m}$  from the internal tube surface at the bottom. This  $TiO_2$  layer shows the same kind of uniformly striated structure observed for the film deposited at  $600\text{ }^\circ\text{C}$ . At this time we have no explanation for the striation in the  $TiO_2$  layer.

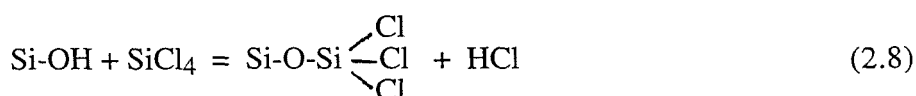
The scanning electron microscopy was supplemented by measurements of the elemental composition profile across the polished tube section shown in Figure 2.9 by electron probe microanalysis. Figures 2.10a and b show the relative density profiles of  $\text{TiO}_2$  for the 600 °C and 450 °C deposition respectively. The main features of these figures is the gradual rise of the  $\text{TiO}_2$  profile from the side of the  $\text{TiCl}_4$  flow (inside of Vycor tube) and steep decline towards the side of the  $\text{H}_2\text{O}$ . Significant  $\text{TiO}_2$  is present over about 100  $\mu\text{m}$  region although the region of totally plugged pores is much thinner as evidenced by the sharp maximum in the profile. The profiles in Figures 2.10a and b do not show the striated structure of the  $\text{TiO}_2$  layer, probably because of the lower resolution of EPMA compared to that of SEM.

The SEM and EPMA results show several unexpected features. First there is the location of the deposition region. The concentration of the reactants  $\text{TiCl}_4$  and  $\text{H}_2\text{O}$  were chosen inversely proportional to their Knudsen diffusion coefficients, so that the reaction region may be located exactly at the midpoint of the tube wall, according to a simple model of diffusion limited reaction. Instead the reaction region was much closer to the  $\text{TiCl}_4$  side. The same trend was observed for the  $\text{Al}_2\text{O}_3$  films as shown in the Al/Si ratio profile given in Figure 2.11. A second unexpected feature is the asymmetric nature of Al and Ti profiles. In the case of the  $\text{TiO}_2$  films, one can also notice in the SEM micrographs the difference in the texture of the regions separated by the striation. The region extending from the  $\text{TiCl}_4$  side to the location of the maximum deposit density is smooth, whereas at the opposite side of the layer the texture seems granular. As shown in the EPMA profile, the smooth region is coated with  $\text{TiO}_2$  all the way from the inside of the tube to the peak of the deposited layer.

### 2.3.7 Reaction Mechanism

The brief discussion that follows deals with some general features of the reaction mechanism and not with the detailed chemical mechanism which is outside the scope of this work and should be approached by different type of experiments. The main question addressed here is whether deposition occurs via a homogeneous precursor or is strictly heterogeneous. In the first case the gas phase reaction between chloride and water molecules would produce oligomer molecules, or particles, which could then form a layer on the pore surface. In the second case the chloride molecule and water would react directly with sites on the solid surface. We shall consider the reactions of  $\text{SiCl}_4$  and  $\text{TiCl}_4$  separately, for as we have seen these two reactions have shown qualitatively different trends, especially in one-sided deposition.

There is a significant body of work concerning the reactions of gaseous  $\text{SiCl}_4$  and other chlorosilanes with the surface hydroxyl groups of silica gels. Reaction of  $\text{SiCl}_4$  or  $\text{CH}_3\text{SiCl}_3$  with isolated silica surface hydroxyl groups takes place with elimination of  $\text{HCl}$  to form a  $\text{SiOSi}$  bond, and at  $280^\circ\text{C}$  this reaction was complete within one hour (Armistead and Hockey, 1967). Hydrogen bonded-OH groups on the other hand reacted much more slowly. When the surface treated by the chloride was exposed to water vapor at the reaction temperature, the -OH groups reappeared, i.e., the Si-Cl groups hydrolyzed to Si-OH and  $\text{HCl}$ . Simultaneously with these reactions between  $\text{SiCl}_4$  or  $\text{H}_2\text{O}$  in the gas and -OH and -Cl groups in the solid, condensation reactions between two -OH groups or a -OH and a -Cl group in the solid result in cross linking by formation of siloxane bonds. Thus exposure of the silica surface to a gaseous mixture containing  $\text{SiCl}_4$  and  $\text{H}_2\text{O}$  at temperatures above  $250^\circ\text{C}$  is expected to result in the growth of a partially hydroxylated  $\text{SiO}_2$  layer by the reactions





In contrast to the reaction of gaseous  $\text{SiCl}_4$  with surface hydroxyl groups, the gas phase reaction between  $\text{SiCl}_4$  and  $\text{H}_2\text{O}$  at temperatures below  $900^\circ\text{C}$  is virtually uncharted territory. We know only one report (Hudson, 1947) of kinetic experiments of gas phase hydrolysis of  $\text{SiCl}_4$ ,  $\text{TiCl}_4$  and  $\text{SnCl}_4$ .

Titanium oxide deposition was shown earlier to have features distinct from those of  $\text{SiO}_2$ . In the opposing reactants geometry,  $\text{TiO}_2$  deposition is much faster, at  $450^\circ\text{C}$  requiring about 30 minutes for complete pore plugging compared to the 60 minutes required for pore plugging by  $\text{SiO}_2$  at  $800^\circ\text{C}$ . However, in one-sided deposition, pore plugging by  $\text{TiO}_2$  was not achieved. The literature provides some interesting information about the reactions of  $\text{TiCl}_4$  with hydroxylated surfaces. Armistead et al. (1969) found that  $\text{TiCl}_4$  vapors react with surface hydroxyls of silica gel at room temperature to give  $\text{Si-O-TiCl}_3$  and  $(\text{Si-O})_2\text{TiCl}_2$  groups. Hair and Hertl (1973) found that gaseous  $\text{TiCl}_4$  reacts with hydroxyl groups on silica gel very rapidly even at room temperature. Tolmachev and Okatov (1984) passed alternatively  $\text{TiCl}_4$  and  $\text{H}_2\text{O}$  over a powder of Vycor glass at  $180^\circ\text{C}$  and observed a layer by layer growth of titanium oxide. Evidently the  $\text{Ti-Cl}$  groups hydrolyze to  $\text{Ti-OH}$ , which can once more react with  $\text{TiCl}_4$ . These reactions were not examined in the temperature range relevant to our experiments,  $400\text{-}600^\circ\text{C}$ , but the direct heterogeneous mechanism remains plausible for the opposing reactants deposition.

The failure to achieve pore plugging in one-sided deposition of  $\text{TiO}_2$  is rather puzzling. However, a tentative explanation can be found in the relatively high rate of the homogeneous reaction. The gas phase reaction between  $\text{TiCl}_4$  and  $\text{H}_2\text{O}$  is known to be much faster than the analogous reaction of  $\text{SiCl}_4$  (Hudson, 1947). In the opposing reactants geometry the heterogeneous mechanism is dominant because of the high surface

area and the low concentration of reactants. Any oligomers formed homogeneously would diffuse away from the reaction zone rather slowly and would more likely become trapped by the surface contributing to the overall growth of the deposit layer. In one-sided deposition, however, the homogeneous reaction depletes the reactants thus suppressing the direct heterogeneous reactions. At the same time the oligomers and particles formed in the gas phase have relatively low diffusion coefficients and are much more likely to be advected away from the reaction zone than to diffuse and become attached on the internal surface.

The deposition of  $\text{Al}_2\text{O}_3$  layers followed a pattern similar to that of  $\text{TiO}_2$ . The opposing reactants geometry yielded complete pore plugging at temperatures as low as  $450^\circ\text{C}$ , but in one-sided deposition complete pore plugging was not achieved, at least in the experiments listed in Table 2.2. The same considerations regarding reaction mechanisms as in the  $\text{TiO}_2$  case apply here too, since  $\text{AlCl}_3$  is known to react rapidly with water in the gas phase (Wong and Robinson, 1970). Deposition of  $\text{B}_2\text{O}_3$  has some distinct features. One is the high reactivity of  $\text{BCl}_3$  with surface hydroxyls, the reaction proceeding even at room temperature (Hair and Hertl, 1973). Another is the ease of hydrolysis of  $\text{B}_2\text{O}_3$  to boric acid which may explain the formation of whiskers and cracks upon prolonged exposure to laboratory air.

## 2.4 CONCLUSIONS

Hydrogen permeable membranes were synthesized by depositing layers of amorphous  $\text{SiO}_2$ ,  $\text{TiO}_2$ ,  $\text{Al}_2\text{O}_3$  and  $\text{B}_2\text{O}_3$  within the pores of Vycor tubes using the reaction of the respective chloride vapors ( $\text{SiCl}_4$ , etc.) with water vapor. The membranes obtained by  $\text{SiO}_2$  deposition have permeances of  $0.1 - 0.3 \text{ cm}^3/\text{cm}^2\text{-atm-min}$  and  $\text{H}_2:\text{N}_2$  permeation ratios of 3000-5000 at  $450^\circ\text{C}$ . These permeances include the resistance of the Vycor tube

wall as well as the resistance of the deposited layer. The membranes containing the other oxides have somewhat lower permeances.

Silica membranes can be synthesized by opposing reactants deposition and by one-sided deposition, the latter resulting in thinner deposited layers and higher permeances. Within the range of conditions employed, titania and alumina membranes were obtained only in the opposing reactants deposition, the one-sided deposition failing to produce pore plugging. A direct heterogeneous mechanism seems to be responsible for the opposing reactants deposition of all four oxides. It also explains the one-sided deposition of  $\text{SiO}_2$ . However, the rapid homogeneous reaction between  $\text{TiCl}_4$  and  $\text{H}_2\text{O}$  or  $\text{AlCl}_3$  and  $\text{H}_2\text{O}$  seems to interfere with the one-sided deposition of  $\text{TiO}_2$  and  $\text{AlO}_3$ .

## **ACKNOWLEDGMENT**

Funding by the Department of Energy with UCR Grant DE-FG22-89PC89765 and Contract DE-AC21-90MC26365 is gratefully acknowledged.

**LITERATURE CITED**

Armistead, C. G. and Hockey, J. A. Reactions of Chloromethyl Silanes with Hydrated Aerosil Silicas. *Trans. Farad. Soc.* **1967**, *63*, 2549-2556.

Armistead, C. G., Tyler, A. J., Hambleton, F. H., Mitchell, S. A. and Hockey, J. A. The Surface Hydroxylation of Silica. *J. Phys. Chem.* **1969**, *73*(11), 3947-3953.

Boyd, D. C. and Thompson, D. A. Glass in Kirk-Othmer Encyclopedia of Chemical Technology, **1980**, *11*, 807-880.

Gavalas, G. R., Megiris, C. E. and Nam, S. W. Deposition of H<sub>2</sub>-Permselective SiO<sub>2</sub> Films. *Chem. Eng. Sci.* **1989**, *44*(9), 1829-1835.

Gavalas, G. R. and Megiris, C. E. Synthesis of SiO<sub>2</sub> Membrane on Porous Support and Method of Use of Same. U.S. Patent 4,902,307, **1990**.

Hair, M. L. and Hertl, W. Chlorination of Silica Surfaces. *J. Phys. Chem.* **1973**, *77*(17), 2070-2075.

Hudson, R. F. The Vapor Phase Hydrolysis of Non-metallic Chlorides. Proceedings International Congress of Pure and Applied Chemistry, **1947**, 297-305.

Lee, R. W. Diffusion of Hydrogen in Natural and Synthetic Fused Quartz. *J. Chem. Phys.* **1963**, *38*(2), 448-455.

Leiby, Jr., C. C. and Chen, C. L. Diffusion Coefficients, Solubilities and Permeabilities for He, Ne, H<sub>2</sub>, and N<sub>2</sub> in Vycor Glass. *J. Appl. Phys.* **1960**, 31(2), 268-274.

Nam, S. W. and Gavalas, G. R. Stability of H<sub>2</sub>-Permselective SiO<sub>2</sub> Films Formed by Chemical Vapor Deposition. *AIChE Symposium Series* **1989**, 85 (268), 68-74.

Reichmann, M. G. and Bell, A. T. Raman Study of the Preparation of SiO<sub>2</sub>-Supported TiO<sub>2</sub> from TiCl<sub>4</sub> and HCl. *Langmuir* **1987**, 3(1), 111-116.

Shelby, J. E. Molecular Solubility and Diffusion in Treatise on Materials Science and Technology, M. Tomozawa and R. H. Doremus (Eds.) **1979**, Vol. 17, 1-40.

Tolmachev, V. A. and Okatov, M. A. Investigation of Process for Synthesizing Ultrathin Titanium Oxide Layers in Porous Glass. *Sov. J. Opt. Technol.* **1984**, 51(2), 104-107.

Wong, P. and Robinson, M. Chemical Vapor Deposition of Polycrystalline Al<sub>2</sub>O<sub>3</sub>. *J. Am. Ceram. Soc.* **1970**, 53(11), 617-621.

**Table 2.1. Conditions of Deposition and Permeances of the Resulting Membranes.**

Code	Oxide	Reaction Geometry	Reactants (atm)		Reaction Temp (°C)	Reaction Time (min)	Gas Permeance $\left(\frac{\text{cm}^3(\text{STP})}{\text{cm}^2\cdot\text{min}\cdot\text{atm}}\right)$			
			Chloride	H <sub>2</sub> O			at 450°C		at Deposition T	
							H <sub>2</sub>	N <sub>2</sub>	H <sub>2</sub>	N <sub>2</sub>
S1	SiO <sub>2</sub>	opposing	0.30	0.07	700	180	0.03	2.5x10 <sup>-5</sup>	0.09	30x10 <sup>-5</sup>
S2	SiO <sub>2</sub>	opposing	0.30	0.07	800	90	0.02	0.65	0.11	7.5
S3	SiO <sub>2</sub>	one-sided	0.15	0.04	800	25	0.09	8	0.29	150
S4	SiO <sub>2</sub>	one-sided	0.15	0.04	600	10	0.28	7	0.43	70
S5	SiO <sub>2</sub>	one-sided	0.15	0.04	400	95	0.08	500	0.07	400
S6	SiO <sub>2</sub>	one-sided	0.02	0.025	600	55	0.35	50	0.53	250
A1	Al <sub>2</sub> O <sub>3</sub>	opposing	0.20	0.07	800	120	0.003	5.5	0.02	28
A2	Al <sub>2</sub> O <sub>3</sub>	opposing	0.20	0.07	450	60	0.004	2.4	0.01	2.4
A3	Al <sub>2</sub> O <sub>3</sub>	opposing	0.20	0.07	450	30	0.03	6.3	0.03	6.3
A4*	Al <sub>2</sub> O <sub>3</sub>	opposing	0.20	0.07	450	30	0.01	1.5	0.01	1.5
B1	B <sub>2</sub> O <sub>3</sub>	opposing	0.10	0.10	450	105	0.1	2.0	0.10	2
B2	B <sub>2</sub> O <sub>3</sub>	one-sided	0.10	0.10	500	10	-	-	0.30	40
B3	B <sub>2</sub> O <sub>3</sub>	opposing	0.10	0.10	150	90	-	-	0.03	5
T1	TiO <sub>2</sub>	opposing	0.20	0.12	450	35	0.09	59	0.09	59
T2	TiO <sub>2</sub>	opposing	0.20	0.12	450	60	0.06	3.8	0.06	3.8
T3	TiO <sub>2</sub>	opposing	0.20	0.12	600	35	-	-	0.17	38
T4	TiO <sub>2</sub>	opposing	0.20	0.12	600	60	-	-	0.08	5.9
T5	TiO <sub>2</sub>	opposing	0.20	0.12	800	50	-	-	0.02	110
untreated	-	-	-	-	-	-	0.7	19,000	-	-

\*same as A3 but annealed at 700°C overnight after deposition

Table 2.2. One-Sided Deposition Experiments Which Did Not Result in Pore Plugging Within Two Hours of Reaction.

Code	Oxide	Reactants (atm) H <sub>2</sub> O	chloride	Reaction temperature (°C)	Comment
A5*	Al <sub>2</sub> O <sub>3</sub>	0.10	0.04	200	
A6*	Al <sub>2</sub> O <sub>3</sub>	0.10	0.04	600	
A7*	Al <sub>2</sub> O <sub>3</sub>	0.10	0.04	800	
B4**	B <sub>2</sub> O <sub>3</sub>	0.10	0.10	150	
B3**	B <sub>2</sub> O <sub>3</sub>	0.10	0.10	400	
T6	TiO <sub>2</sub>	0.12	0.20	450	substrate remains clear
T7	TiO <sub>2</sub>	0.12	0.20	600	substrate remains clear
T8	TiO <sub>2</sub>	0.12	0.20	200	substrate remains clear
T9	TiO <sub>2</sub>	0.12	0.01	450	white film formed
T10	TiO <sub>2</sub>	0.12	0.01	600	white film formed
T11	TiO <sub>2</sub>	0.12	0.01	300	homogeneous reaction particles

\* no permeation change

\*\* slow permeation change

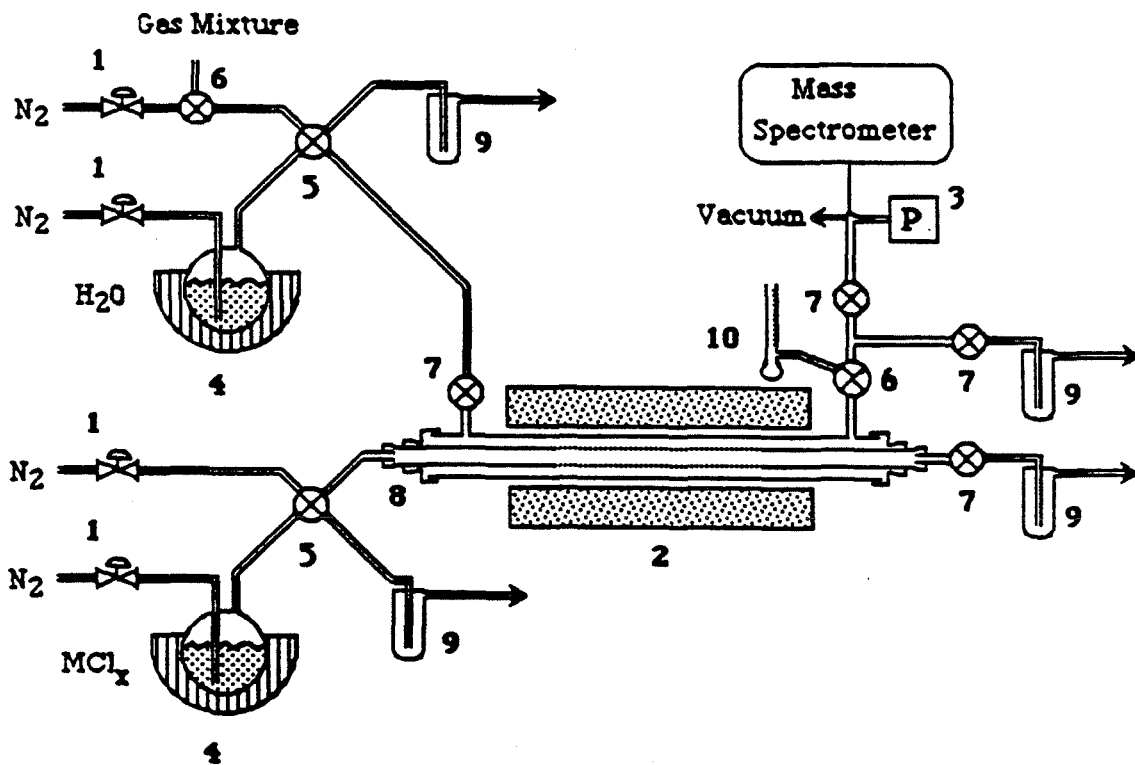


Figure 2.1a Schematic of the reactor system for opposing reactants deposition. 1. mass flowmeter with valve; 2. furnace with temperature controller; 3. pressure transducer; 4. bubbler with heating element and temperature controller; 5. 4-way valve; 6. 3-way valve; 7. on-off valve; 8. special fitting; 9. scrubber; 10. bubble flowmeter.

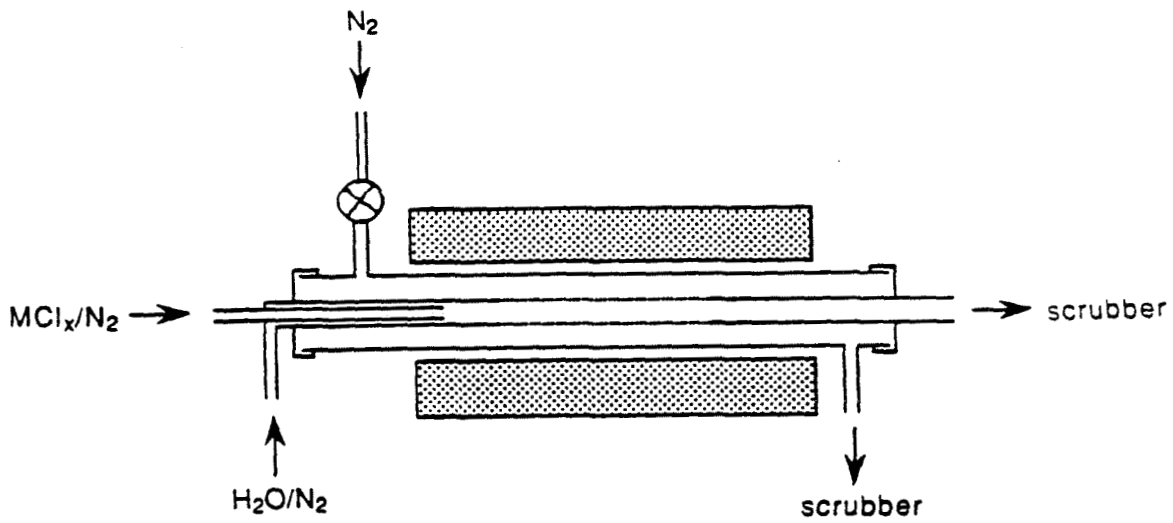


Figure 2.1b Schematic of reactant inlet for one-sided deposition.

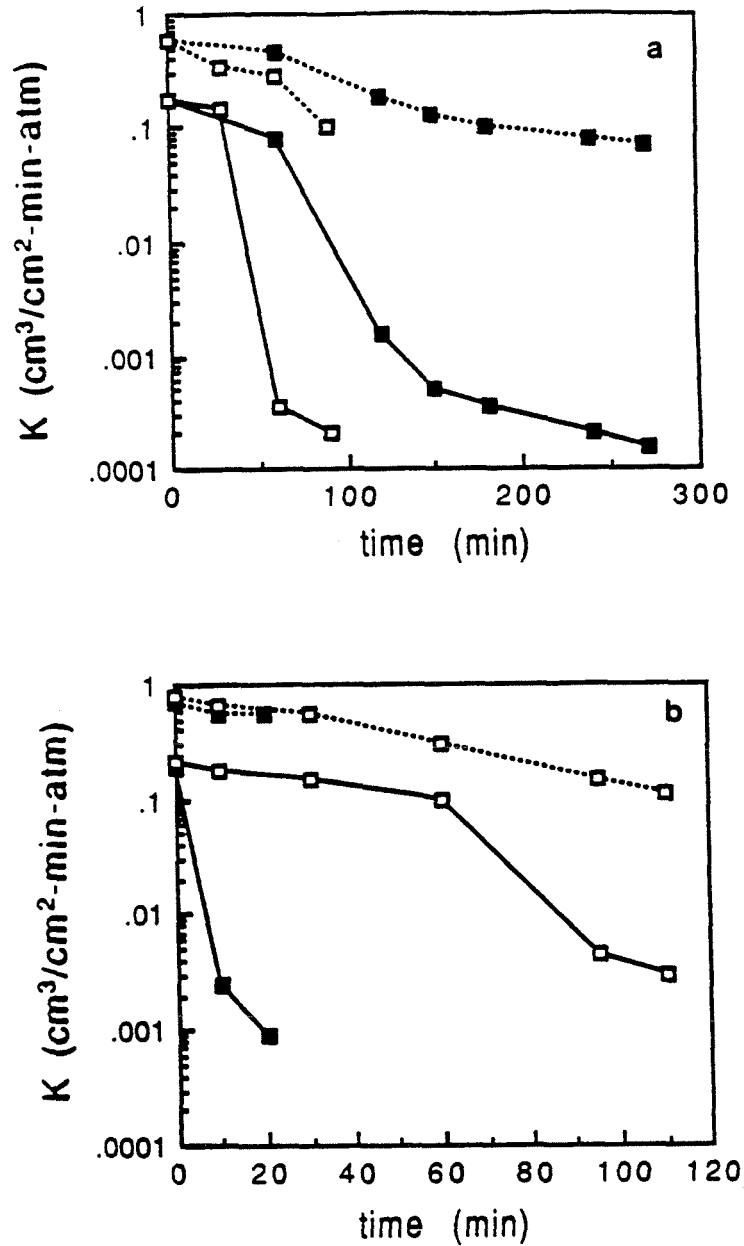


Figure 2.2 Permeances at deposition temperatures for hydrogen (---) and nitrogen (—) versus time of deposition by  $\text{SiCl}_4$  and  $\text{H}_2\text{O}$  reaction.

a: opposing reactants geometry at 700°C (■); and 800°C (□). Reactant streams were 7%  $\text{H}_2\text{O-N}_2$  and 30%  $\text{SiCl}_4\text{-N}_2$ .

b: one-sided deposition at 600°C (■) and 400°C (□). Reactant stream was 4%  $\text{H}_2\text{O}$  - 15%  $\text{SiCl}_4$  in  $\text{N}_2$ .

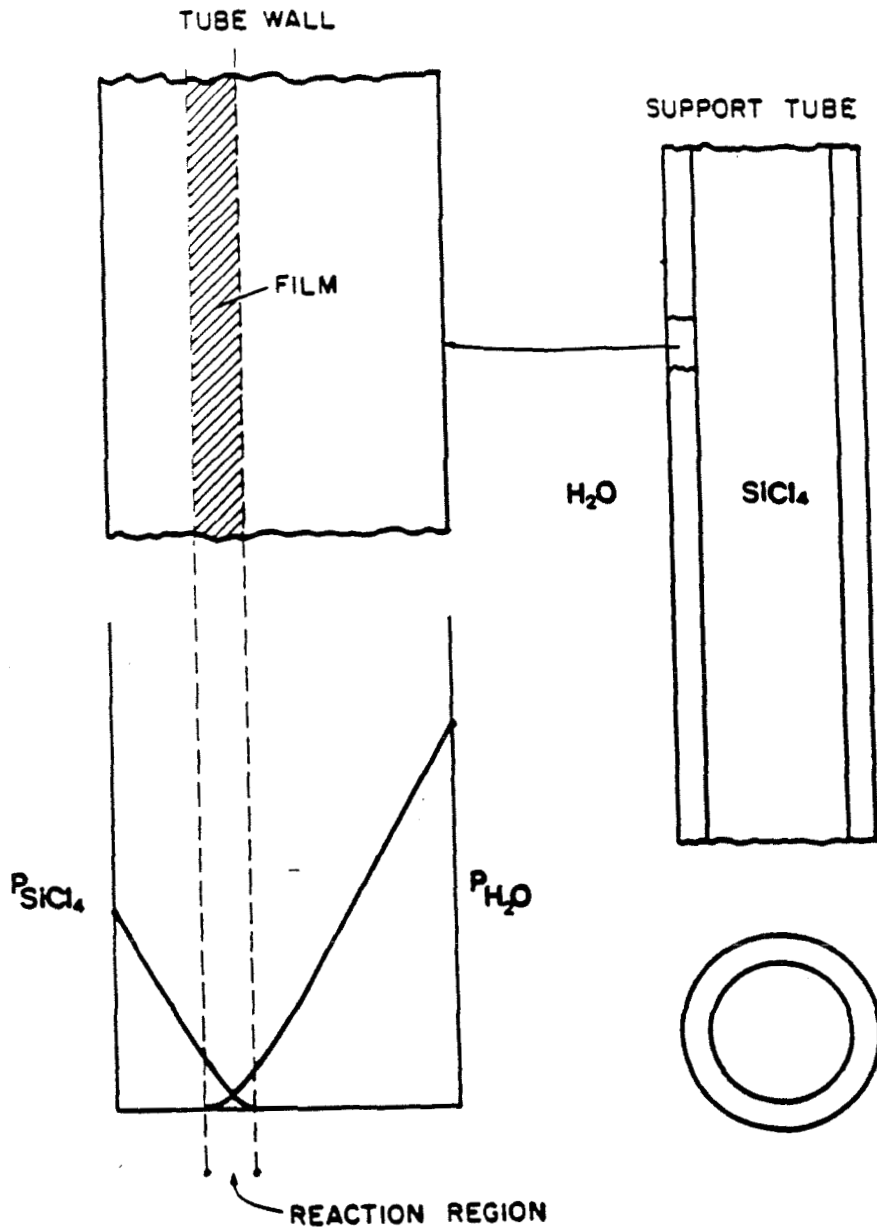


Figure 2.3 Schematic of concentration profiles in opposing reactants deposition.

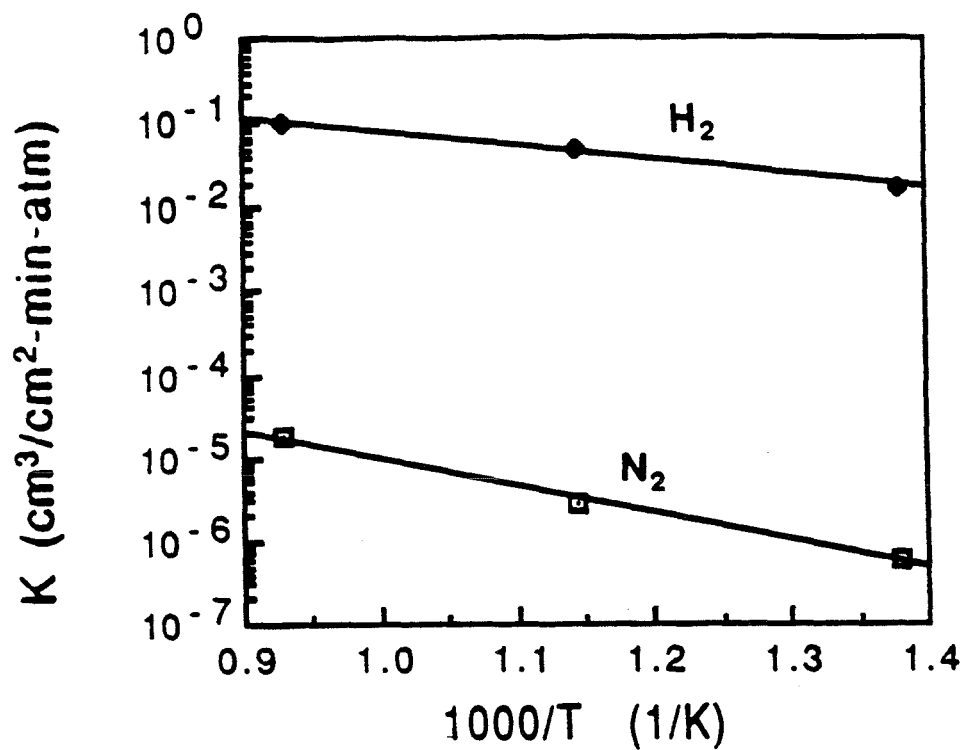


Figure 2.4 Arhenius plots for  $\text{H}_2$  and  $\text{N}_2$  permeances of  $\text{SiO}_2$  membranes.  $E_{\text{H}_2} = 37$  kJ/mol,  $E_{\text{N}_2} = 60$  kJ/mol.

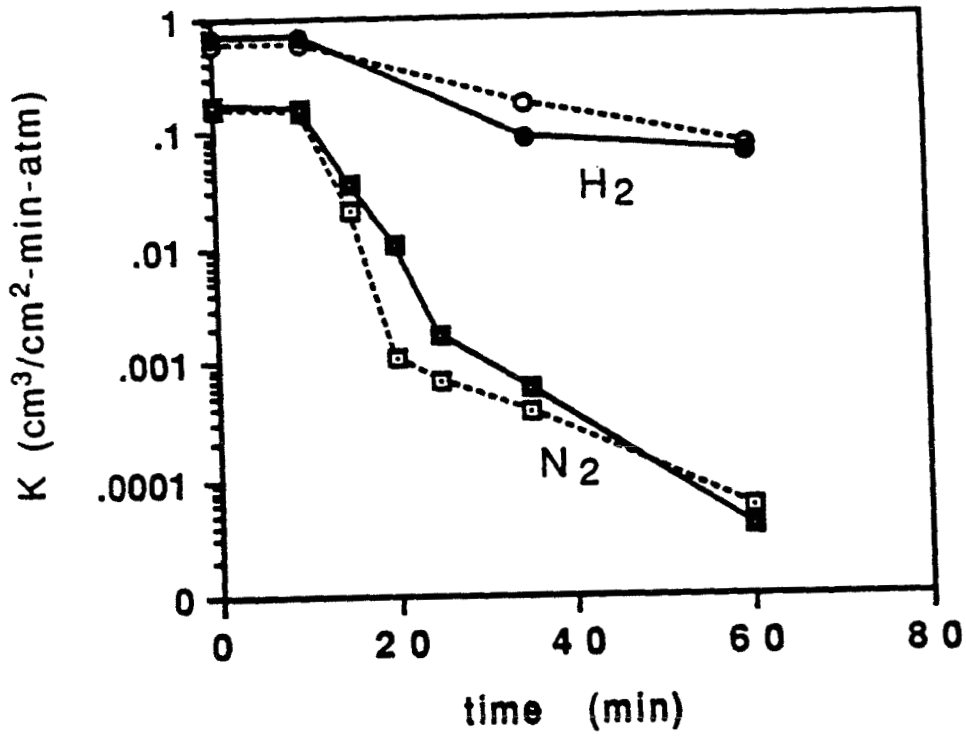


Figure 2.5 Nitrogen ( $\square, \blacksquare$ ) and hydrogen ( $\circ, \bullet$ ) permeation coefficients of  $\text{TiO}_2$  membranes during deposition at  $450^\circ\text{C}$  (—) and  $600^\circ\text{C}$  (- - -). Reactants: 20%  $\text{TiCl}_4\text{-N}_2$  and 12%  $\text{H}_2\text{O-N}_2$ .

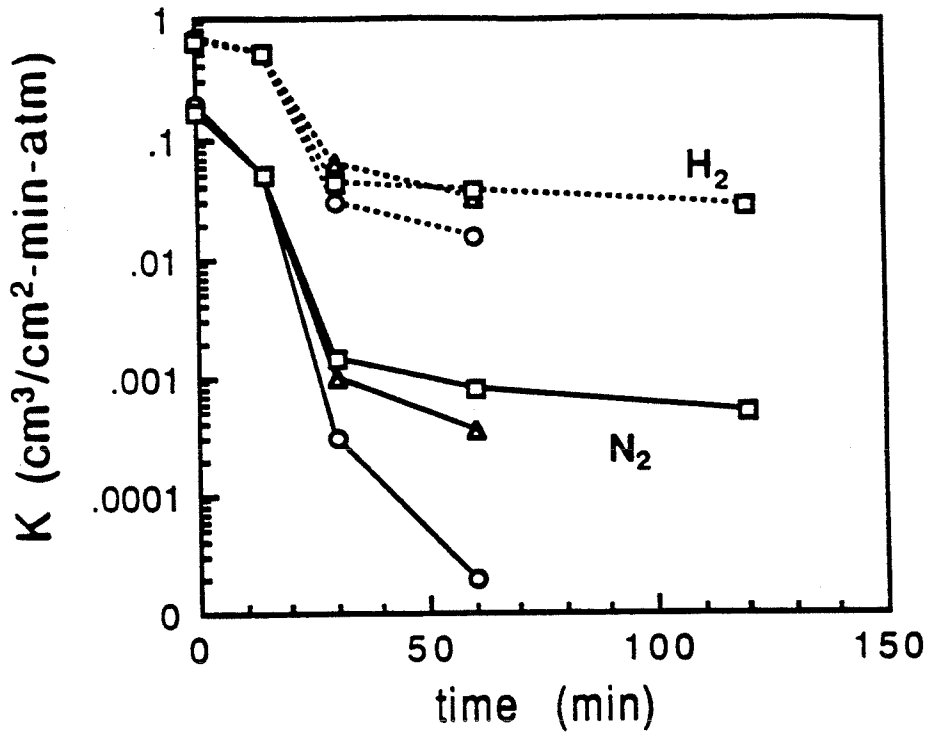


Figure 2.6 Permeances measured at deposition temperatures for hydrogen (---) and nitrogen (—) versus time of  $\text{AlCl}_3 + \text{H}_2\text{O}$  reaction at 450°C (o), 700°C ( $\Delta$ ), 800°C ( $\square$ ). Reactant streams were 7%  $\text{H}_2\text{O}-\text{N}_2$  and 20%  $\text{AlCl}_3-\text{N}_2$  in opposing reactants geometry.

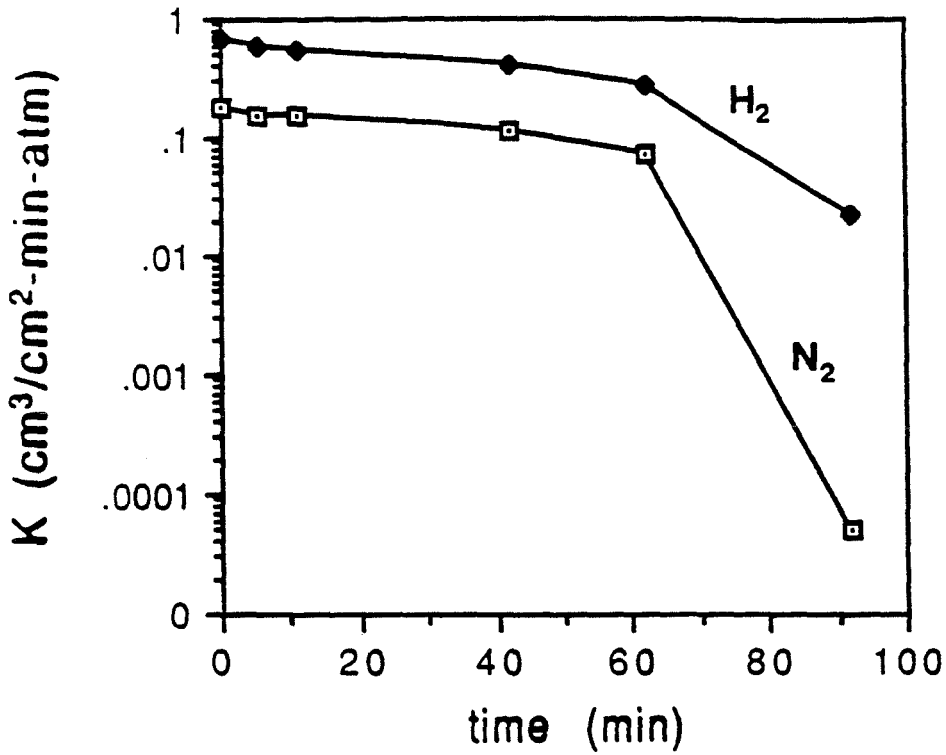


Figure 2.7 Hydrogen and nitrogen permeances at  $150^\circ\text{C}$  during deposition of  $\text{B}_2\text{O}_3$  at  $150^\circ\text{C}$  in opposing reactants geometry. Reactant streams: 10%  $\text{BCl}_3\text{-N}_2$  and 10%  $\text{H}_2\text{O-O}_2$ .

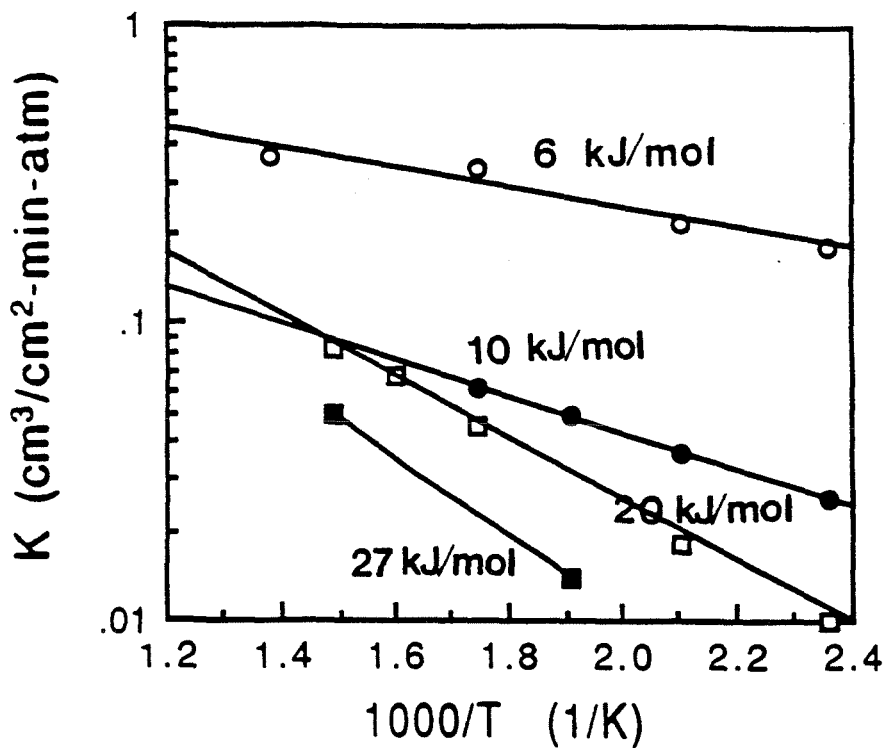


Figure 2.8 Hydrogen permeances of a  $B_2O_3$  membrane deposited at  $150^\circ\text{C}$  and annealed under dry  $N_2$  at  $400^\circ\text{C}$  overnight (■),  $300^\circ\text{C}$  (□) overnight,  $150^\circ\text{C}$  overnight (●) and exposed to laboratory air at room temperature for 23 days (○). Calculated activation energies are given on the figure.

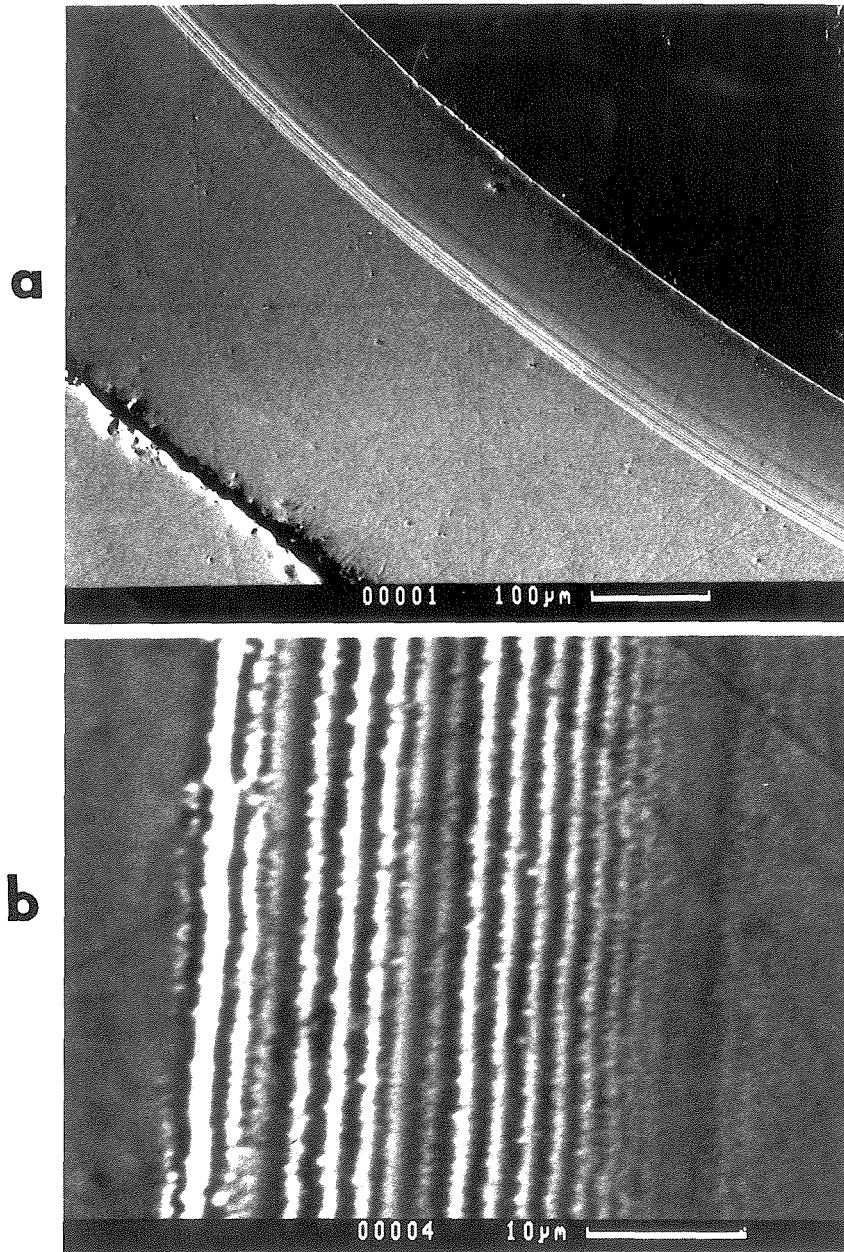


Figure 2.9 Scanning electron micrographs of tube cross sections containing TiO<sub>2</sub> deposited at 600 °C (a,b) and at 450 °C (c).

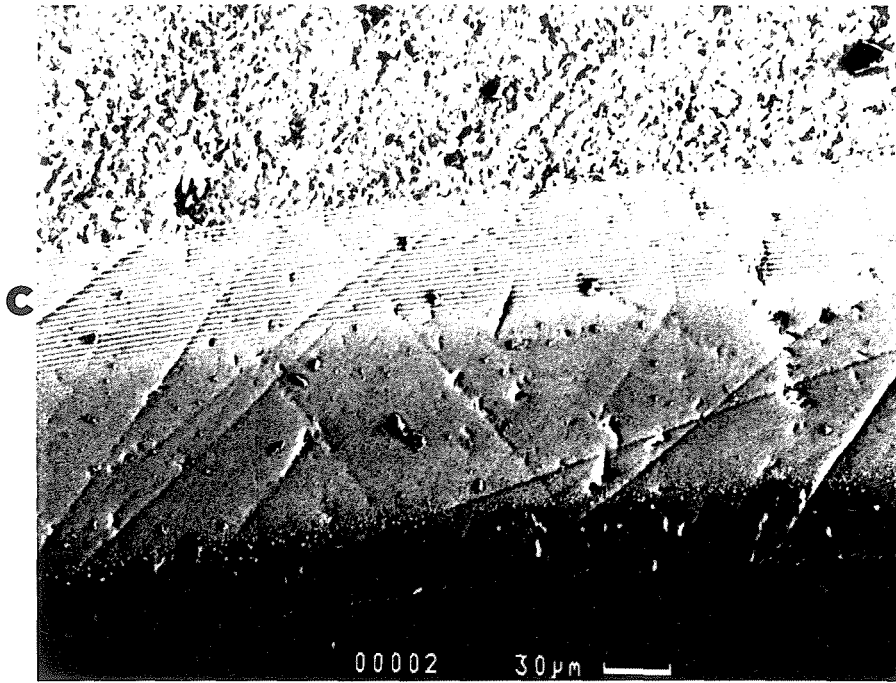


Figure 2.9 (cont.)

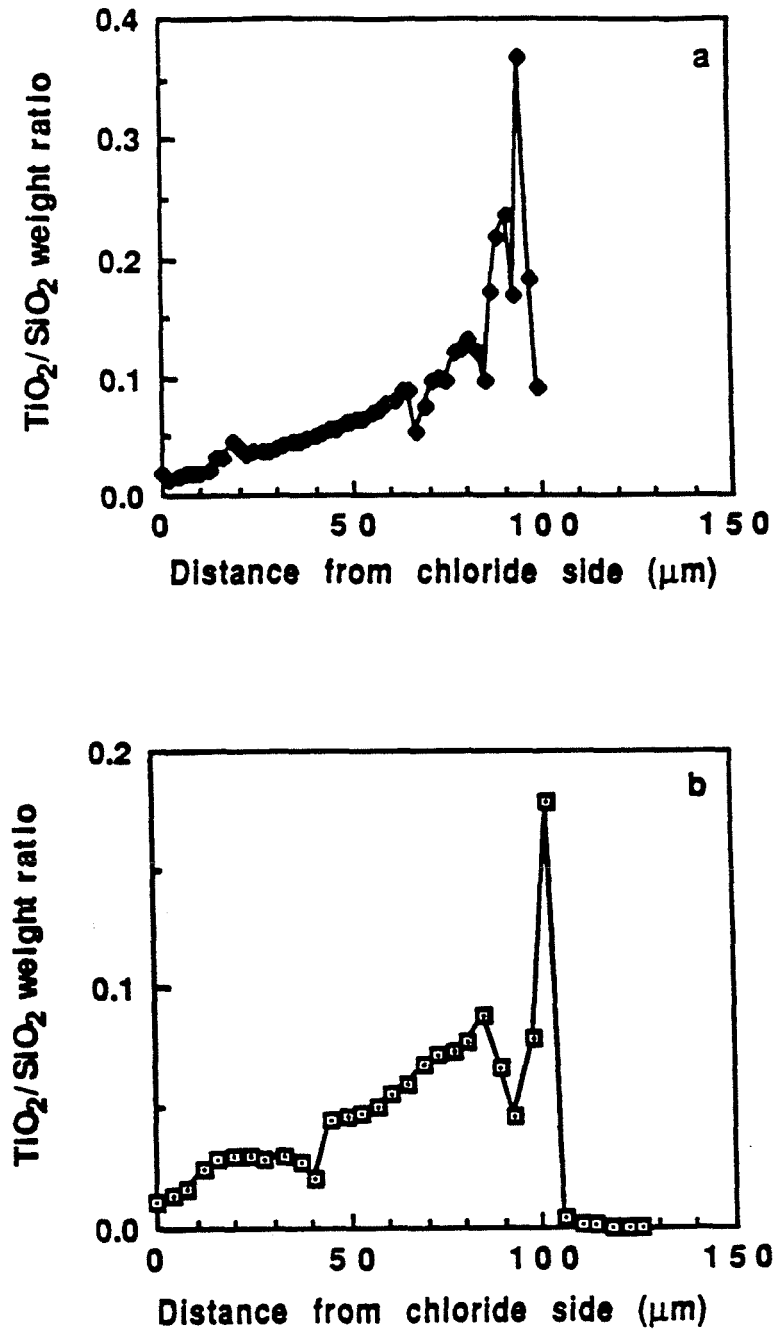


Figure 2.10 EPMA linescan of tube cross sections containing TiO<sub>2</sub> layers deposited at 600°C (a) and 450°C (b).

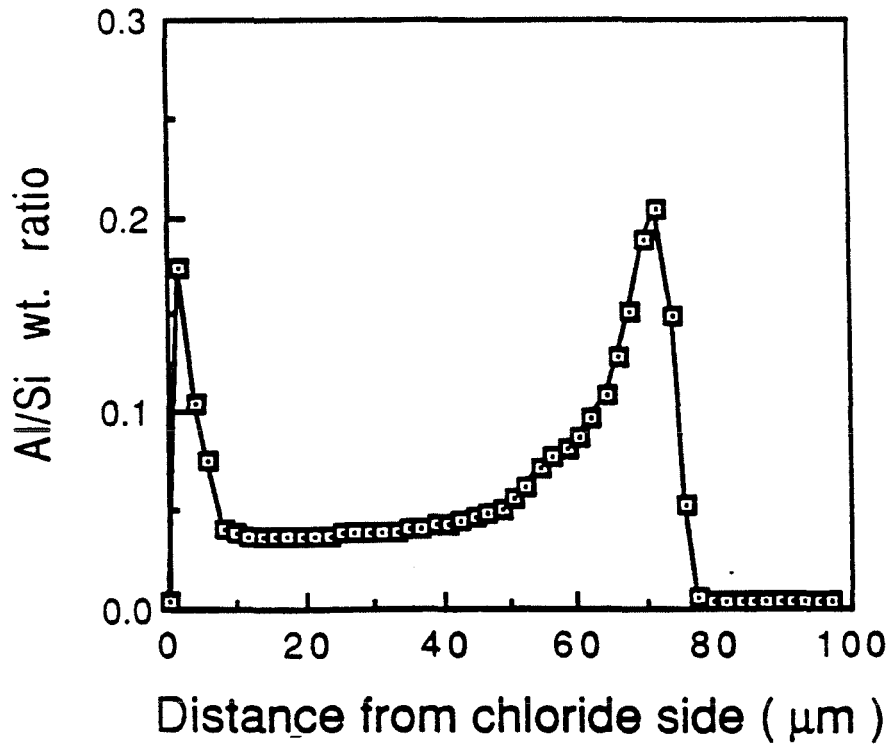


Figure 2.11 EPMA linescan of a tube cross section containing an  $\text{Al}_2\text{O}_3$  layer deposited by  $\text{AlCl}_3$  hydrolysis at  $800^\circ\text{C}$  in an opposing reactants geometry. Reactant streams were 7%  $\text{H}_2\text{O}-\text{N}_2$  and 20%  $\text{AlCl}_3-\text{N}_2$ .

## **CHAPTER 3**

### **A Kinetic Model of Membrane Formation by CVD of SiO<sub>2</sub> and Al<sub>2</sub>O<sub>3</sub>**

Published *AIChE J.* **38**, 847 (1992)

# A Kinetic Model of Membrane Formation by CVD of SiO<sub>2</sub> and Al<sub>2</sub>O<sub>3</sub>

Michael Tsapatsis and George Gavalas

*Department of Chemical Engineering, California Institute of Technology,  
Pasadena, CA 91125*

## ABSTRACT

Silica and alumina layers deposited into the walls of porous Vycor tubes by chloride hydrolysis in an opposing reactants geometry have been characterized by scanning electron microscopy and electron microprobe analysis. The layers are asymmetric, having a long tail towards the side of the chloride flow and a sharp boundary at the other side. The deposit thickness is several tenths of microns while the totally plugged region is of order of one micron.

A model has been developed describing reaction, diffusion, and evolution of the porous structure in the Vycor substrate due to the accumulation of the solid product. The deposition reaction is described by transient kinetics in terms of the concentrations of silanol and chloride groups in the product layer, as well as the concentrations of the gaseous reactants. The model is capable of generating deposit profiles in good agreement with those measured by electron microprobe analysis.

### 3.1 INTRODUCTION

Chemical vapor deposition (CVD) is a versatile technique widely used in the manufacture of electronic and optical devices. It has also been used for making the electrolyte layers of solid oxide fuel cells (Isenberg, 1981; Carolan and Michaels, 1987). CVD of  $\text{SiO}_2$  and other oxides on porous Vycor tubes has been used in our laboratory to prepare hydrogen membranes capable of operation at elevated temperatures. In our first experiments we used  $\text{SiH}_4$  oxidation to deposit  $\text{SiO}_2$  (Gavalas et al., 1989), but later turned to the hydrolysis of  $\text{SiCl}_4$ ,  $\text{TiCl}_4$ , or  $\text{AlCl}_3$ ,  $\text{BCl}_3$  to deposit  $\text{SiO}_2$ ,  $\text{TiO}_2$ ,  $\text{Al}_2\text{O}_3$  and  $\text{B}_2\text{O}_3$ , all selectively permeable to hydrogen (Tsapatsis et al., 1991). Deposition was carried out in the opposing reactants geometry, i.e., by applying flows of the chloride and water at opposite sides of the porous tube wall. Deposition of  $\text{SiO}_2$ , but not of the other oxides, was also possible in the one-sided geometry—both reactants flowing at the same side of the porous support.

*The one-sided geometry is the one used in film deposition on nonporous substrates and in chemical vapor infiltration (CVI) in porous substrates. When the latter process is employed for composite materials fabrication, it is essential that the product solid fills the porous substrate completely. By contrast, membrane preparation requires the deposit layer to be as thin as possible to achieve high flux of the permeate gas. Scanning electron microscopy and electron microprobe analysis of the  $\text{SiO}_2$  and  $\text{Al}_2\text{O}_3$  deposit layers deposited within the porous substrate show that the density of the product oxide ( $\text{SiO}_2$ ,  $\text{Al}_2\text{O}_3$ ) is not uniform across the deposit layer. There is a sharp peak at the point of pore plugging and a much wider region of lower deposit density. Only the region of pore plugging serves a useful membrane function, while the partially plugged region decreases the membrane permeance without improving materially the membrane selectivity. The present study was focused on understanding how the density profile of the deposit layer is*

influenced by the deposition chemistry and the operating conditions, with the goal of preparing improved membranes.

Deposition within a porous substrate involves reaction, diffusion, and gradual pore closure, a problem that has received considerable attention in the chemical engineering literature during the last ten years in the context of lime sulfation and other gas-solid reactions. In this paper we emphasize the deposition kinetics and treat the transport features of the problem in a simple fashion. Depending on the gas composition and pressure, the nature of the substrate, the temperature and the contact scheme, CVD processes may be dominated by homogeneous or heterogeneous reactions or both may be equally important. In the opposing reactants deposition employed in our experiments, heterogeneous reactions are expected to be dominant because of the high surface area of the microporous substrate (mean pore size 40 Å, BET surface area 200 m<sup>2</sup>/g). In one-sided deposition, on the other hand, gas phase reactions outside of the substrate may become important and may, in fact, prevent the deposition of a permselective layer. Such seems to be the case with the AlCl<sub>3</sub>-H<sub>2</sub>O and TiCl<sub>4</sub>-H<sub>2</sub>O systems (Tsapatsis et al., 1991).

Heterogeneous kinetics are often formulated assuming that the surface is at pseudosteady state with respect to the fluid phase, thus permitting the expression of the reaction rate solely in terms of gaseous concentrations. Such pseudosteady kinetics are commonly employed to describe CVD and CVI (Carolan and Michaels, 1987; Sotirchos, 1991). The pseudosteady assumption is valid provided that the characteristic time of deposition is much larger than the characteristic relaxation time of surface species concentrations. Otherwise, the surface reaction must be described by transient kinetics. In the deposition of SiO<sub>2</sub>, for example, a surface exposed to gaseous SiCl<sub>4</sub> and H<sub>2</sub>O might eventually develop a steadily growing deposit layer with constant surface concentration of reactive groups. After this steady surface structure has been attained, the deposition rate will become a function solely of the gaseous reactant concentrations. In the problem at

hand, however, the deposit layer can only grow to a few layers before pore closure; therefore, the role of the first few layers in determining the final deposit characteristics might be important in the sense that significant pore restriction is caused even by a single layer. On the contrary this would not be the case in a macroporous substrate when hundreds or thousands of layers are deposited before pore closure. Since the first few layers are developed under unsteady conditions, the emphasis of the present work is on the transient kinetics of deposition.

## 3.2 EXPERIMENTAL TECHNIQUES

### 3.2.1 Apparatus

A detailed description of the apparatus for opposing reactants chemical vapor deposition is given elsewhere (Gavalas et al., 1989). A schematic diagram is shown in Figure 3.1. The reactor consists of a porous Vycor tube inside a nonporous quartz tube (12 mm ID). The Vycor tube (7 mm OD, 1.1 mm wall thickness, 0.30 void fraction and 40 Å mean pore diameter) supplied by Corning Inc. is welded from either side with nonporous quartz tube sections to permit connection with metal fittings to the feed gas lines. The chlorides were supplied by Aldrich Chemical Co. with 99.999% purity for  $\text{SiCl}_4$  and 99.99% purity for  $\text{AlCl}_3$ . A chloride reactant stream  $\text{SiCl}_4\text{-N}_2$  or  $\text{AlCl}_3\text{-N}_2$  of the desired composition was generated by passing a stream of nitrogen through a bubbler or sublimator containing  $\text{SiCl}_4$  or  $\text{AlCl}_3$  and held at the appropriate temperature. The water reactant stream was likewise generated by passing  $\text{N}_2$  through a water bubbler. Typical flowrates of  $\text{N}_2$  were 50-100 cc/min for each stream. Typical reactant mol fractions were 0.1-0.35 and were calculated assuming equilibrium at the bubblers. Before deposition the tubes were heated gradually to 600 °C and maintained at that temperature overnight under oxygen flow to remove organic impurities and establish a common concentration of surface hydroxyl groups for all experiments.

### 3.2.2 Scanning Electron Microscopy (SEM)

SEM analysis of tubes carrying the deposited layers was carried out by a CamScan scanning electron microscope operating at 20 KV. The samples (sections of the tubes after deposition) were prepared by first casting in epoxy, and then polishing and coating by carbon or gold to eliminate sample charging. Some tube cross sections were also examined by Electron Microprobe Analysis (EPMA), using a Jeol 733 Superprobe electron microscope with wavelength dispersive spectroscopy detection (WDS). When a focused electron beam was used, we observed sample burning which did not significantly affect the analysis of  $\text{Al}_2\text{O}_3$  or  $\text{TiO}_2$  deposits but was a major problem when analyzing  $\text{SiO}_2$  deposit on Vycor. Thus for most of the  $\text{SiO}_2$  deposit analysis, a 10  $\mu\text{m}$  beam was used to avoid sample burning. That resulted in a lower resolution for the tracing of  $\text{SiO}_2$  layers. Moreover, since in EPMA the analyzed volume increases with decreasing apparent density, the analysis of a  $\text{SiO}_2$  deposit on  $\text{SiO}_2$  substrate will not reveal the actual variations of deposited material because in regions of higher deposition, the analyzed volume will be smaller than from a highly porous region. To account for this limitation, prior to analysis, the substrate and the membrane are impregnated with copper nitrate which is reduced under hydrogen. From the EPMA analysis we find the Si/Cu ratio of the untreated substrate and the membrane. By assuming that to the EPMA resolution Cu concentration is the same over both samples, we can find the deposit over substrate ratio.

## 3.3 EXPERIMENTAL RESULTS

Permeation coefficients (permeances) of hydrogen and nitrogen through  $\text{SiO}_2$  and  $\text{Al}_2\text{O}_3$  membranes are given elsewhere (Tsapatsis et al.,1991). Here we consider only the  $\text{N}_2$  permeance as a measure of pore plugging. Figure 3.2 shows typical results for the evolution of the  $\text{N}_2$  permeance during  $\text{Al}_2\text{O}_3$  and  $\text{SiO}_2$  deposition. The decline of the  $\text{N}_2$

flux, initially slow, accelerates, and then becomes slow once more. The end of the rapid decline period is evidently caused by the elimination of all Knudsen diffusion paths connecting the two sides of the tube wall, i.e., by the loss of connectivity. Once the open Knudsen paths have been eliminated, the reaction rate drops to a very low residual value controlled by activated flux of water through the deposit layer. This residual reaction takes place at the chloride side, for the diffusion coefficient of the larger chloride molecule through the deposit layer is much smaller than that of water. We shall refer to the elimination of continuous Knudsen paths as "pore plugging" and shall define it operationally by the time when the nitrogen flux has declined to one tenth of its initial value. Typical times for pore plugging are 15 minutes for  $\text{Al}_2\text{O}_3$  deposition at  $450^\circ\text{C}$ , 30 minutes for  $\text{Al}_2\text{O}_3$  deposition at  $800^\circ\text{C}$  and 1 hour for  $\text{SiO}_2$  deposition at  $800^\circ\text{C}$ .

Figure 3.3a shows an SEM photograph of an  $\text{Al}_2\text{O}_3$  membrane. The darker region located near the inner radius reveals the presence of aluminum. The white line at the end of that region is believed to be a step created on the sample surface during polishing due to the harder alumina rich region. A typical  $\text{Al}_2\text{O}_3/\text{SiO}_2$  profile obtained by EPMA is shown in Figure 3.3b. The oxide ratio is derived based on the assumption that all Al is present as  $\text{Al}_2\text{O}_3$ . The deposit layer has strongly asymmetric shape and is located near the side of chloride flow, in agreement with previously reported EPMA measurements (Tsapatsis et al., 1991). The deposit layer is spread over several tens of microns, but the completely plugged region is much thinner, probably of order 1 micron, as evidenced by the sharp maximum of the  $\text{Al}_2\text{O}_3/\text{SiO}_2$  ratio located on the white line of the SEM photographs.

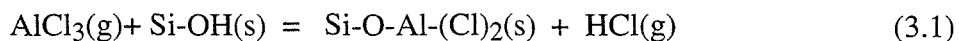
Figure 3.4 shows the radial profile of the  $\text{Al}_2\text{O}_3/\text{SiO}_2$  ratio after 3, 10 and 15 minutes of deposition. The profile, initially monotonically decreasing, at a later time develops a maximum, which sharpens with the progress of deposition. Figure 3.5 shows the ratio of deposited  $\text{SiO}_2$  to substrate  $\text{SiO}_2$  across a tube after pore plugging. The weight of deposited  $\text{SiO}_2$  is derived based on the assumption that all Si deposited is  $\text{SiO}_2$ . We had

previously found that the  $\text{SiO}_2$  density of untreated Vycor tubes varies over the tube cross section. The ratio plotted in Figure 3.5 is based on the measured  $\text{SiO}_2$  density profile of the untreated tube. As in Figure 3.3b, the deposit density is highly asymmetrical about the location of the maximum. However, the overall thickness of that layer is considerably larger than that of Figure 3.3b.

The highest value of the  $\text{Al}_2\text{O}_3$  (deposit)/  $\text{SiO}_2$  (substrate) and  $\text{SiO}_2$  (deposit)/  $\text{SiO}_2$  (substrate) mass ratios measured on the EPMA traces for samples that underwent pore plugging is about 0.17. Complete pore filling (to void fraction zero), on the other hand, corresponds to a ratio of 0.43 for  $\text{SiO}_2$  and 0.58 for  $\text{Al}_2\text{O}_3$  based on true (helium) densities of 2.1 for  $\text{SiO}_2$  (corresponding to reported densities of  $\text{SiO}_2$  films deposited by  $\text{SiH}_4$  oxidation) and 2.85 for  $\text{Al}_2\text{O}_3$  (corresponding to reported densities for  $\gamma\text{-Al}_2\text{O}_3$ ). There are several possible reasons for this discrepancy. A first possibility is that the layers deposited in the opposing reactants geometry have lower densities than the nominal densities used in the calculations. Second, sample polishing would smear and blunt the deposit at the peak, especially if that peak is sharp. Third, the electron beam excites a finite volume in the sample introducing a form of spatial averaging, which would reduce the measured intensity at the narrow plugged region. Moreover, the experimental uncertainty for  $\text{SiO}_2$  analysis is greater than for  $\text{Al}_2\text{O}_3$ , because the calculations for the former require analysis of two different Vycor samples, while for the latter the EPMA scan of a single sample provides directly the deposit to substrate ratio. As significant as these uncertainties are, it is unlikely that they are sufficient to fully account for the difference between the measured deposit density and the density corresponding to complete pore filling. A major part of this difference must be attributed to interruption of connectivity at a nonzero void fraction, as expected from percolation theory.

To explore the role of the initial chemical structure of the substrate surface on the course of deposition, we performed the following additional experiment. The porous

Vycor support was first exposed to a dry stream of  $\text{AlCl}_3\text{-N}_2$  which reacts to replace surface OH groups with Cl groups as follows:

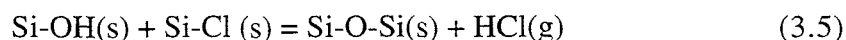
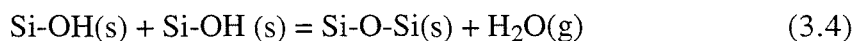
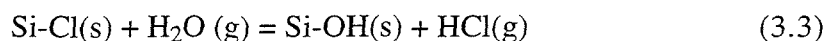
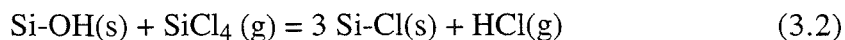


The dehydroxylated or partially dehydroxylated support was then subjected to the usual opposing reactant deposition of  $\text{Al}_2\text{O}_3$ . EPMA analysis of the resulting deposit layer produced the results shown in Figure 3.6. The peak has shifted towards the water side and the steep decline is facing the chloride side, in contrast with the peak shapes observed in Figures 3.3 through 3.5. This drastic change of the deposit profile reveals the importance of the substrate surface chemistry.

### 3.4 MODEL FORMULATION

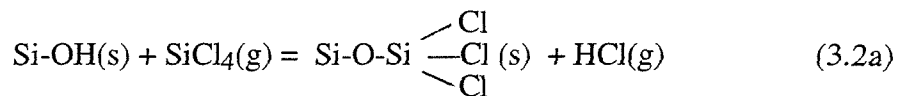
#### 3.4.1 Reaction Mechanism for $\text{SiO}_2$ Formation

The role of homogeneous and heterogeneous reactions in one-sided and opposing reactants deposition has been discussed in a previous report (Tsapatsis et al., 1991). Previous kinetic experiments suggest that the homogeneous reaction between  $\text{SiCl}_4$  and water is slow and that  $\text{SiO}_2$  deposition on high surface area silica takes place by an heterogeneous mechanism which can be described by the following simplified scheme (Hair and Hertl, 1969,1973; Armistead and Hockey, 1967) :

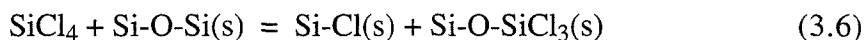


where  $\text{Si-OH}(\text{s})$  represents a surface hydroxyl group (silanol),  $\text{Si-Cl}(\text{s})$  a surface chloride group, and  $\text{Si-O-Si}(\text{s})$  a siloxane bridge on the solid. In this notation we are counting

surface -OH and -Cl groups and not silicon atoms. Equation 3.2 could be written more analytically as



In limiting the reaction network to the above four steps, we have neglected the attack by  $\text{SiCl}_4$  on siloxane bonds leading to the direct chlorination



which has been previously reported but not quantified (Morrow and Code, 1976; Bunker et al., 1989). We have also not distinguished among different types of surface -OH groups (isolated, geminal, hydrogen bonded) which are known to have different reactivities towards  $\text{SiCl}_4$  and other chlorides. According to Equation (3.2) the chloride initially reacts with the Vycor surface even in the absence of water (until all OH groups are consumed). That reaction affects the chloride concentration profile and consequently the overall deposition process.

### 3.4.2 Reaction Mechanism for $\text{Al}_2\text{O}_3$ Formation

The reports of Peri (1966) and Peri and Hensley (1968) on reactions of  $\text{AlCl}_3$  with surface -OH groups suggest that a reaction analogous to Equation 3.2 takes place between gaseous  $\text{AlCl}_3$  and silica. However, IR examination of a silica sample treated by  $\text{AlCl}_3$  and subsequently exposed to  $\text{H}_2\text{O}$  disclosed Si-OH rather than Al-OH groups (Peri, 1966; Peglar et al., 1971). The absence of Al-OH may be due to rapid condensation or the transfer of these groups to silicon atoms. In view of the uncertainty about the precise reactions of  $\text{AlCl}_3$  with silica, we have not developed specific rate expressions for the formation of  $\text{Al}_2\text{O}_3$ . Moreover, the homogeneous reaction between  $\text{AlCl}_3$  and  $\text{H}_2\text{O}$  may play some role despite the large surface area and the low concentration of reactants in the

deposition region (Wong and Robinson, 1970). Because of this lack of specific kinetic information, we have not implemented the model for alumina deposition. We note, however, that the density profiles of the  $\text{Al}_2\text{O}_3$  layer as well as those from  $\text{TiO}_2$  deposition reported elsewhere (Tsapatsis et al., 1991) have some common features with those of  $\text{SiO}_2$ , especially the slow increase followed by the steep decline in the direction from the chloride side to the water side suggesting similarities in the deposition mechanisms.

### 3.4.3 *Formulation of Kinetics and Species Balances*

The silanol and chloride groups initially can be considered as surface species. As the deposit builds up, however, these groups become distributed throughout the volume of the deposit layer. Because of this unusual feature, the concentration of silanol and chloride groups will be given in mols per unit volume.

The species balances will be formulated treating reactions 3.2 through 3.5 as elementary and using the rate expressions

$$r_1 = k_1 C_1 S_{\text{OH}} \quad (3.7)$$

$$r_2 = k_2 C_2 S_{\text{Cl}} \quad (3.8)$$

$$r_3 = k_3 S_{\text{OH}}^2 \quad (3.9)$$

$$r_4 = k_4 S_{\text{OH}} S_{\text{Cl}} \quad (3.10)$$

where  $S_{\text{OH}}$  and  $S_{\text{Cl}}$  are the concentrations of the -OH and -Cl groups in mols per unit total volume and the  $r_i$  are expressed in mols per unit total volume per unit time. As suggested in the literature (Hair and Hertl, 1969, 1973; Armistead and Hockey, 1967), the reactions are considered irreversible with HCl being unable to attack the silica deposit (Iller, 1979). It is implicitly assumed that all -OH and -Cl groups within the deposit layer are equally accessible to the gaseous molecules, a reasonable assumption in view of the few monolayer thickness of the deposit layer. Unlike reactions 3.2 and 3.3, reactions 3.4 and 3.5 are assumed to be second order in the condensed species -OH and -Cl. It should be noted here

that we consider condensation reactions taking place in the whole volume of the deposit. This is in accordance with the assumption that all OH and Cl species are accessible to gaseous reactants. In other words the condensation reactions are considered as solid state reactions with rates expressed per unit volume of the deposit layer per unit time. If  $\phi = \epsilon_0 - \epsilon$  is the volume fraction of the deposit layer with respect to the total volume, then the rate of reaction 3.4 in mols per unit volume of the deposit layer per unit time is given by

$$\frac{r_3}{\phi} = k_3 \left( \frac{S_{OH}}{\phi} \right)^2 \quad (3.11)$$

and similarly for reaction 3.5, with  $k_3$  and  $k_4$  being intrinsic rate constants. Thus the rate parameters  $k_3'$  and  $k_4'$  in Equations 3.9 and 3.10 are functions of the extent of deposition,

$$k_3' = \frac{k_3}{\epsilon_0 - \epsilon}, \quad k_4' = \frac{k_4}{\epsilon_0 - \epsilon} \quad (3.12)$$

Equations (3.9), (3.10) and (3.12) hold only after the deposit layer has attained a small but finite thickness ( $\epsilon_0 - \epsilon > 0$ ). Initially there are no chloride groups, and the silanol groups have stabilized to some fixed concentration by virtue of the thermal pretreatment. The section Numerical Results and Discussion describes the initialization of the integration.

The use of two concentrations  $S_{OH}$  and  $S_{Cl}$  to characterize the deposit layer is a drastic approximation, for it ignores the role of the geometric arrangement (proximity, etc.) of these immobile species. Such effects cannot be represented by classical kinetics and will not be considered here.

We have chosen to represent diffusion and pore constriction by a classical model, ignoring the statistical or percolative aspects of pore connectivity. The EPMA results shown in the previous section indicate that connectivity is, in fact, interrupted at some nonzero void fraction. However, the quantification of connectivity and the percolation threshold does not appear practical without additional experimentation, specifically addressed to these issues, or without additional empiricism and mathematical complication.

The conventional reaction-diffusion problem is now formulated using the rate expressions (3.7)-(3.12) and neglecting the curvature of the tube wall to obtain the following balances for the gas phase and condensed phase species.

$$\frac{\partial}{\partial x} \left[ D_1(\varepsilon) \frac{\partial C_1}{\partial x} \right] = k_1 C_1 S_{OH} \quad (3.13)$$

$$\frac{\partial}{\partial x} \left[ D_2(\varepsilon) \frac{\partial C_2}{\partial x} \right] = k_2 C_2 S_{Cl} - \frac{k_3}{\varepsilon_0 - \varepsilon} S_{OH}^2 \quad (3.14)$$

$$\frac{\partial S_{OH}}{\partial t} = -k_1 C_1 S_{OH} + k_2 C_2 S_{Cl} - \frac{1}{\varepsilon_0 - \varepsilon} (2k_3 S_{OH}^2 + k_4 S_{OH} S_{Cl}) \quad (3.15)$$

$$\frac{\partial S_{Cl}}{\partial t} = 3k_1 C_1 S_{OH} - k_2 C_2 S_{Cl} - \frac{k_4}{\varepsilon_0 - \varepsilon} S_{OH} S_{Cl} \quad (3.16)$$

$$\frac{\partial S_0}{\partial t} = \frac{1}{\varepsilon_0 - \varepsilon} (k_3 S_{OH}^2 + k_4 S_{OH} S_{Cl}) \quad (3.17)$$

where  $S_0$  is the concentration of siloxane bonds (Si-O-Si) in the deposit layer in mols per unit total volume. Equations 3.13 and 3.14 neglect the gas phase accumulation term, an approximation justified by comparison of the observed times for pore plugging, which were on the order of 30 minutes, with the characteristic time for gaseous diffusion, which was estimated to be on the order of a few seconds.

The progress of deposition can be characterized by the instantaneous void fraction  $\varepsilon$  computed from the amount of silicon in the deposit layer using some value for the molar volume per silicon atom. For this purpose we shall ignore the differences among the molar volumes of silicon atoms associated with different groups and use the volume  $v$  corresponding to undensified  $\text{SiO}_2$  produced by chemical vapor deposition, so that

$$\frac{\partial \varepsilon}{\partial t} = -v k_1 C_1 S_{OH} \quad (3.18)$$

The initial and boundary conditions associated with Equations 3.13 through 3.18 are:

$$t = 0 : S_{OH} = S_{OH}^0, S_{Cl} = 0, \varepsilon = \varepsilon_0 \quad (3.19)$$

$$x = 0 : l_1 (C_{10} - C_1) = -D_1 \frac{\partial c_1}{\partial x} \quad (3.20)$$

$$l_2 C_2 = D_2 \frac{\partial c_2}{\partial x} \quad (3.21)$$

$$x = L : l_2' (C_{20} - C_2) = D_2 \frac{\partial C_2}{\partial x} \quad (3.22)$$

$$l_1' C_1 = -D_1 \frac{\partial C_1}{\partial x} \quad (3.23)$$

where the bulk values of  $C_2$  and  $C_1$  at the chloride side and the water side, respectively, are zero,  $l_1$  and  $l_2$  are the mass transfer coefficients from the chloride side (tube interior), and  $l_1'$  and  $l_2'$  are the same coefficients at the water side (annulus).

The effective diffusion coefficients in Equations 3.13 and 3.14 (and in Equations 3.20 through 3.23) are functions of the local porous structure. For simplicity we have adopted the random capillary model (Gavalas, 1980) with capillaries of uniform initial radius  $a_0$ . Then, the local capillary radius is related to the local void fraction by the relation

$$\varepsilon(x,t) = 1 - \exp(-2\pi\lambda a^2) \quad (3.24)$$

The two effective diffusion coefficients are then expressed in terms of  $\varepsilon$  by the simple often used relation

$$D_i = \frac{\varepsilon}{\tau} A \left( \frac{T}{M_i} \right)^{1/2} a \quad i = 1,2 \quad (3.25)$$

where  $A$  is the constant in the Knudsen diffusion coefficient,  $M_1$  and  $M_2$  are the molecular weights of chloride and water, and  $\tau$  is the empirical tortuosity.

### 3.5 NUMERICAL RESULTS AND DISCUSSION

Simulations were performed for  $\text{SiO}_2$  formation at  $800\text{ }^\circ\text{C}$ . Among the various rate constants only  $k_1$  could be estimated from previous reports. Hair and Hertl (1969) reported values of  $k_1$  in the range  $300\text{-}500\text{ }^\circ\text{C}$ . Recent thermogravimetric experiments in our laboratory provided additional values up to  $600\text{ }^\circ\text{C}$ . Extrapolating these measurements to  $800\text{ }^\circ\text{C}$  we estimated the base value of  $k_1$  listed in Table 3.1. The thermogravimetric experiments also indicated that  $k_2$  is lower than  $k_1$  by a factor of 3 to 10. In our calculations we varied  $k_2/k_1$  between 0.1 and 1. The constants  $k_3$  and  $k_4$  for which no information was available were varied together between 0 and 10. The initial surface concentration of silanol groups ( $-\text{OH}$ ) was estimated from the aforementioned thermogravimetric experiments to be between 3 and  $5/(\text{nm})^2$  for Vycor annealed at  $600\text{ }^\circ\text{C}$ , while for Vycor annealed at  $800\text{ }^\circ\text{C}$ , the literature suggests a lower value,  $1\text{-}2/(\text{nm})^2$  (Hair and Hertl, 1969, 1973; Peri and Hensley, 1968). In our experiments the Vycor tubes were pretreated at  $600\text{ }^\circ\text{C}$  for several hours and then heated to  $800\text{ }^\circ\text{C}$  just before the beginning of deposition. Because the exposure to  $800\text{ }^\circ\text{C}$  before deposition was minimal, we estimated the concentration of the  $-\text{OH}$  groups to be in the range  $1.5\text{-}4.5/(\text{nm})^2$  and made parametric calculations with several values in this range. The Nusselt number was estimated around 4 for both the internal and external flows (Welty et al., 1984) while the bulk diffusion coefficients were estimated using the equation given in Bird et al., (1960), p. 505. Table 3.1 lists all the other parameter values used in the calculations. Numerical solutions of Equations 3.13 through 3.23 were obtained to explore the effect of various parameters and compare with the microprobe traces. The time evolution Equations 3.15 through 3.18 were integrated by a fourth order Runge-Kutta routine. Each evaluation of the right side of these equations required solution of the linear boundary value problem 3.13-3.14, 3.20-3.23. This solution was carried out by difference spatial discretization

and solution of the resulting linear system by Gaussian elimination. Each run was terminated when the local radius decreased to one-tenth of its original value (4 Å).

At  $t = 0$  the rate of condensation reactions is zero because there are no chloride groups, and because the -OH groups after lengthy heat pretreatment are too far from each other or prevented to react because of steric hinderances (this subtlety is not described by Equation (3.9)). Thus, at  $t = 0$  the last terms in Equations (3.14) and (3.15) are indeterminate. To initialize the integration we have set these two terms equal to zero until  $\varepsilon_0 - \varepsilon$  becomes 0.01.

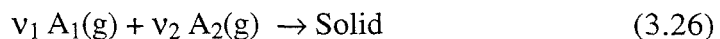
Figure 3.7 shows the density profile of the deposit layer at different times during deposition. The profile initially decreases monotonically with distance from the chloride side, but later develops a maximum which gradually steepens as pore plugging is approached. As mentioned earlier in the discussion of Figure 3.5, the value of 0.17 for  $\text{SiO}_2(\text{deposit})/\text{SiO}_2(\text{substrate})$  at the position of pore plugging measured in the electron probe scans contains several errors, the most important of which is the limited resolution of the electron microprobe. Thus, the true value of this ratio is expected to be higher than 0.17 but lower than the value 0.43 calculated for complete pore filling, assuming a deposit density of  $2.1 \text{ g/cm}^3$ . Taking as an estimate a value  $\sim 0.2$ , we may consider pore plugging to occur at  $t \approx 60$  minutes when the peak of the profile reaches that value. For comparison the experimental points of Figure 3.5 have been included in Figure 3.7.

Figures 3.8-3.11 illustrate the effect of the parameters  $k_2/k_1$ ,  $k_3$ ,  $S_{\text{OH}}^0$ , and  $C_{10}$ . Figure 3.8 shows the normalized density profile of the deposit layer vs. dimensionless distance from the chloride side for different values of the ratio  $k_2/k_1$ . Keeping  $k_1$  constant, the film thickness and the time required for pore plugging increase with decreasing values of  $k_2/k_1$ . Clearly, with lower hydrolysis rates, the regeneration of the -OH groups necessary for continuation of the reaction becomes slower, slowing down the overall process. Figure 3.9 shows the effect of the condensation reaction (3) and (4). As  $k_3$  and

$k_4$  increase the film moves away from the chloride side and the time for complete pore filling increases from 69 min for  $k_3 = 0$  to 74 min for  $k_1 = 20 \text{ cm}^3/\text{min}\cdot\text{mol}$ . As expected, more rapid condensation reactions bring down the concentration of reactive sites and slow down the overall process. Moreover, the condensation reactions have a larger stoichiometric coefficient for -OH groups and therefore tend to decrease the [-OH]:[-Cl] ratio moving the reaction region towards the water side. By contrast, an increase of  $S_{\text{OH}}^0$  causes the deposit layer to move towards the chloride side and the tail thickness to increase (Figure 3.10). As OH concentration increases, more chloride can react with the Vycor surface in the absence of  $\text{H}_2\text{O}$  vapor causing the increase of the tail thickness. Moreover, due to the increased chloride consumption, the reaction front is moved towards the chloride side causing the shift of the deposit position. Finally, increasing the concentration of one of the reactants (e.g., the chloride) causes the deposit layer to move in the direction of the other reactant and shortens the time required for pore plugging (Figure 3.11). Additional calculations not included in the figures show that the width of the deposit layer decreases while the time for pore filling increases with decreasing initial pore size. For example the times to complete pore filling were 69 and 95 minutes for initial pore diameters of 40 Å and 25 Å respectively.

Despite the success of the transient model in describing the growth of the deposit, it is interesting to examine the ability of a conventional pseudosteady kinetics to describe deposition. For this purpose we have formulated a deposition model based on pseudosteady kinetics and carried out a number of calculations to obtain deposit layer profiles up to the time of pore plugging. The development of this model is presented below:

Consider the chemical vapor deposition reaction:



occurring within the walls of porous glass in an opposing reactants geometry.

Diffusion and reaction in a porous glass can be described by the equations:

$$\frac{\partial}{\partial x} \left( D_1(\epsilon) \frac{\partial c_1}{\partial x} \right) = v_1 S(\epsilon) r \quad (3.27)$$

$$\frac{\partial}{\partial x} \left( D_2(\epsilon) \frac{\partial c_2}{\partial x} \right) = v_2 S(\epsilon) r \quad (3.28)$$

with boundary conditions:

$$\text{at } x = 0 \quad l_1 (C_{10} - C_1) = -D_1 \frac{\partial C_1}{\partial x}, \quad l_2 C_2 = D_2 \frac{\partial C_2}{\partial x} \quad (3.29)$$

$$\text{at } x = L \quad l_2 (C_{20} - C_2) = D_2 \frac{\partial C_2}{\partial x}, \quad l_1 C_1 = -D_1 \frac{\partial C_1}{\partial x} \quad (3.30)$$

where we used the pseudosteady state approximation to delete the accumulation terms. The rate of increase of the deposit solid layer is:

$$\frac{\partial q}{\partial t} = v r \quad (3.31)$$

$$\text{with initial condition} \quad \text{at } t = 0 \quad q = 0 \quad (3.32)$$

We use the following rate expression

$$r = k C_1^\alpha C_2^\beta \quad (3.33)$$

The random pore model with single initial radius  $a_0$  is used and additionally here we make use of the relation:

$$S(q) = -\frac{d\epsilon(q)}{dq} = 4 \pi (1 - \epsilon) [\lambda(a_0 - q)] \quad (3.34)$$

since in that model one needs the surface area.

The above equations are solved numerically using central finite difference. The equations are discretized to give a set of nonlinear algebraic equations which are solved by iteration based on the Newton-Raphson method.

Numerous runs were performed combining various values of  $\alpha$  and  $\beta$  with a value of  $k$  such that pore closure takes place at approximately 60 ~ 90 min. None of these simulations was able to reproduce the experimental deposit characteristics. Figure 3.12 is an example from these simulations for the conditions of the experiment shown in Figure 3.5. This figure shows the deposit profiles for various values of  $\alpha$  and  $\beta$  and a common value of  $k$  chosen to match the experimental time for pore closure. The profiles calculated from the model fail to match the finite deposit density at  $x = 0$ . The position of the peak could be made to match the experimental position by increasing  $\alpha/\beta$  but then the profile does not have the steep decline after the peak. On the other hand, by decreasing  $\alpha/\beta$  it is possible to match the steep drop of the profile but then the peak location moves too far to the right.

A final word of caution is in order about the scope of the deposition model. The model developed here is confined to the description of the growth of the deposit layer and can predict the gross features of the final deposit density profile. This information is of some value in understanding qualitatively the effect of parameters such as pore size, concentration of reactants, etc., on the membrane permeance. However, the quantitative prediction of membrane permeance requires measurement of the permeability of various gases as a function of deposit density over the whole range of densities encountered across the membrane layer. This experimental programme has not been carried out.

### 3.6 CONCLUSIONS

Silica and alumina layers prepared in the opposing reactants geometry by the hydrolysis of the chlorides possess highly asymmetric shape. The deposit density

increases gradually from the chloride side, passes through a maximum and steeply decreases to zero well before the water side. Pore plugging is attained at a nonzero void fraction, evidently due to a percolative interruption of connectivity. A deposition mechanism suggested by previous studies has been adopted involving reaction of the gaseous chloride with silanol groups on the surface, reaction of water vapor with chloride groups of the surface, and condensation of two silanol groups or a silanol and a chloride group to form siloxane bonds. The transient kinetics associated with these reactions were introduced into a model employing a classical description of diffusion and pore closure. The numerical results obtained with this model describe well the location and shape of the deposit layer but are not capable of describing the interruption of connectivity at a nonzero void fraction. The calculations show that the geometry of the deposit layer is relatively insensitive to the kinetic parameters, but it is more sensitive to the pore size and the density of silanol groups of the Vycor substrate. A pseudosteady kinetic model failed to predict the qualitative trends observed in the experiments.

## **ACKNOWLEDGMENTS**

Dr. S. W. Nam contributed in the development of the homogeneous model. Support was provided by the Department of Energy with UCR Grant DE-FG22-89PC89765 and Contract DE-AC21-90MC26365.

**LITERATURE CITED**

Armistead, C. G. and Hockey, J. A. Reactions of Chloromethylsilanes with Hydrated Aerosil Silicas. *Trans. Faraday Soc.* **1967**, *63*, 2549-2556.

Bird, R. B., Stewart, W. E. and Lightfoot E. N. Transport Phenomena, Wiley, New York, 1960.

Bunker, B. C., Haaland, D. M., Michalske, T. A. and Smith, W. L. Kinetics of Dissociative Chemisorption on Strained Edge-Shared Surface Defects on Dehydroxylated Silica. *Surf. Sci.* **1989**, *222*, 95.

Carolan, M. and Michaels, J. N. Chemical Vapor Deposition of Yttria Stabilized Zirconia on Porous Substrates. *Solid State Ionics* **1987**, *25*, 207.

Gavalas, G. R. A Random Capillary Model With Application to Char Gasification at Chemically Controlled Rates. *AIChE J.* **1980**, *26*, 577.

Gavalas, G. R., Megiris, C. E. and Nam, S. W. Deposition of H<sub>2</sub>-permselective SiO<sub>2</sub> Films. *Chem. Eng. Sci.* **1989**, *44*, 1829.

Hair, M. L., and Hertl, W. Reactions of Chlorosilanes with Silica Surfaces. *J. Phys. Chem.* **1969**, *73*, 2372.

Hair, M. L. and Hertl, W. Chlorination of Silica Surfaces. *J. Phys. Chem.* **1973**, *77*, 2070.

Iller, R. K. *The Chemistry of Silica*, John Wiley & Sons, New York, 1979.

Isenberg, A. O. Energy Conversion via Solid Electrolyte Electrochemical Cells at High Temperatures. *Solid State Ionics* **1981**, 314, 431.

Morrow, B. A. and Cody, I. A. Infrared Studies of Reactions on Oxide Surfaces. 5. Lewis Acid Sites on Dehydroxylated Silica. *J. Phys. Chem.* **1976**, 80, 1995.

Peglar, R. J., Hambleton, F. H. and Hockey, J. A., Structure Surface and Catalytic Properties of the  $\text{SiO}_2/\text{BCl}_3$ ,  $\text{SiO}_2/\text{AlMe}_3$  and  $\text{SiO}_2/\text{AlCl}_3$  Systems. *J. Catal.* **1971**, 20, 309.

Peri, J. B. Infrared Study of Adsorption of Carbon Dioxide, hydrogen Chloride and other Molecules on "Acid" Sites on Dry Silica-Alumina and  $\gamma$ -Alumina. *J. Phys. Chem.* **1966**, 70, 3168.

Peri, J. B. and Hensley, A.L., Jr. The Surface Structure of Silica Gel. *J. Phys. Chem.* **1968**, 72, 2926.

Sahimi, M., Gavalas, G. R. and Tsotsis, T.T. Statistical and Continuum Models of Fluid-Solid Reactions in Porous Media. *Chem. Eng. Sci.* **1990**, 45, 1443.

Sotirchos, S. V. Dynamic Modelling of Chemical Vapor Infiltration. *AIChE J.* **1991**, 37, 1369.

Tsapatsis, M., Kim, S. J., Nam, S. W. and Gavalas, G. R. Synthesis of Hydrogen Permselective  $\text{SiO}_2$ ,  $\text{TiO}_2$ ,  $\text{Al}_2\text{O}_3$  and  $\text{B}_2\text{O}_3$  Membranes from the Chloride Precursors. *I&EC Res.* **1991**, *30*, 2152.

Welty, J. R., Wicks, C. E. and Wilson, R. E. Fundamentals of Momentum, Heat and Mass Transfer, John Wiley & Sons, New York , 1984.

Wong, P. and Robinson, M. Chemical Vapor Deposition of Polycrystalline  $\text{Al}_2\text{O}_3$ . *J. Amer. Ceram. Soc.* **1970**, *53*, 617.

**Notation**

a:	pore radius, cm
$a_0$ :	initial pore radius, cm
$C_1$ :	gas phase chloride concentration, mol/cm <sup>3</sup> pore volume
$C_2$ :	gas phase water concentration, mol/cm <sup>3</sup> pore volume
$C_1^0$ :	chloride or water concentration at the bubbler, mol/cm <sup>3</sup>
d:	outside diameter of Vycor tube, cm
$d'_{\text{equivalent}}$ :	equivalent hydraulic diameter of outside flow, cm
$D_i$ :	Knudsen diffusivity of species i, cm <sup>2</sup> /min
$D_{i,\text{bulk}}$ :	binary diffusivity of species i, cm <sup>2</sup> /min
k:	reaction rate constant used in the pseudosteady state kinetics
$k_1, k_2$ :	reaction rate constants, cm <sup>3</sup> pore volume/min-mol
$k_3, k_4$ :	reaction rate constants, cm <sup>3</sup> deposit/min-mol
L:	thickness of substrate Vycor tube, cm
$M_i$ :	molecular weight of species i
Nu:	Nusselt number
q:	thickness of deposit layer perpendicular to pore wall, cm
R:	gas constant
r:	reaction rate used in the pseudosteady state kinetics, mol/cm <sup>2</sup> -min
$r_i$ :	rate of i <sup>th</sup> reaction (i = 1, ..., 4); mol/cm <sup>3</sup> -min
$S_{\text{OH}}$ :	-OH concentration, mol/cm <sup>3</sup>
$S_{\text{Cl}}$ :	-Cl concentration, mol/cm <sup>3</sup>
$S_{\text{O}}$ :	Si <sup>O</sup> Si concentration, mol/cm <sup>3</sup>
$S_{\text{OH}}^0, S_{\text{Cl}}^0$ :	initial concentrations of OH and Cl, mol/cm <sup>3</sup>
S:	surface area per unit volume, cm <sup>2</sup> /cm <sup>3</sup>

- T: temperature, K  
v: molar volume of deposit, cm<sup>3</sup>/mole  
x: distance measured from inside wall of substrate tube, cm

**Greek letters**

- $\alpha$ : reaction order of chloride (when using the expression  $r = k C_1^\alpha C_2^\beta$ )  
 $\beta$ : reaction order of water (when using the expression  $r = k C_1^\alpha C_2^\beta$ )  
 $\epsilon_0$ : initial void fraction of substrate  
 $\epsilon$ : void fraction of substrate  
 $\lambda$ : parameter of the random capillary model, cm<sup>-2</sup>  
 $\tau$ : tortuosity  
 $\phi$ : deposit volume fraction

**Table 3.1.** Model Parameter Values.

$k_1$	=	$2.45 \times 10^{11} \exp(-22000/RT) \text{ cm}^3/\text{min-mol}$
$k_4$	=	$5 \text{ cm}^3 \text{ solid deposit}/\text{min-mol}$
$k_2$	=	$0.1 k_1$
$k_3$	=	$k_4$
$C_1^0$	=	$0.25 \text{ atm}/RT$
$C_2^0$	=	$0.1 \text{ atm}/RT$
$\tau$	=	3
$\epsilon_o$	=	0.3
$a_o$	=	$20 \times 10^{-8} \text{ cm}$
$L$	=	0.11 cm
$S_o$	=	$3 \times 10^6 \text{ cm}^2/\text{cm}^3$
$v$	=	$29 \text{ cm}^3/\text{g mole}$
$\rho_p$	=	$1.47 \text{ g}/\text{cm}^3$
$S_{OH}^o$	=	$(\text{OH sites}/\text{nm}^2) \frac{1}{6.023 \times 10^{23}} S_o \text{ in moles}/\text{cm}^3$
OH/nm <sup>2</sup>	=	2
$l_i$	=	$\frac{Nu' D_{i,bulk}}{d}$ , cm / min
$l_i'$	=	$\frac{Nu' D_{i,bulk}}{d'}$ , cm / min
$Nu \cong Nu'$	=	4
$d \sim d'_{\text{equivalent}}$	=	0.5 cm
$D_{H_2O,bulk}$	=	$5.2 \text{ cm}^2/\text{s}$ , at $800^\circ\text{C}$ (estimated using Eq. 16.3-1 from Bird et al. (1960), p. 505)
$D_{SiCl_4,bulk}$	=	$2 \text{ cm}^2/\text{s}$ , at $800^\circ\text{C}$ (estimated using Eq. 16.3-1 from Bird et al. (1960), p. 505)

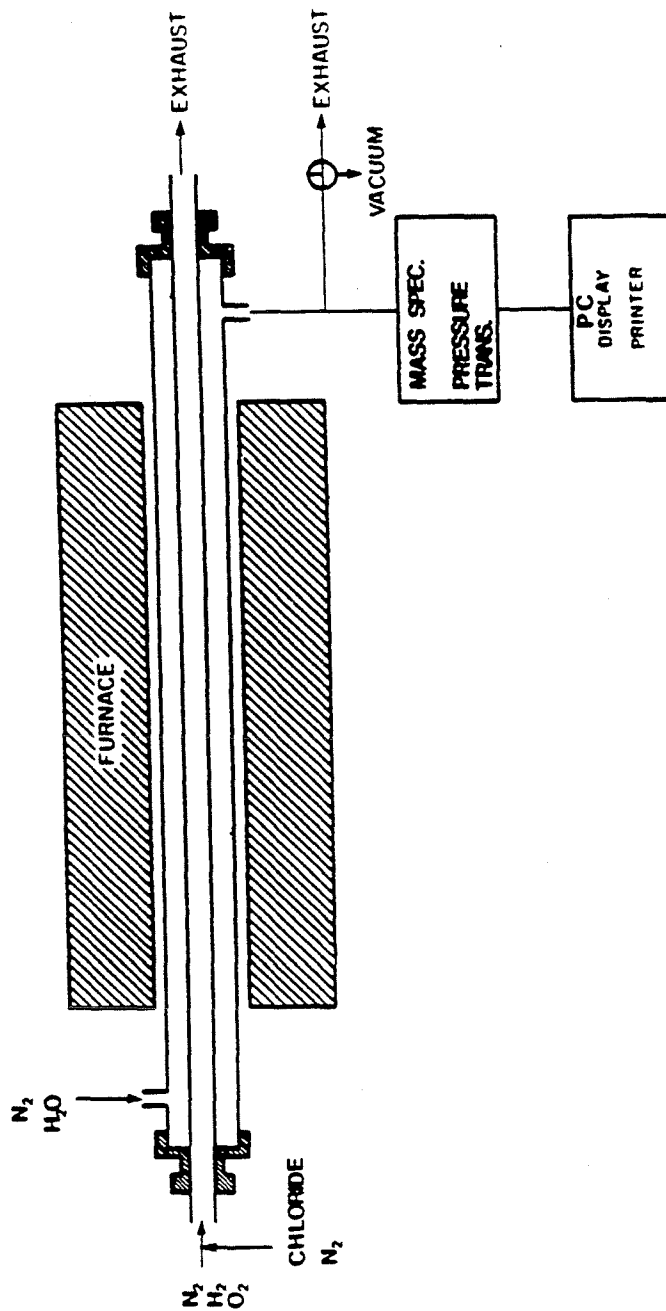


Figure 3.1 Schematic of deposition system.

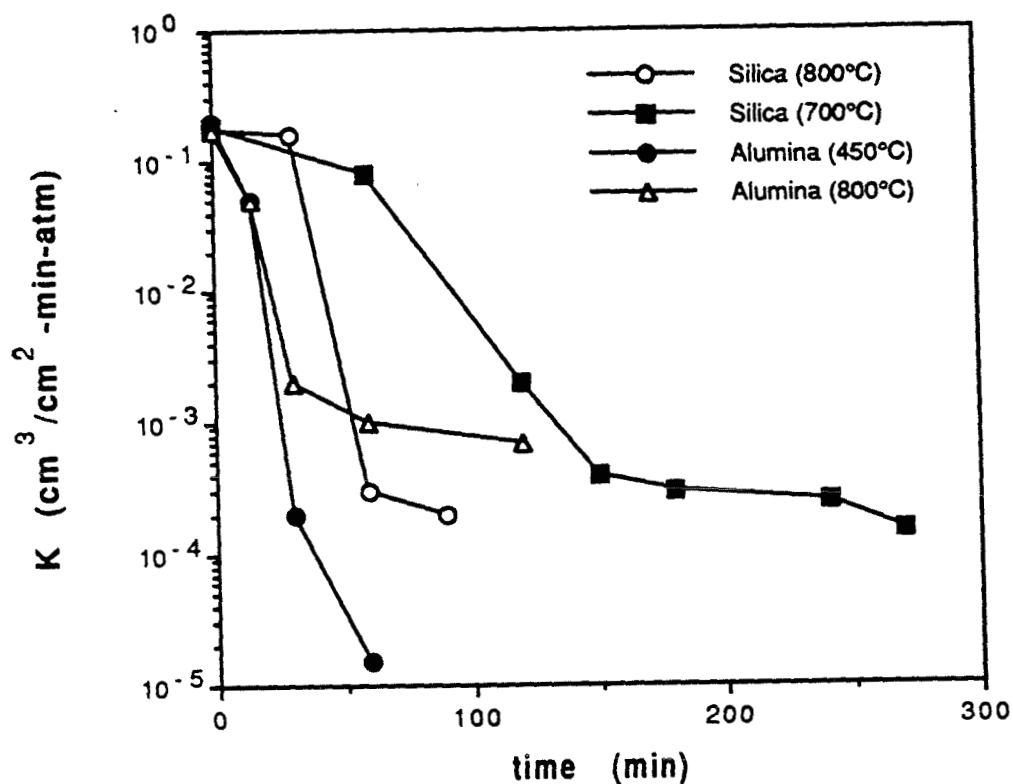


Figure 3.2 Evolution of  $\text{N}_2$  permeance (measured at deposition temperature) for : Alumina deposition at  $450^\circ\text{C}$  (●) and  $800^\circ\text{C}$  ( $\Delta$ ), using 8%  $\text{H}_2\text{O-N}_2$  and 20%  $\text{AlCl}_3\text{-N}_2$  in opposing reactants geometry. Silica deposition at  $800^\circ\text{C}$  (O) and  $700^\circ\text{C}$  (■), using 7%  $\text{H}_2\text{O-N}_2$  and 30%  $\text{SiCl}_4\text{-N}_2$  in opposing reactants geometry.

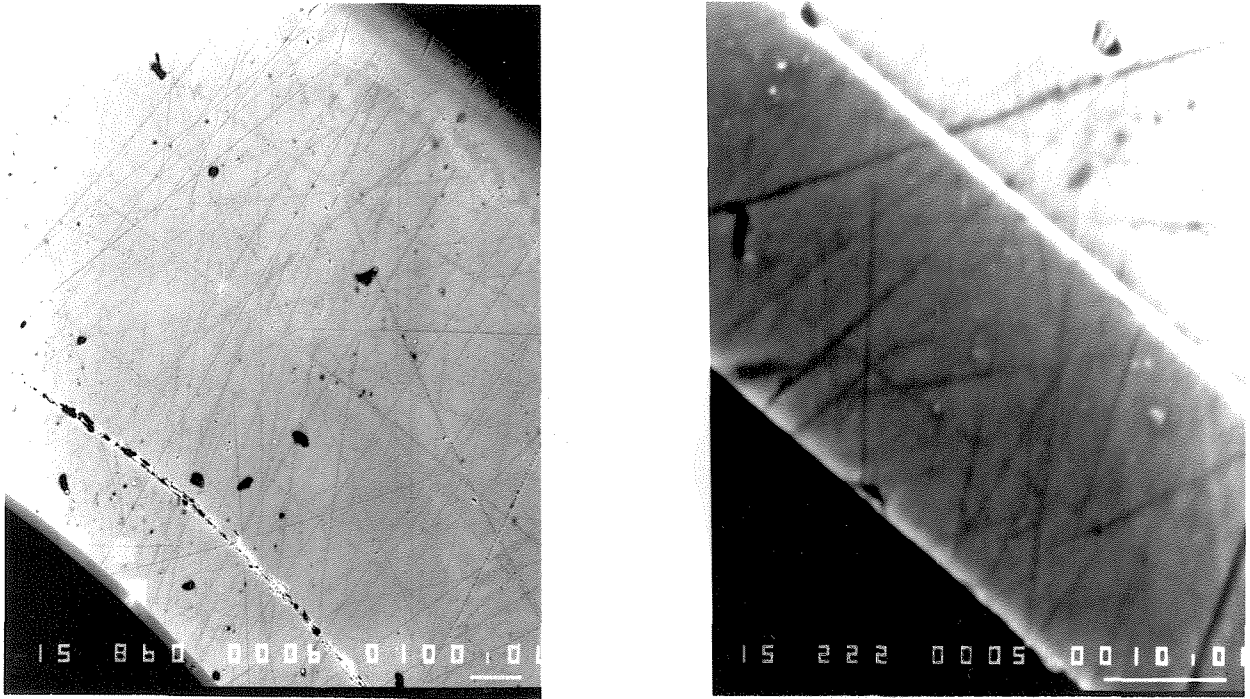


Figure 3.3a SEM micrograph of an Al<sub>2</sub>O<sub>3</sub> membrane at two different magnifications (bars are 100 μm at left and 10 μm at right). Membrane prepared at 450 °C by opposing reactants deposition with 20% AlCl<sub>3</sub>-N<sub>2</sub> and 7% H<sub>2</sub>O-N<sub>2</sub>.

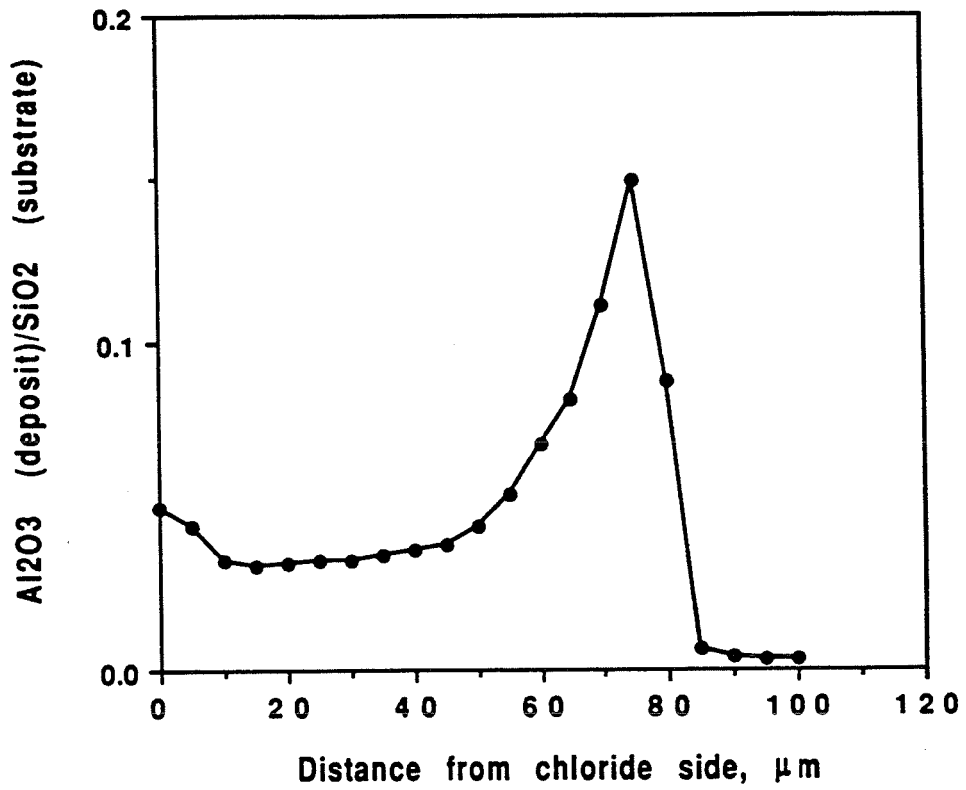


Figure 3.3b Mass ratio of Al<sub>2</sub>O<sub>3</sub> (deposit) to SiO<sub>2</sub> (substrate) obtained by electron microprobe analysis of a membrane prepared at 800°C by opposing reactants deposition with 20% AlCl<sub>3</sub>-N<sub>2</sub> and 7% H<sub>2</sub>O-N<sub>2</sub>.

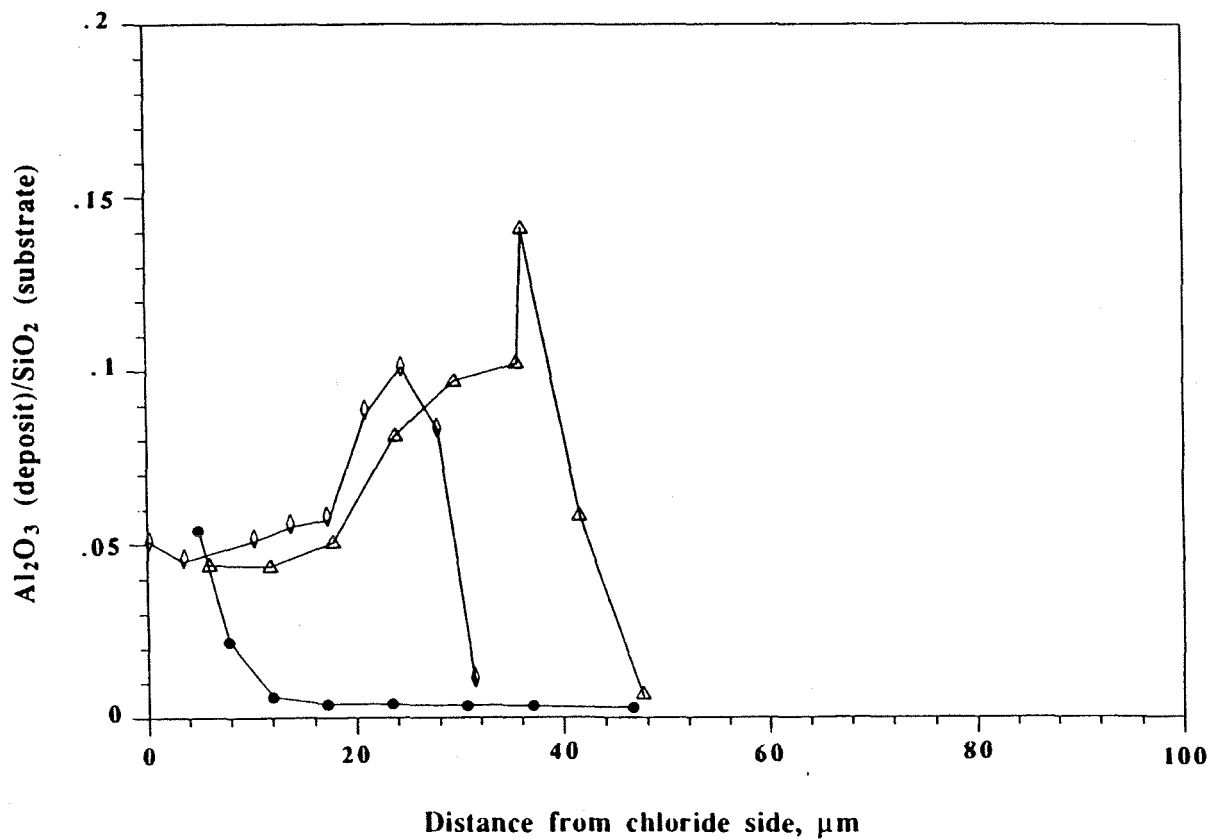


Figure 3.4 Electron microprobe analysis of Vycor cross-sections subjected to Al<sub>2</sub>O<sub>3</sub> deposition in the opposing reactants geometry at 450 °C with 20% AlCl<sub>3</sub>-N<sub>2</sub> and 7% H<sub>2</sub>O-N<sub>2</sub> for 3 min (O), 10 min ( $\diamond$ ) and 15 min ( $\Delta$ ).

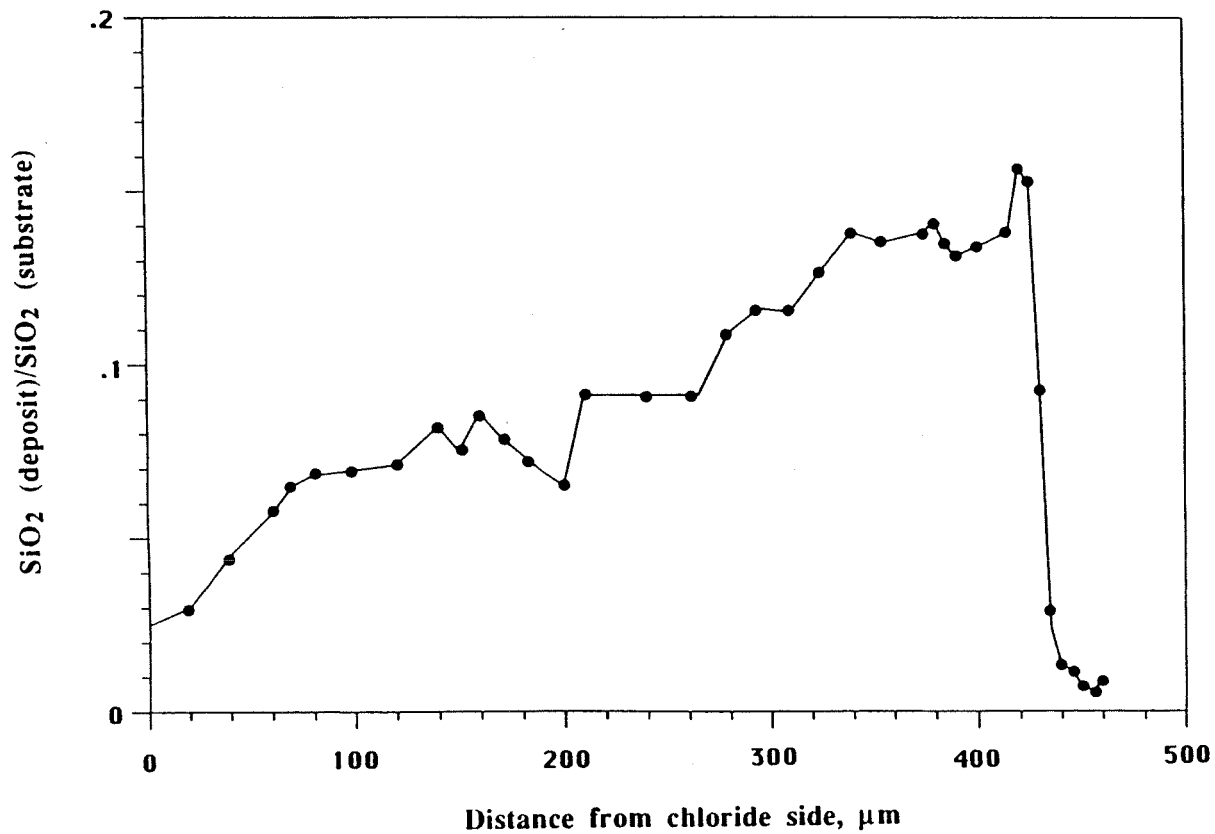


Figure 3.5 Electron microprobe line scan of a tube cross-section after SiO<sub>2</sub> deposition in opposing reactants geometry using 30% SiCl<sub>4</sub>-N<sub>2</sub> and 7% H<sub>2</sub>O-N<sub>2</sub>, for 1 hr.

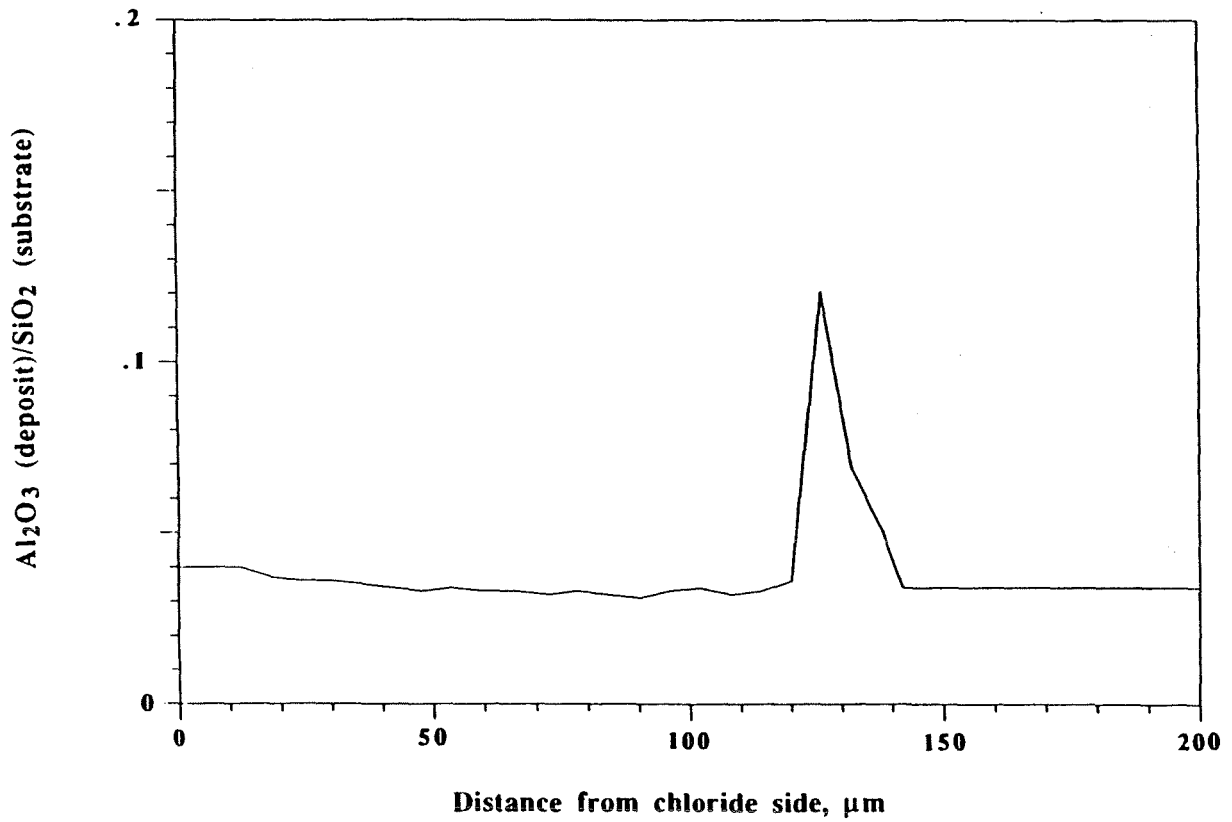


Figure 3.6 Electron microprobe line scan of a tube cross-section subjected to Al<sub>2</sub>O<sub>3</sub> deposition after pretreatment by AlCl<sub>3</sub>.

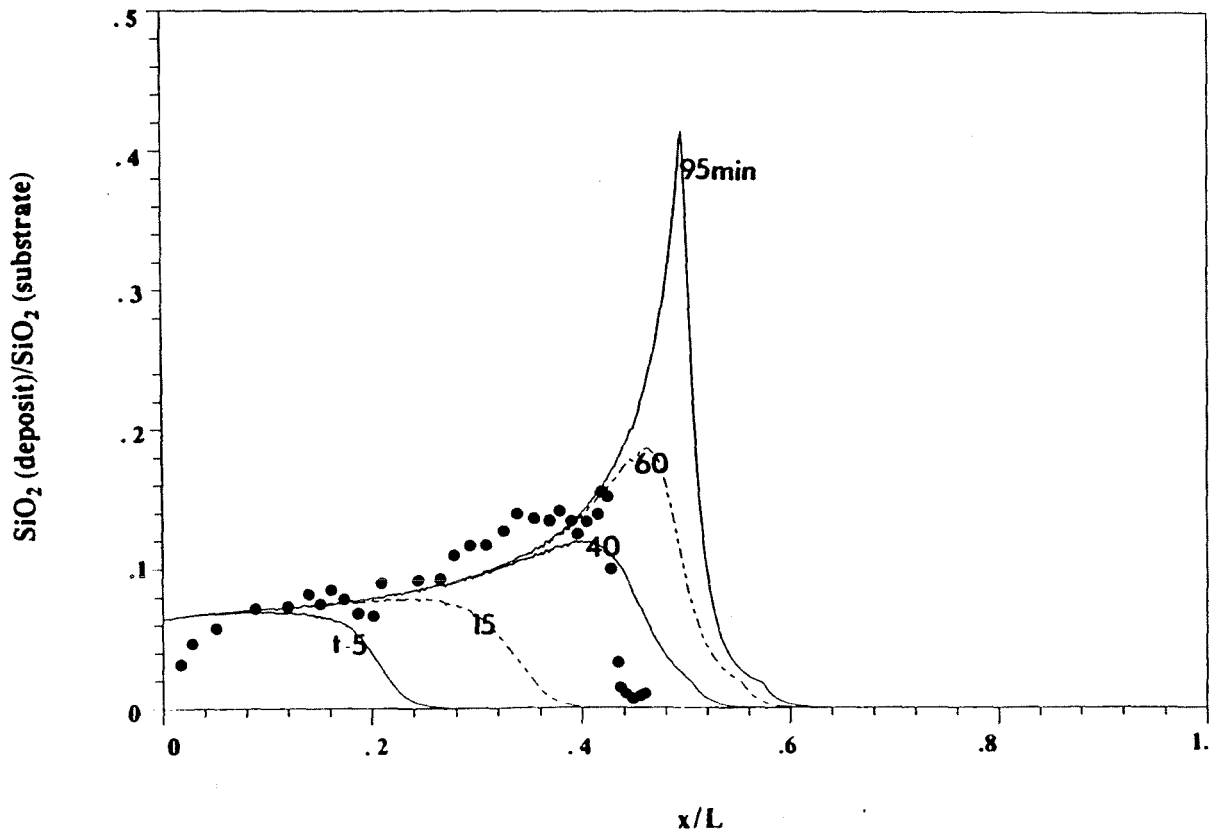


Figure 3.7 Simulated evolution of SiO<sub>2</sub> deposit at 800 °C in opposing reactants geometry using the parameter values given in Table 3.1 except  $C_{10} = 0.3 \text{ atm/RT}$ ,  $C_{20} = 0.07 \text{ atm/RT}$  (as in the experiments of Fig. 3.5). (●) Data of Fig. 3.5 replotted for comparison.

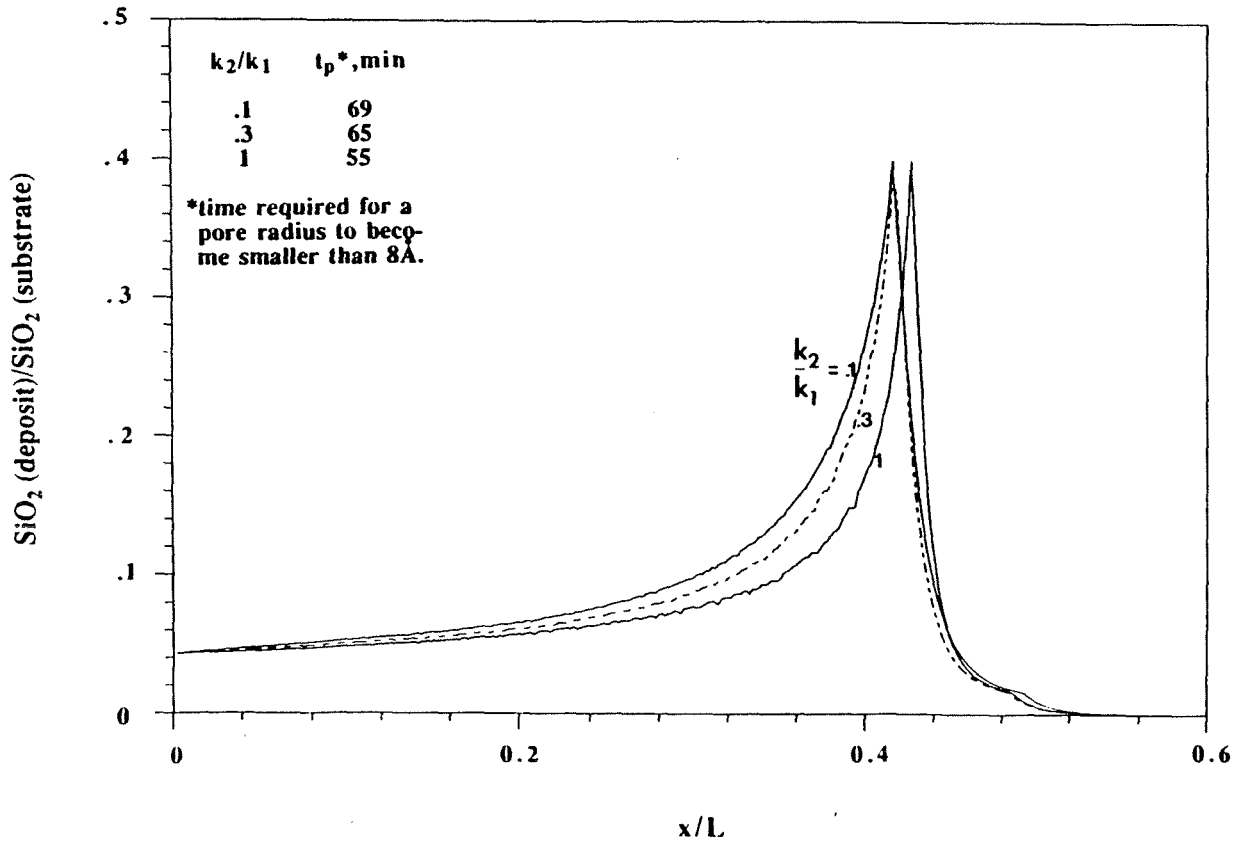


Figure 3.8 Simulated density profiles of the  $\text{SiO}_2$  layers at the end of deposition, for three different values of  $k_2/k_1$ . The corresponding deposition times are given in the Figure. Parameters values are given in Table 3.1.

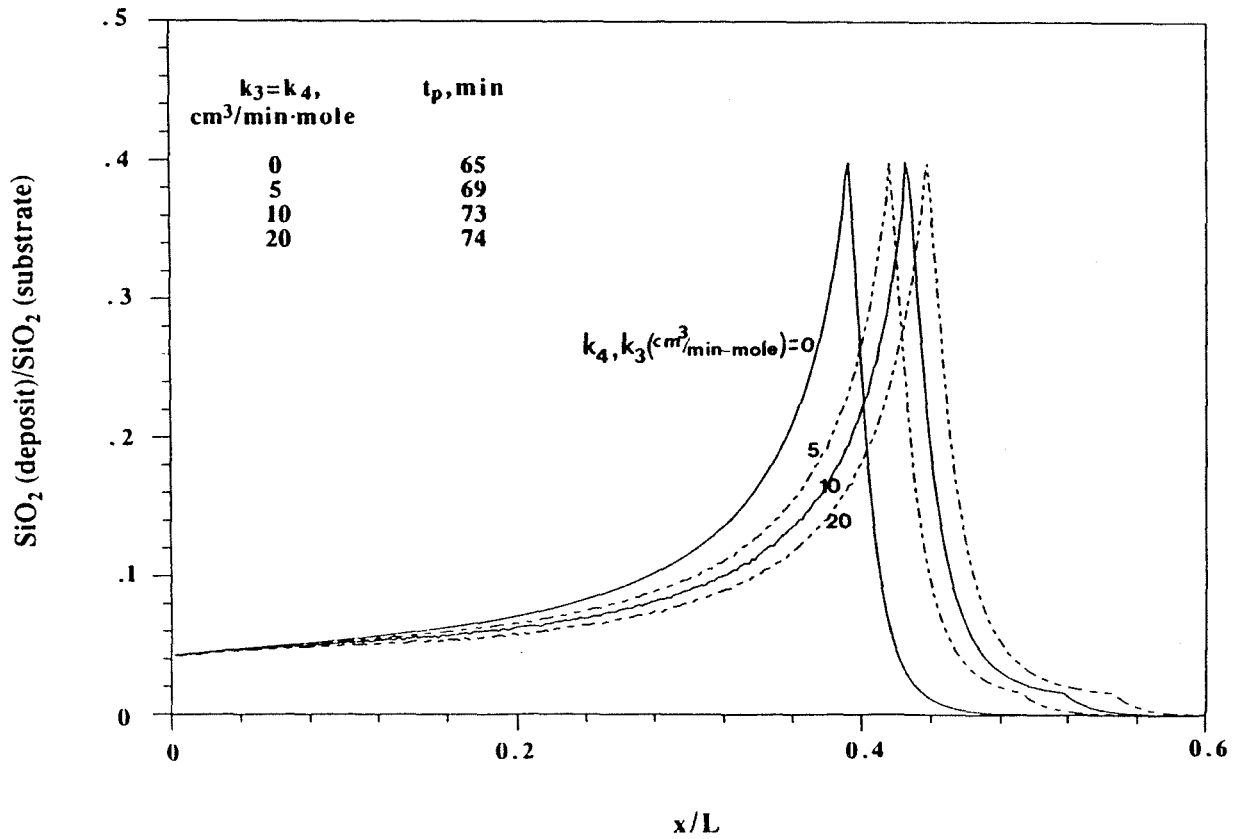


Figure 3.9 Effect of condensation reactions (Equations 3.4 and 3.5) on deposit profiles at the end of deposition.

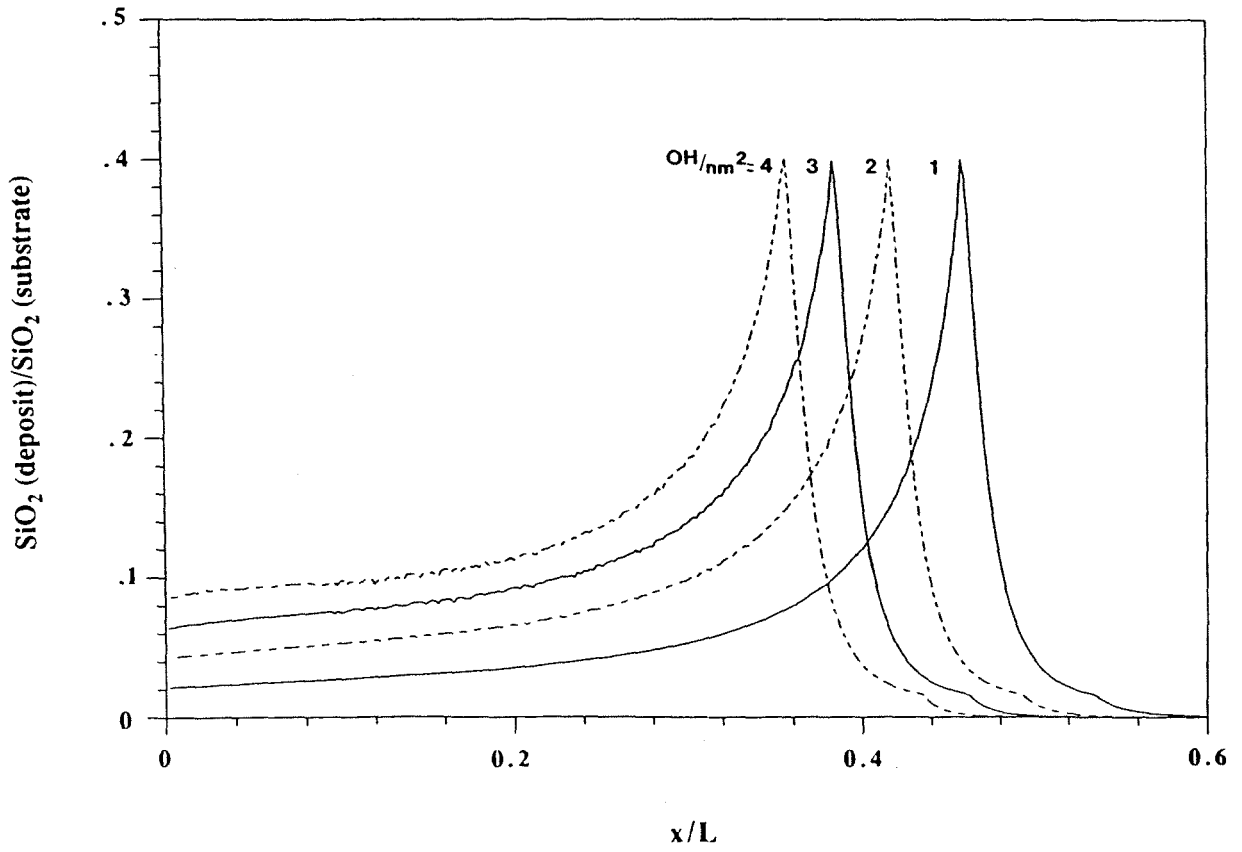


Figure 3.10 Simulated density profiles for different values of initial OH concentrations.

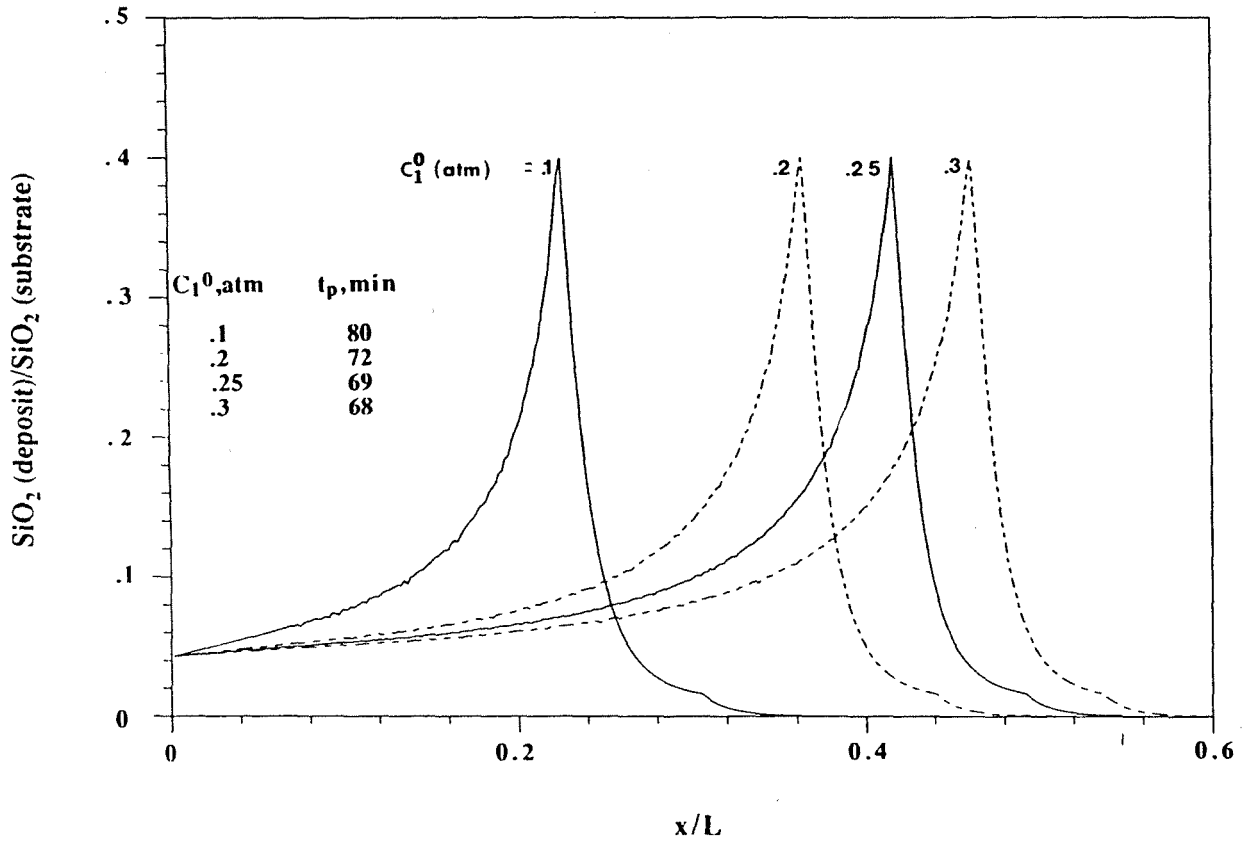


Figure 3.11 Effect of chloride concentration on deposit profile.

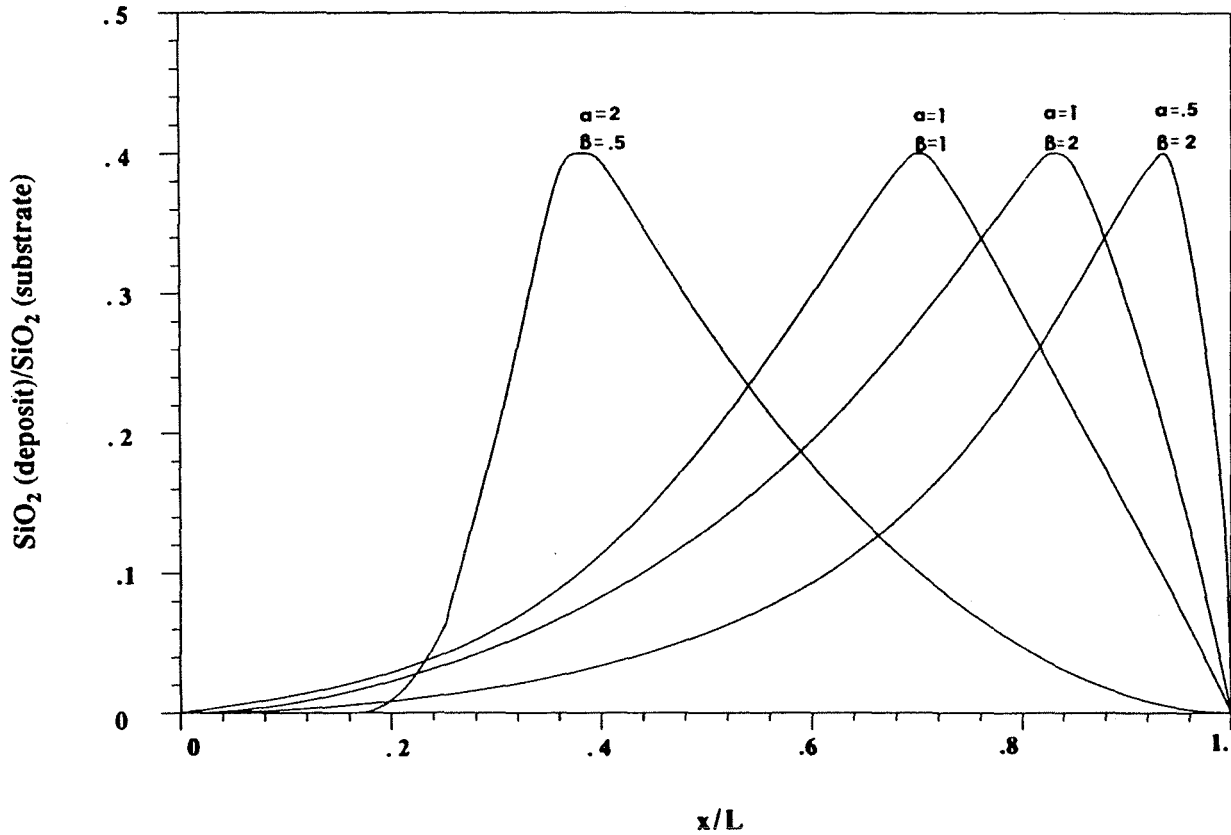


Figure 3.12 Simulated density profiles of SiO<sub>2</sub> layers at the end of deposition for four different combinations of reaction orders  $\alpha$  and  $\beta$  using the rate expression  $r = k C_{10}^{\alpha} C_{20}^{\beta}$ .

Deposition conditions are those of the experiment shown in Fig. 3.5.

## **CHAPTER 4**

### **Structure and Aging Characteristics of H<sub>2</sub>- permselective SiO<sub>2</sub>-Vycor Membranes**

In print *J. Membrane Sci.*  
(February 1994)

## Structure and Aging Characteristics of H<sub>2</sub>-permselective SiO<sub>2</sub>-Vycor Membranes

Michael Tsapatsis and George Gavalas

*Department of Chemical Engineering, California Institute of Technology,  
Pasadena, CA 91125*

### ABSTRACT

Hydrogen-permselective membranes were prepared by atmospheric pressure chemical vapor deposition (APCVD) of SiO<sub>2</sub> layers in porous Vycor tubes. The deposition was carried out by passing the reactants SiCl<sub>4</sub> and H<sub>2</sub>O through the bore of the support tubes at temperatures ranging from 600 °C to 800 °C. The deposit layers were examined by TEM, SEM, and EPMA. When the deposit was confined inside the pores of the Vycor substrate, the membranes were mechanically stable, but when it extended substantially outside of the porous matrix, the stresses induced by thermal cycling led to crack formation and propagation. Electron microscopy revealed that the SiO<sub>2</sub> deposit density is maximum in a region about 0.5 μm thick adjacent to the bore surface and gradually declines to zero within a depth of about 10 μm from the surface. The thin region of maximum deposit density is responsible for permselectivity, for it essentially blocks the permeation of nitrogen and larger molecules while allowing substantial permeation of hydrogen. This region contains about 10% by volume trapped voids and as a result has relatively high permeability as suggested by percolation theory. Annealing at high temperatures causes densification of the deposited material as evidenced by increased activation energy for H<sub>2</sub> permeation and correspondingly reduced permeance. The presence of H<sub>2</sub>O vapor accelerates the densification process. The densified membranes had a H<sub>2</sub> permeance as high as 0.1 cm<sup>3</sup>(STP)/min-atm-cm<sup>2</sup> at 500 °C and a H<sub>2</sub>/N<sub>2</sub> permeance ratio above 500.

## 4.1 INTRODUCTION

Inorganic membranes are currently of interest as potentially energy efficient separation alternatives to conventional processes like swing adsorption and cryogenic processes. Their main advantage is the ability to operate at elevated temperatures allowing direct coupling with reactions to increase the yield or selectivity. Increased yields for example can be attained by selective removal of one of the products in equilibrium-limited reactions. Hydrogen permselective membranes, in particular, have been considered for application to hydrogen sulfide decomposition and various hydrocarbon dehydrogenations (1-4).

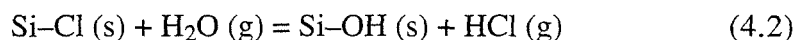
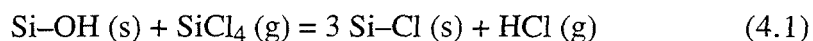
Some early studies have been concerned with the preparation and function of inorganic membranes with mesoporous separating films (4-7). These membranes have provided modest yield improvements in equilibrium limited dehydrogenations (e.g., ethane to ethylene), but their separation selectivity is limited to that of Knudsen diffusion. To fully exploit the potential of membrane reactors to combine reaction and separation in a single unit, membranes with high hydrogen selectivity would be required. One potential application is hydrogen production from coal gas. In this process a highly selective membrane can be integrated with the catalytic shift reactor to provide pure hydrogen suitable for ammonia production or other chemical synthesis.

Highly selective permeation properties are encountered only among certain dense (crystalline or amorphous), or ultramicroporous (molecular sieve) materials. Palladium, for example, is known to be very selective to hydrogen permeation, but the high material cost and the susceptibility to embrittlement are obstacles to large scale membrane applications (8). Dense silica glass and some other glasses are known to be highly selective towards helium and hydrogen (9) with nitrogen and other common gases having much lower permeabilities (10). Even for hydrogen, however, diffusion is activated (30-

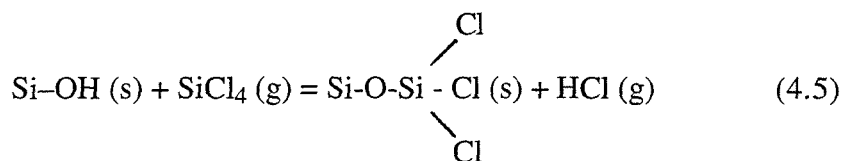
40 kJ/mole) and the absolute permeability is low. It is important, therefore, that the separation layer is very thin to obtain reasonable membrane permeance.

We have previously reported the preparation and characterization of hydrogen permselective membranes consisting of a thin SiO<sub>2</sub> layer formed by chemical vapor deposition (CVD) within the walls of porous Vycor tubes (11,12,13,14). In our recent work CVD is carried out using the reaction of SiCl<sub>4</sub> or related compounds with H<sub>2</sub>O at 600°-800 °C (13,14). The high reaction temperature and the presence of water vapor favor the deposition of a dense and stress free deposit layer. Other investigators have used the oxidation of triisopropyl silane to prepare silica membranes (15).

Deposition of silica layers on porous tubes can be carried out in the Opposing Reactants Geometry (ORG), i.e., passing one of the reactants through the bore and the other outside of the tube, or in the One-Sided Geometry (OSG), i.e., passing both reactants through the bore or outside of the tube. As detailed elsewhere (13), the hydrogen permeance of the membranes prepared by OSG is higher than the permeance of membranes prepared using ORG. Deposition of SiO<sub>2</sub> by SiCl<sub>4</sub> hydrolysis using ORG has been described and analyzed elsewhere (14). The deposit layer was found to have an asymmetric profile which was well explained by the heterogeneous nature of the reaction which is initiated at surface silanols (—Si-OH groups). The reaction can be described by the simplified scheme:



where (s) is used to identify surface species. In this notation one counts surface -OH and -Cl groups and not silicon atoms. Equation 4.1 can be written more analytically as:



In the OSG, the situation is more complicated. The heterogeneous reaction on the Vycor surface (Equations 4.1-4.4) is still the dominant process, but simultaneous generation of hydrous silicon oxide monomers, clusters and particles in the gas phase may also contribute to the deposit growth. To obtain good membrane permeance, deposition should take place within the pores of the support to form a thin and nonporous layer. The deposition of particles at the external surface of the support will most likely create a porous deposit unable to contribute to the separation function of the membrane. Good membrane properties are thus favored when the reaction proceeds by the heterogeneous mechanism and/or by deposition of monomers or small clusters formed in the gas phase which are able to penetrate the Vycor glass pore structure.

In this work we report results on the morphology, permeation properties and stability of silica membranes prepared by OSG deposition. Preparation conditions are identified under which the heterogeneous reaction is the dominant one. Under these conditions the deposit is confined inside the pores of the substrate and the membrane is stable. Conditions favoring gas phase reactions on the other hand are associated with a pronounced deposit extending outside of the support and often leading to membrane failure. TEM reveals significant residual porosity inside the deposit at the end of deposition. The influence of this remaining porosity on the permeation properties of the membrane is examined qualitatively using percolation theory arguments.

## 4.2 EXPERIMENTAL TECHNIQUES

### 4.2.1 CVD System

A detailed description and a schematic of the apparatus for Chemical Vapor Deposition is given elsewhere (13). The system consists of a porous Vycor tube (5 mm inside diameter, 1.1 mm wall thickness, 0.3 void fraction and 4.4 nm mean pore diameter, supplied by Corning Inc.) connected at both sides with nonporous quartz sections and secured concentrically inside a quartz shell heated by a furnace. The length of the porous section was 5-7 cm to avoid significant variations of reactants concentration in the axial direction. The reactants ( $\text{SiCl}_4$  and  $\text{H}_2\text{O}$ ) in  $\text{N}_2$  carrier were generated by bubblers and passed through the bore of the support Vycor tube. The concentrations of the reactants were controlled by regulating the temperature of the bubblers. Since the flowrates of the nitrogen streams through the bubblers were low it was assumed that the carrier gas was in each case saturated with the reactants. In order to suppress premature homogeneous reactions, the two reactants were introduced into the furnace by separate concentric quartz tubes and mixed about 5 cm before the porous section of the support. Before mixing, the two reactant streams were preheated in the initial 40 cm of the furnace thus eliminating temperature differences between the reactant stream and the porous support tube. Laminar flow conditions existed in the support conduit (Reynolds number  $<10$ ). For all experiments the total flowrate was approximately 200 cc/min. The permeation rates of various gases through the membrane under formation were measured with a sensitive pressure transducer interfaced to a computer (11,13).

### 4.2.2 SEM, EPMA, TEM

Polished cross-sections and inside (bore) surfaces of the membranes were examined by Scanning Electron Microscopy (SEM) with a Cam Scan electron microscope

operating at 15 kV, and by Electron Microprobe Analysis (EPMA) using a Jeol 733 Superprobe. For the EPMA analysis a low current (5nA) 5-10  $\mu\text{m}$  beam was used to avoid sample burning. Transmission Electron Microscopy (TEM) was performed on thin sections of the membranes prepared by ion milling or by ultramicrotomy. A Phillips 430 TEM operating at 300 kV was used throughout these studies. For ion milling the samples were first thinned mechanically in a dimpler and subsequently subjected to ion milling. For ultramicrotomy the samples were first vacuum impregnated with the precursor solution of an epoxy. After polymerization was completed, the sample was thinned by polishing and finally microtomed. The procedure was based on the technique developed by Ehret et al. (16). Ultramicrotomy gives sections of uniform thickness. Thus the transmission electron micrographs are readily interpretable for porosity variations. With ion milling sample thickness variations make the interpretation of the micrographs complicated. By comparing micrographs of untreated Vycor prepared by microtomy and ion milling, it was found that microtomy does not introduce artifacts during sample preparation. For the analysis of the deposited layers only microtomed samples were used. The image analysis technique described by Levitz et al. (17) was used.

#### ***4.2.3. Thermal and Hydrothermal Treatment***

The thermomechanical stability of the membranes was tested by thermal treatment under dry  $\text{N}_2$ . Since in some of the potential applications (e.g., water gas shift reaction) the membranes would be exposed to substantial partial pressures of water vapor, the permeation properties of the membranes were also tested during extended exposure to 3 atm of  $\text{H}_2\text{O}$  vapor and 7 atm of  $\text{N}_2$  at  $550^\circ\text{C}$ .

### 4.3 RESULTS AND DISCUSSION

For an understanding of the influence of the process parameters on the deposit characteristics, depositions were carried out at various temperatures and reactant concentrations.

#### 4.3.1 *Effect of H<sub>2</sub>O and SiCl<sub>4</sub> Concentrations*

A typical evolution of H<sub>2</sub> and N<sub>2</sub> permeances during deposition is shown in Figure 4.1. The course of the reaction was followed by measuring the H<sub>2</sub> and N<sub>2</sub> permeation rates every 5 minutes of deposition. During reaction the permeation of nitrogen decreased by a factor of ten or more, while the permeation of hydrogen remained almost unchanged. Pore plugging may be operationally defined as the point at which the N<sub>2</sub> permeance is 10% of its initial value. Figure 4.2 shows the time to pore plugging for various combinations of SiCl<sub>4</sub> and H<sub>2</sub>O concentrations at 600 °C. The general trend is that an increase of SiCl<sub>4</sub> or H<sub>2</sub>O concentration reduces the time to pore plugging ( $t_p$ ) except for depositions in which both concentrations are high (>8%). In that case  $t_p$  increases with concentration.

The internal surface of the tube (at the side of reactants flow) was examined by SEM. Figure 4.3a shows an SEM photograph of the internal surface (bore) of a Vycor support tube. A surface roughness of the order of 100 nm is revealed by the existence of pronounced depressions. The SEM photograph of the bore of a typical membrane immediately after pore plugging (15 minutes of deposition) is shown in Figure 4.3b. The membrane of Figure 4.3b was deposited under low concentration of SiCl<sub>4</sub>. Similar morphology is revealed for all other membranes deposited at 600°C with low concentrations of SiCl<sub>4</sub> and/or H<sub>2</sub>O (<5%) just after pore plugging. Comparison of Figures 4.3a and 4.3b reveals a roughness similar to that of the support tube indicating that the deposit does not extend significantly outside of the support.

To investigate the deposit evolution after pore plugging the deposition (under the conditions defined in Figure 4.3b) was extended for 15 and 35 additional minutes after pore plugging (30 and 50 total minutes of deposition). Examination of the bore of the tubes by SEM (Figure 4.4) indicates that after pore plugging the deposit continues to grow outside of the Vycor support. The influence of concentration variation on the morphology of the deposit is revealed by comparison of Figure 4.5 with Figure 4.3. Figure 4.5 is the SEM photograph of the bore of a tube after deposition with 8%  $\text{SiCl}_4$  and 13%  $\text{H}_2\text{O}$  for 30 minutes (immediately after pore plugging). In this case, with both reactants at high concentration, a pronounced surface roughness is observed indicating deposition of particles which are too big to enter the pores. More particles are observed down the reactor, consistent with a gas phase mechanism for particle formation. Considerable particle formation and deposition are similarly observed at 600 °C whenever the concentrations of both reactants are higher than about 5%. The depletion of reactants available for deposition in the pores can explain the increase in  $t_p$  observed at the high concentration region of Figure 4.2.

The above observations show that extension of the deposit layer outside of the porous matrix of the support occurs either by deposition of homogeneously formed particles (Figure 4.5) or by heterogeneous growth of the surface of the support when the reaction is prolonged beyond the time required for pore plugging (Figure 4.4). For membranes in which the deposit layer extends beyond the porous region, dynamic crack propagation is observed during temperature changes. The cracks start from the bore of the tube (at the location of the external deposit) and mostly extend along the inner wall, but in some cases they propagate within the Vycor support as shown in Figure 4.6. These cracks seem to be caused by thermomechanical stresses. They can be avoided when care is taken to change the temperature very slowly ( $\sim 1^\circ \text{C}/\text{min}$ ). When the deposit is confined inside the pores of Vycor, no such cracks can be initiated. Thus in order to avoid crack

formation, low enough concentrations of reactants should be used and the deposition should not be extended beyond the time that is required to achieve pore plugging.

The depth of penetration of the deposit inside the wall of the support tube is determined by the reaction Thiele modulus. An increase in the Thiele modulus will result in a thinner deposit layer and, hence, in a more permeable membrane. In the experiments described below a higher temperature was used in an attempt to increase the Thiele modulus while using sufficiently low  $\text{SiCl}_4$  concentration to minimize homogeneous particle formation.

#### ***4.3.2 Effect of Deposition Temperature***

Deposition runs were carried out using 2.7%  $\text{SiCl}_4$  and 13%  $\text{H}_2\text{O}$  at 600, 650 and 750 °C. At these concentrations no external deposition was observed provided the reaction time was carefully controlled. Five additional minutes of deposition at 750 °C were enough to give morphologies similar to the one shown in Figure 4.4. In a kinetically controlled deposition the reciprocal of the time required for pore plugging,  $1/t_p$ , is proportional to the deposition rate. Figure 4.7 is an Arrhenius plot of  $1/t_p$  for depositions up to 750 °C. An activation energy of 17 kcal/mole is calculated which is somewhat lower than the 22 kcal/mole value of the activation energy of the heterogeneous reaction (4 and references therein). The mass transfer resistance from the free stream to the bore surface and depletion of OH groups with increasing temperature can easily account for such a difference.

#### ***4.3.3 Thermal and Hydrothermal Treatment***

Silicon dioxide formed by CVD is known to undergo densification upon exposure to high temperatures. This densification is accelerated by  $\text{H}_2\text{O}$  vapor (12 and references therein). Figure 4.8 shows the  $\text{H}_2$  permeance and associated activation energy versus time

of annealing under dry N<sub>2</sub> for a membrane developed by a 5 min deposition at 750 °C using 2.7% SiCl<sub>4</sub> and 13% H<sub>2</sub>O. For the estimation of the activation energy the fluxes were adjusted for the effect of the resistance of the porous tube as in reference (11):

$$\frac{1}{K_{sl}} = \frac{1}{K} - \frac{1}{K_{sub}} \quad (4.6)$$

Where K<sub>sl</sub>, K and K<sub>sub</sub> are the permeances through the separation layer, the composite membrane and the untreated substrate respectively. The data are given in Table 4.1.

It has been suggested that densification by thermal treatment involves removal of silanol groups (Si-OH) in the SiO<sub>2</sub> deposit accompanied by formation of additional Si-O-Si bonds. Water vapor strongly catalyses the rearrangement of siloxane bonds and accelerates the densification (12).

During heat treatment in the presence of 3 atm water vapor, the hydrogen permeance declines more drastically, by up to a factor of 6 compared to the permeance of the as deposited membrane, as shown in Table 4.2. After adjustment for the resistance of the support tube which remains constant (11), the permeance decline of the separation layer is almost by a factor of 10. The permeance of nitrogen also declines, however, so that the selectivity remains about the same. The activation energy for hydrogen permeance after hydrothermal treatment varied somewhat from membrane to membrane but was generally in the range 25 - 30 kJ/mol as compared to 10-15 kJ/mol for the membranes before treatment. This increase of the activation energy can account for the decline of hydrogen permeance during the hydrothermal treatment.

Since it is possible that HCl produced during densification (reaction 4.4) attacks the SiO<sub>2</sub> deposit, the role of chloride groups incorporated during deposition on the subsequent decline of permeance was also examined. From EPMA and EDAX analysis the deposit Cl/Si atom ratio is up to .07 immediately after deposition. After two days of hydrothermal treatment, no appreciable amount of Cl could be detected anymore. The relatively fast

elimination of chloride groups suggests that the role of HCl is not of major importance because changes in permeance are observed for up to nine days of hydrothermal treatment.

Membranes developed by deposition at 750°C show the best stability characteristics. After nine days of hydrothermal treatment, the permeance was about 0.1 cm<sup>3</sup>(STP)/cm<sup>2</sup>-min-atm at 500°C and remained the same after 13 days of additional treatment. It must be noted that the measurement of the very small nitrogen permeance is subjected to considerable error from any small leaks in the system. Hence the true nitrogen permeances may be considerably lower than the measurements indicate.

#### ***4.3.4 Characterization of the Permselective Layer***

Defocus contrast electron microscopy was used to characterize thin membrane cross sections. The technique is based on the fact that electrons propagate slower through a dense phase of a material than through a lower density phase. The resulting phase shift under the right imaging conditions can be used to image a material based on its density variations. A theoretical treatment of the technique is given by Ruhle (18). Here it suffices to note that if the image is focused at some distance  $\Delta f < 10,000 \text{ \AA}$ , above the specimen, the voids (pores) are imaged as bright spots. The size of the projections is representative of the pore size for pores with diameter greater than about 10 Å.

Figure 4.9 is a micrograph of untreated Vycor. The distribution of the matrix SiO<sub>2</sub> (dark) and the pore structure (white) is evident. The long range density changes evident in the figure (of the order of several thousands Å) are introduced by the sectioning in the microtome and do not reflect the glass structure. The short range density fluctuations (of the order of several Angstroms) is the high resolution image detail dominated by the microscope transfer function and forms an added background on the medium-scale image detail (>10 Å) relevant to the pore structure.

After background subtraction the binary image is extracted using the "Image" (Version 1.33) program for the Macintosh. A part of the micrograph of untreated Vycor along with the corresponding binary image in which the pore structure is in black is given in Figure 4.10.

The black area of the binary image in Figure 4.10 is the projection of the pore structure of a thin slice of Vycor glass (the typical thickness of the microtomed specimens collected was about 400 Å). To extract quantitative information from the image one needs a model of the pore structure. For the purpose of this study, and as a first approximation, we follow reference (16) and consider the micrograph as a 2D section of Vycor glass. This assumption is justified by the fact that the correlation length of the pore structure of Vycor (16) is roughly equal to the sample thickness. The void fraction could therefore be estimated from the ratio of the black area over the total area analyzed.

The pore structure was analyzed using a standard "chord analysis" (16). The most probable chord length is associated with the pore diameter. From the image analysis we obtained  $\epsilon_0 = .35$  and  $\bar{d} = 47$  Å in good agreement with  $\epsilon_0 = .30$  and  $\bar{d} = 44$  Å provided by Corning Inc. (using adsorption). Representative micrographs taken across a membrane formed using 13% H<sub>2</sub>O and 2.7% SiCl<sub>4</sub> at 600°C are shown in Figure 4.11. A similar analysis as for the untreated Vycor gives the  $\epsilon$  and  $\bar{d}$  values shown in Table 4.3.

Figure 4.12 shows  $\epsilon/\epsilon_0$  versus distance from the side of reactants flow. The void fraction is minimum (about one-third of its original value) at the wall and gradually grows to its original value within about 10 μm from the wall. Inspection of TEM micrographs such as that shown in Figure 4.13 suggests that the minimum void fraction (maximum SiO<sub>2</sub> deposit) persists for at least 0.5 μm from the wall. This sublayer of minimum  $\epsilon$  is evidently impervious to SiCl<sub>4</sub>, and quite impermeable to N<sub>2</sub> but much more permeable to hydrogen thus providing the separation function of the membrane. In the remaining part of

the deposit layer, the pores are partially constricted and do not provide significant molecular sieving, although they decrease the permeance of all gases.

Intrapore deposition ceases when all open paths for  $\text{SiCl}_4$  penetration have been interrupted. The separation layer at that point contains a residual (trapped) porosity, approximately one-third of the original porosity or about 0.1 void fraction on an absolute basis. Similar residual void fraction was estimated from TGA experiments (19). This residual porosity is readily explained by percolation theory. Initially the pore diameter varies from pore to pore and along the length of a single pore. As deposition progresses, the pores having the narrowest cross section will become blocked, and as more pores become blocked, small clusters of incompletely filled pores become isolated. When the fraction of blocked pores exceeds a critical value (which depends on the mean coordination number of the matrix), the pore network loses its connectivity and the reactant  $\text{SiCl}_4$  cannot penetrate any longer into the interior of the pore matrix. Reaction continues on the external surface and on small pore clusters accessible to the external surface. This process leaves behind clusters of pores which, although not completely filled, are nevertheless inaccessible to the reactant. As will be seen below, these pores have an important effect on hydrogen permeance. Trapped porosity is also observed in ORG deposition of  $\text{SiO}_2$ ,  $\text{Al}_2\text{O}_3$  and  $\text{TiO}_2$  (13,14). The volume fraction of trapped porosity may increase somewhat during hydrothermal annealing and densification.

#### *4.3.5 Effect of Trapped Porosity on the $\text{H}_2$ Permeance*

The characteristics of the separation layer can be examined more closely by comparing its permeance with that of compact Vycor glass. The comparison is meaningful only for membranes that have undergone hydrothermal treatment after which their activation energy for hydrogen permeance is close to that of nonporous Vycor (about 32 kJ/mol (23)). For example, the hydrogen permeance of the membrane of Figure 4.13 was

.033(cm<sup>3</sup>(STP) / cm<sup>2</sup>-min-atm) at 450 °C after hydrothermal treatment. The permeability of nonporous Vycor glass at the same temperature is given as  $0.6 \times 10^{-7}$  and  $2.4 \times 10^{-7}$  (cm<sup>3</sup> (STP)-cm / cm<sup>2</sup>-min-atm) in references (20) and (23) respectively. According to these values, the membrane of Figure 4.13 has the same hydrogen permeance as a .02 to .07 μm thick slab of nonporous Vycor.

On the other hand, the TEM results show that the separation layer over which the deposit density is maximum has thickness of about 0.5 μm. It appears, therefore, that the permeability of the separation layer is about 7 to 25 times higher than that of nonporous Vycor glass depending on the value used for the permeability of nonporous Vycor. The difference becomes even more pronounced if we take into account that the 0.02-0.07 μm layer of nonporous Vycor is equivalent to the whole membrane and not just to the separation layer. The large difference in the permeabilities of the SiO<sub>2</sub> deposit and of nonporous Vycor glass cannot be attributed to residual -OH groups and other defects in the deposit, for the activation energy (after hydrothermal treatment) is close to that of nonporous Vycor. The difference is more likely due to supramolecular features and, in particular, to the residual trapped porosity.

In the last part of this chapter we apply results of percolation theory to estimate the permeability of the separation layer. The analysis shows that trapped porosity near the percolation threshold significantly magnifies the permeability of the material explaining the experimental findings. In view of the crude network representation employed for the separating layer, this analysis has only qualitative significance.

#### ***4.3.6 Estimation of Membrane Permeability Based on Percolation Theory***

The purpose of the following qualitative analysis is to explore the effect of trapped porosity on the permeability of the separation layer. For this purpose the separation layer can be considered as a composite structure consisting of dense SiO<sub>2</sub> (phase 2) and porous

inclusions (phase 1). Phase 1 has much higher H<sub>2</sub> diffusivity than phase 2. The composite structure is very near the percolation threshold of phase 1. The problem, in its simplest form, is equivalent with one of finding the effective diffusional conductance,  $\langle\sigma\rangle$ , of a composite structure consisting of two materials with finite but widely different conductances,  $\sigma_1 \gg \sigma_2$ . The diffusional flux through a cylindrical pore with radius  $r_1$  and length  $l$  is given by:

$$J_1 = 22400 \frac{\pi D(r_1) r_1^2}{l} \Delta c, \text{ in cm}^3(\text{STP})/\text{min} \quad (4.7)$$

where  $D(r_1)$  is the diffusion coefficient and  $\Delta c$  is the concentration difference of the diffusing species over the pore length. For Knudsen diffusion the diffusivity is given by:

$$D(r_1) = 5.82 \times 10^5 \sqrt{\frac{T(\text{K})}{M}} r_1(\text{cm}), \text{ in cm}^2/\text{min} \quad (4.8)$$

where  $T$  is the absolute temperature and  $M$  the molecular weight of the diffusing species.

The flux through a pore filled with SiO<sub>2</sub> is:

$$J_2 = \frac{\pi A r_2^2}{l} \Delta P, \text{ in cm}^3(\text{STP})/\text{min} \quad (4.9)$$

where  $A$  is the gas permeability through SiO<sub>2</sub>, in  $\frac{\text{cm}^3(\text{STP})\text{-cm}}{\text{cm}^2\text{-min-atm}}$ . Diffusional conductances  $\sigma_1$  and  $\sigma_2$  can be defined by the relations:

$$\sigma_1 = 22400 \frac{\pi D(r_1) r_1^2}{l} \quad (4.10)$$

$$\sigma_2 = \frac{\pi A r_2^2 R T}{l} \quad (4.11)$$

Using  $A_{H_2} = 0.6 \times 10^{-7} \frac{\text{cm}^3 (\text{STP})\text{-cm}}{\text{cm}^2\text{-min-atm}}$  taken from reference (20) we have:

$$\left( \frac{\sigma_1}{\sigma_2} \right)_{H_2} = 7.60 \times 10^5 (r_1/r_2)^2 r_1(\text{\AA}) \quad (4.12)$$

or:

$$\left( \frac{\sigma_1}{\sigma_2} \right)_{H_2} = 7.60 \times 10^5 (\varepsilon_1/\varepsilon_2) r_1(\text{\AA}) \quad (4.13)$$

where  $\varepsilon_1$  and  $\varepsilon_2$  are the volume fractions of phases 1 and 2 respectively.

The permeability can be estimated by representing the composite material as a random 3D network consisting of bonds with conductances  $\sigma_1$  and  $\sigma_2$  ( $\sigma_1 \gg \sigma_2$ ) where the fraction  $p$  of bonds with conductance  $\sigma_1$  is at the percolation threshold  $p_c$ . According to Straley (21), the total conductivity at the percolation threshold  $\langle \sigma \rangle$  follows the power law:

$$\langle \sigma \rangle \sim \sigma_1^{1-u} \sigma_2^u \quad \text{or} \quad \langle \sigma \rangle / \langle \sigma \rangle_2 = (\sigma_1 / \sigma_2)^{1-u} \quad (4.14)$$

where  $\langle \sigma \rangle_2$  is the total conductivity when all bonds have conductance  $\sigma_2$ . Equation 4.14 suggests that the total conductivity at the percolation threshold can be estimated from the ratio of the conductivities of the two phases. For a three dimensional network  $u \approx 0.72$  (21). Thus for  $r_1 = 10 \text{\AA}$ , and  $\varepsilon_1/\varepsilon_2 = 0.1 / 0.9$  (the pore radius and volume fractions estimated from TEM), one has:

$$\left( \frac{\langle \sigma \rangle}{\langle \sigma \rangle_2} \right)_{H_2} = 45$$

Using  $A_{H_2} = 2.4 \times 10^{-7} \frac{\text{cm}^3 (\text{STP})\text{-cm}}{\text{cm}^2\text{-min-atm}}$  (23) we find:

$$\left( \frac{\langle \sigma \rangle}{\langle \sigma \rangle_2} \right)_{H_2} = 30$$

This numerical estimate for the enhancement of hydrogen permeability is higher than the experimental values of 7-25 obtained earlier. The analysis nevertheless shows that the trapped porosity can enhance greatly the hydrogen permeability. A similar analysis for nitrogen permeability shows that the trapped porosity can reduce correspondingly the H<sub>2</sub>:N<sub>2</sub> selectivity. A comparison of predicted and experimental selectivities was not undertaken in view of the uncertainty of the measured N<sub>2</sub> permeance.

The above network model also predicts that the activation energy for the composite material will be about 72% of that for nonporous SiO<sub>2</sub>. Using an activation energy of 32 kJ/mol (23) for nonporous Vycor the predicted activation energy is 23 kJ/mol, somewhat lower than the experimentally determined values for densified membranes (25-30 kJ/mole).

Although in the above treatment the material was assumed to be at the percolation threshold,  $p = p_c$ , the details of deposition (for instance the point at which the deposition is terminated) and the subsequent densification processes (possible deposit redistribution by Ostwald ripening) influence how close to the threshold the pore structure is. A quantitative analysis would require a more realistic model for the composite structure, including among other things the size distribution of the trapped voids.

#### 4.4 CONCLUSIONS

The thermal-mechanical stability of SiO<sub>2</sub> membranes prepared by CVD depends on the location of the deposit layer. The membranes are stable if the deposition conditions are carefully chosen to confine the deposit inside the pores of the support. Prolonged exposure of the membranes to high temperatures and water vapor causes a structural rearrangement decreasing the hydrogen permeance to a stable value 5-10 times lower than its initial value. Upon completion of reaction the deposit layer comprises a sublayer of maximum density

about 0.5  $\mu\text{m}$  thick, which provides the separation function of the membrane and a much thicker region (about 10  $\mu\text{m}$ ) of gradually decreasing density. The 0.5 $\mu\text{m}$  sublayer contains a certain volume fraction (about 10%) of trapped porosity that became inaccessible at the end of deposition. This trapped porosity confers to the sublayer permeability much higher than that of the nonporous material.

## **ACKNOWLEDGEMENT**

The authors acknowledge the funding of this work by the Department of Energy, University Coal Research Program, under grant DE-FG22-92PC92525. Corning Inc. has supplied the porous Vycor glass tubes used as membrane supports.

## REFERENCES

1. Shindo, Y., T. Hakuta, H. Yoshitome and H. Inoue, "Separation of H<sub>2</sub>-CO mixtures with porous glass membranes in the intermediate flow region," *J. Chem. Eng. Japan* **19**, 186 (1986).
2. Kameyama, T., H. Dokiya, M. Fujishige, H. Yokokawa and K. Fukuda, "Possibility for effective production of hydrogen from hydrogen sulfide by means of a porous Vycor glass membrane," *Ind. Eng. Chem. Fundam.* **20**, 97 (1981).
3. Sun, Y. H. and S. J. Khang, "Catalytic membrane for simultaneous chemical-reaction and separation applied to a dehydrogenation reaction," *Ind. Eng. Chem. Res.* **27**, 1136 (1988).
4. Tsotsis T. T., A. M. Champagnie, S. P. Vasileiadis, Z. D. Ziaka and R. G. Minet, "The enhancement of reaction yield-through the use of high temperature reactors," *Separation Science and Technology* **28 (1-3)**, 397 (1993).
5. Leenaars, A. F. M. and A. J. Burgraaf, "The preparation and characterization of alumina membranes with ultra fine pores," *J. Colloid Interface Sci.* **105**, 27 (1985).
6. Okubo, T., K. Horuta, K. Kusatabe and S. Morooka, "Preparation of a sol-gel derived thin membrane on a porous ceramic hollow fiber by the filtration technique," *J. Membrane Sci.* **59**, 73 (1991).

7. Cini, P., S. R. Blaha, M. P. Harold and K. Venkataraman, "Preparation and characterization of modified tubular ceramic membranes for use as catalysts supports," *J. Membrane Sci.* **55**, 199 (1991).
8. Gryaznov, V. M., V. S. Suirnov and H. G. Slin'ko, in: Proc. Fifth International Congress Catalysis, The High Cost of Palladium, Vol. 2, North-Holland Publishing Co., Amsterdam (1973) p. 1139.
9. Shelby, J.E., Molecular Solubility and Diffusion, in: M. Tomazawa and R. H. Doremus (Eds.), Treatise of Materials Science and Technology, Vol. 17, Academic Press, N.Y. (1979).
10. D. C. Boyd and D. A. Thompson, Glass, in: Kirk-Othmer Encyclopedia of Chemical Technology, 3rd edition, Vol. 11, John Wiley, New York, N.Y. (1980), pp. 807-880.
11. Gavalas, G. R., C. E. Megiris and S. W. Nam, "Deposition of H<sub>2</sub>-permselective SiO<sub>2</sub> films," *Chem. Eng. Sci.* **44**, 1829 (1989).
12. Nam S.W. and G. R. Gavalas, "Stability of H<sub>2</sub>-permselective SiO<sub>2</sub> films formed by chemical vapor deposition," *AIChE Symp. Ser.* **85**, No. 268, 68 (1989).
13. Tsapatsis, M., S. Kim, S. W. Nam and G. R. Gavalas, "Synthesis of H<sub>2</sub>-permselective SiO<sub>2</sub>, TiO<sub>2</sub>, Al<sub>2</sub>O<sub>3</sub> and B<sub>2</sub>O<sub>3</sub> membranes from the chloride precursors," *Ind. Eng. Chem. Res.* **30**, 2152 (1991).

14. Tsapatsis, M. and G. R. Gavalas, "A kinetic model of membrane formation by CVD of SiO<sub>2</sub> and Al<sub>2</sub>O<sub>3</sub>", *AIChE J.* **38**, 847 (1992).
15. Megiris, C. E. and J. H. E. Glezer, "Synthesis of H<sub>2</sub>-permselective membranes by modified chemical vapor deposition - microstructure and permselectivity of SiO<sub>2</sub>/C/Vycor membranes," *Ind. Eng. Chem. Res.* **31** (5), 1293-1299 (1992).
16. Ehret, G., J. L. Grovisier and J. P. Eberhart, "A new method for studying leached glasses: analytical electron microscopy on ultramicrotomic thin sections," *Journal of Non-Crystalline Solids* **86**, 72-79 (1986).
17. Levitz, P., G. Ehret, S. K. Shinha and J. M. Drake, "Porous Vycor glass: The microstructure as probed by electron microscopy, direct energy transfer, small angle scattering, and molecular adsorption," *J. Chem. Phys.* **95** (8), (1991).
18. Ruhle, M.R., Transmission electron microscopy of radiation induced defects, in: Proc. Int. Conf. Radiation Induced Voids in Metals, U.S. Atomic Energy Commission, Washington D.C.(1972) pp. 256-291.
19. Kim, S.J. and G. R. Gavalas, "Thermogravimetric study of the reactions of chlorosilanes with the surface of Vycor glass," (accepted for publication *J. of Colloid and Interface Sci.* ).
20. Leiby, C. C., Jr. and C. L. Chen, "Diffusion coefficients, solubilities and permeabilities for He, Ne, H<sub>2</sub>, N<sub>2</sub> in Vycor Glass," *J. Appl. Phys.*, **31**, 268 (1960).

21. Straley, J. P., "Critical exponents for the conductivity of random resistor lattices," *Phys. Rev. B.*, **15**, 5773 (1977).
22. Haulin, S. and A. Bunde, Percolation II, in: A. Bunde and S. Harlin (eds.), *Fractals and Disordered Systems*, Chapter 3, Springer Verlag, Berlin Heidelberg (1991) pp. 96-149.
23. Altemose, V. O., Gas permeation through glass, in: *Seventh Symposium on the Art of Glassblowing*, The American Scientific Glassblowing Society, Wilmington, Del. (1962).

**Table 4.1.** Hydrogen Permeance Evolution During Heat Treatment at 550°C Under Dry Nitrogen

Temperature, °C	Gas Permeance, cm <sup>3</sup> (STP)/cm <sup>2</sup> -min-atm				
	Untreated Vycor	After Deposition	After 3 Days	After 7 Days	After 21 Days
450	0.550	0.385	0.186	0.186	0.202
600	0.520	0.397	0.230	0.238	0.258
700	0.400	0.400	0.250	0.252	0.267

**Table 4.2. Conditions of Deposition and Permeances of the Resulting Membranes as Deposited and After Heat Treatments in Dry and Wet N<sub>2</sub>**

Treatment I 12 hrs under N<sub>2</sub> at 750°C  
 Treatment II 2 days at 550°C under 3 atm water and 7 atm N<sub>2</sub>  
 Treatment III 7 days at 500°C under 3 atm water and 7 atm N<sub>2</sub>  
 Treatment IV 13 days at 500°C under 3 atm water and 7 atm N<sub>2</sub>

Temp- erature °C	t <sub>p</sub> ** min	Deposition Time min	Reactants Concentrations, atm				Gas Permeance at 600°C cm <sup>3</sup> (STP)/cm <sup>2</sup> -min-atm									
			SiCl <sub>4</sub>		H <sub>2</sub> O		As Deposited		After Treatment I		After Treatments I&II		After Treatments I, II & III		After Treatments I, II, III & IV	
							N <sub>2</sub>	H <sub>2</sub>	N <sub>2</sub>	H <sub>2</sub>	N <sub>2</sub>	H <sub>2</sub>	N <sub>2</sub>	H <sub>2</sub>	N <sub>2</sub>	H <sub>2</sub>
600	37.5	40	0.027	0.01	0.012	0.31	0.0018	0.37	0.001	0.18	0.0008	0.10				
600	22.5	25	0.027	0.07	0.0075	0.40	0.003	0.37	0.0009	0.14	0.0005	0.075				
600	12.5	20	0.027	0.13	0.004	0.41	0.001	0.37	0.0002	0.15	0.0002	0.068				
600	32.5	35	0.087	0.01	0.011	0.40	0.002	0.40	0.0006	0.17						
600*	22.5	30	0.087	0.13	0.005	0.42										
750	3.0	5	0.027	0.13	0.002	0.40	0.0007	0.33	0.0006	0.25	0.0001	0.12	0.0001	0.11		

\*Develops cracks during Treatment I.

\*\* Time for pore plugging (see text).

**Table 4.3.** Void Fractions and Mean Radii at Various Positions Across the Membrane (Estimated from TEM)

Distance( $\mu\text{m}$ ) from Reactants Side	Void Fraction	Mean Pore Diameter ( $\text{\AA}$ )
0.1	.12	20.8
2.0	.14	22.0
3.0	.16	36.4
4.0	.21	35.0
6.0	.27	36.4
7.0	.28	41.6
10.0	.32	43.0
untreated	.35	46.8

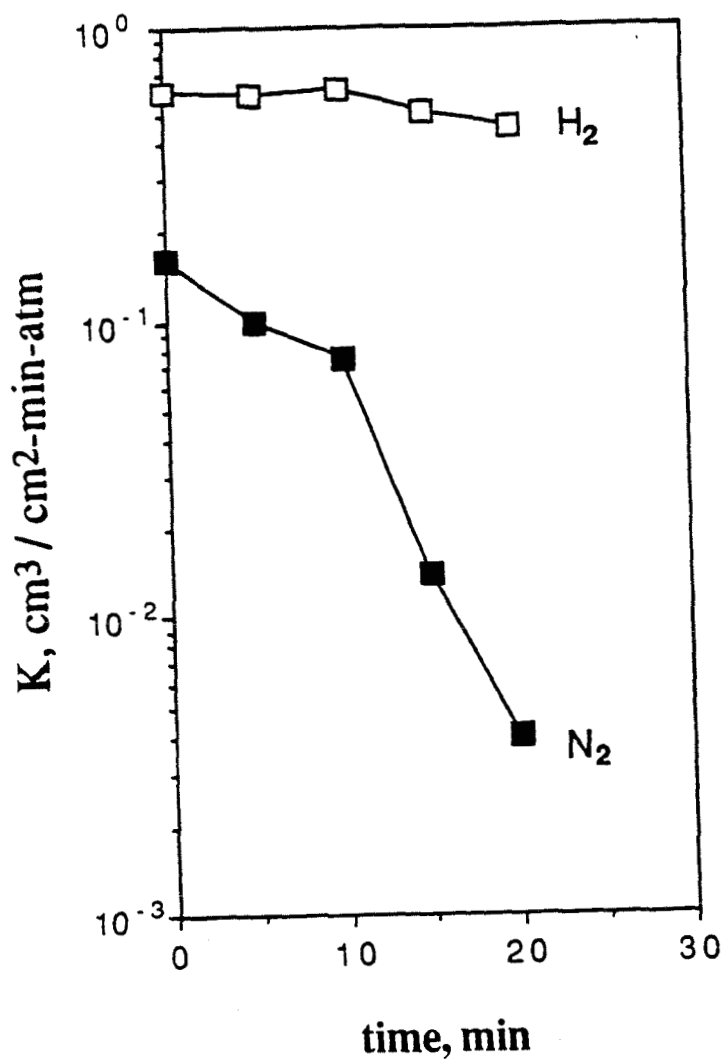


Figure 4.1 Evolution of H<sub>2</sub> and N<sub>2</sub> permeances during OSG deposition at 600°C. Reactant stream was 2.7% SiCl<sub>4</sub> and 13% H<sub>2</sub>O in N<sub>2</sub>.

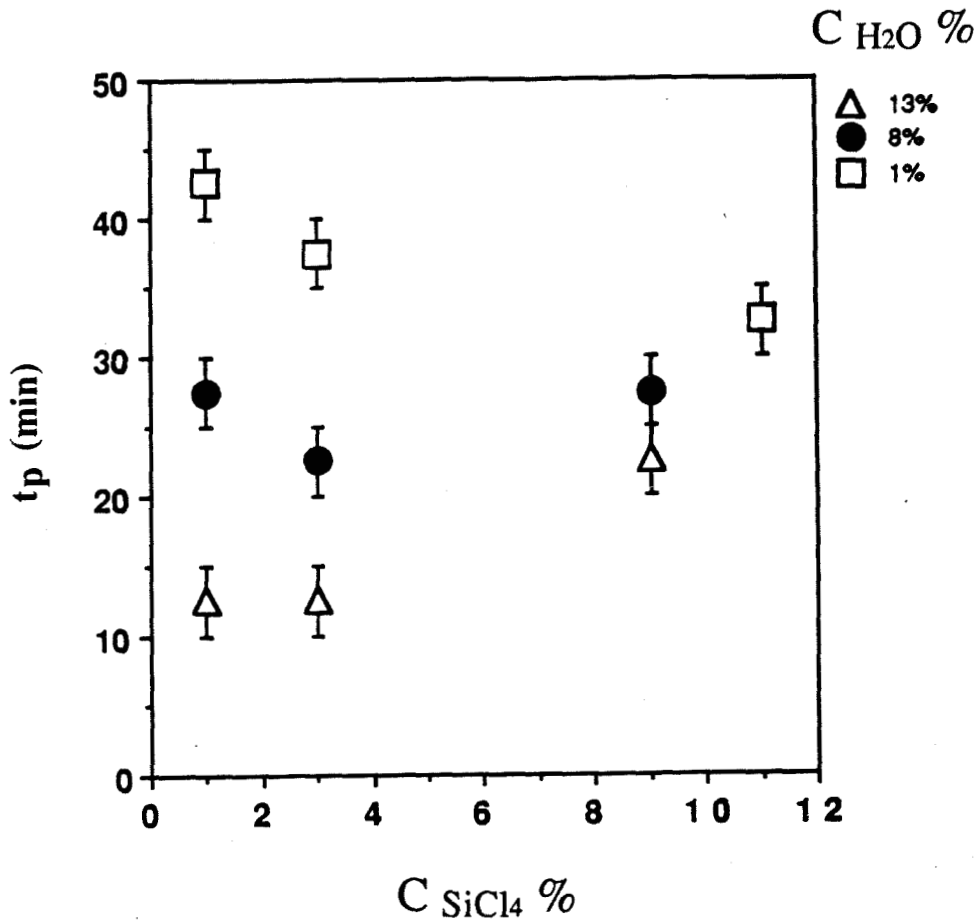


Figure 4.2 Time to pore plugging,  $t_p$ , for various combinations of  $\text{SiCl}_4$  and  $\text{H}_2\text{O}$  concentrations at  $600^\circ\text{C}$ .

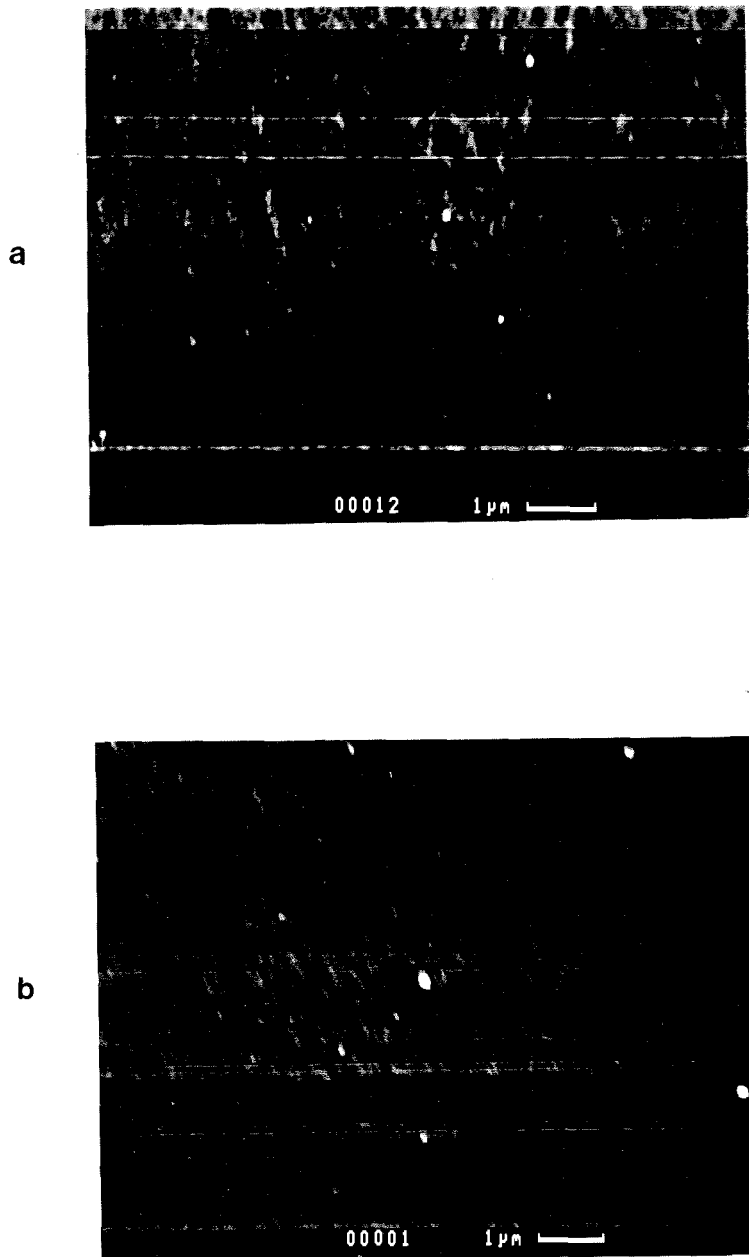


Figure 4.3 SEM micrographs of the bore surface of Vycor tubes. **a**: before deposition, **b**: after 15 minutes of deposition (time to pore plugging) at 600 °C. Reactant stream was 2.7% SiCl<sub>4</sub> and 13% H<sub>2</sub>O in N<sub>2</sub>.

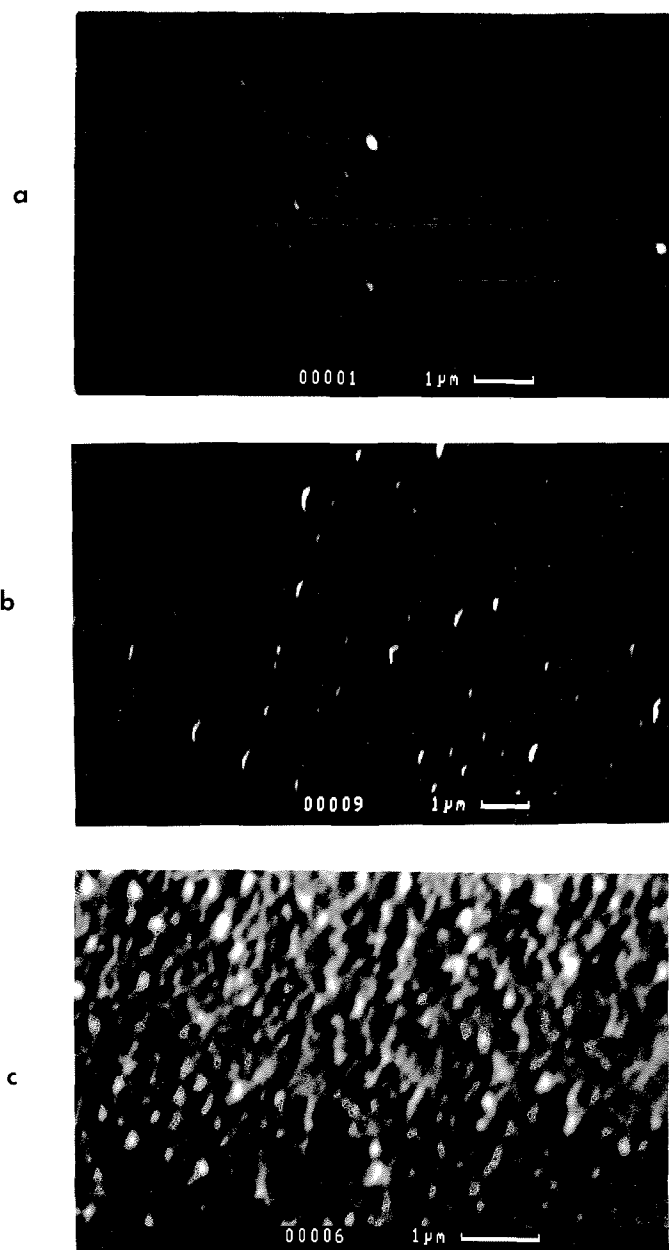


Figure 4.4 SEM micrographs of the bore surface of Vycor tubes. **a**: after 15 minutes of deposition (time to pore plugging); **b**: after 30 minutes of deposition, and **c**: after 50 min of deposition at 600 °C. Reactant stream was 2.7%  $\text{SiCl}_4$  and 13%  $\text{H}_2\text{O}$  in  $\text{N}_2$ .

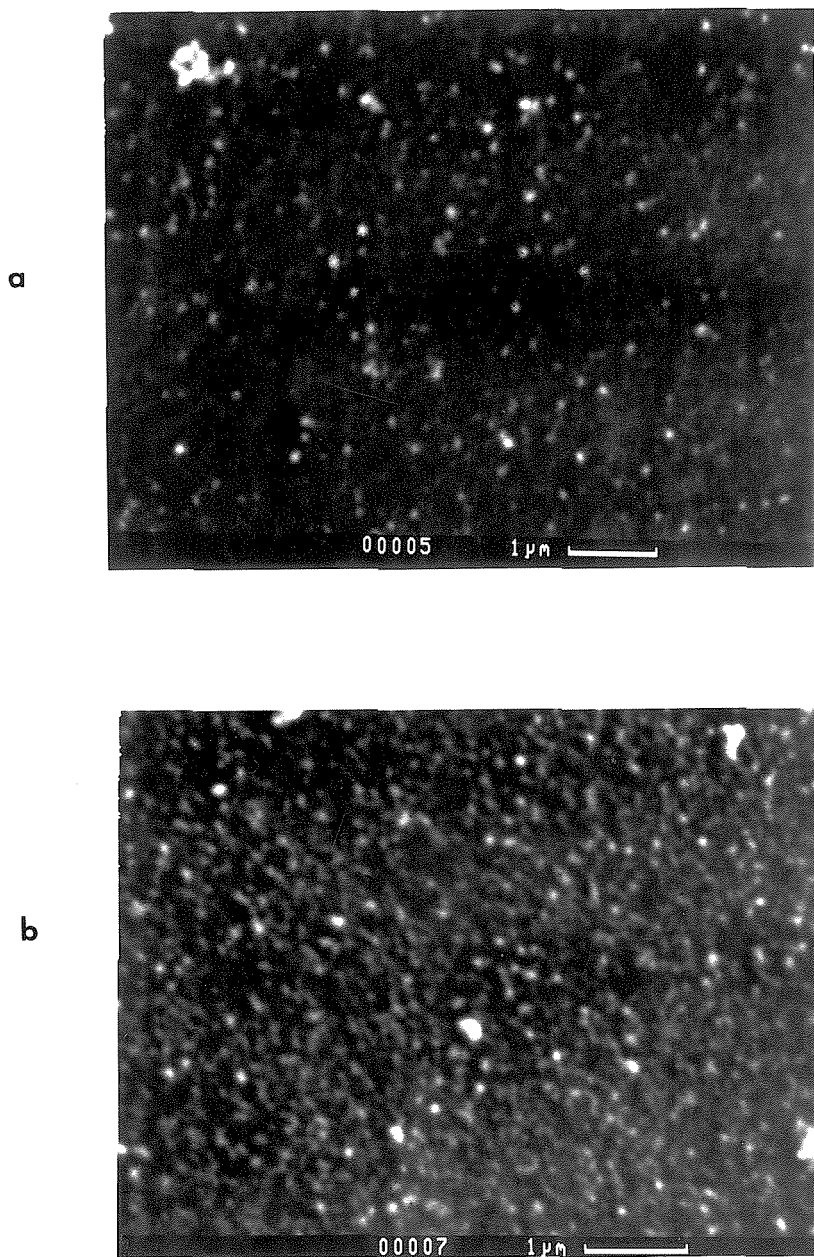


Figure 4.5 SEM microphotograph of the bore of a Vycor tube after OSG deposition at 600 °C with 8.7% SiCl<sub>4</sub> and 13% H<sub>2</sub>O in N<sub>2</sub> immediately after pore plugging. **a**: reactor entrance, **b**: reactor exit.

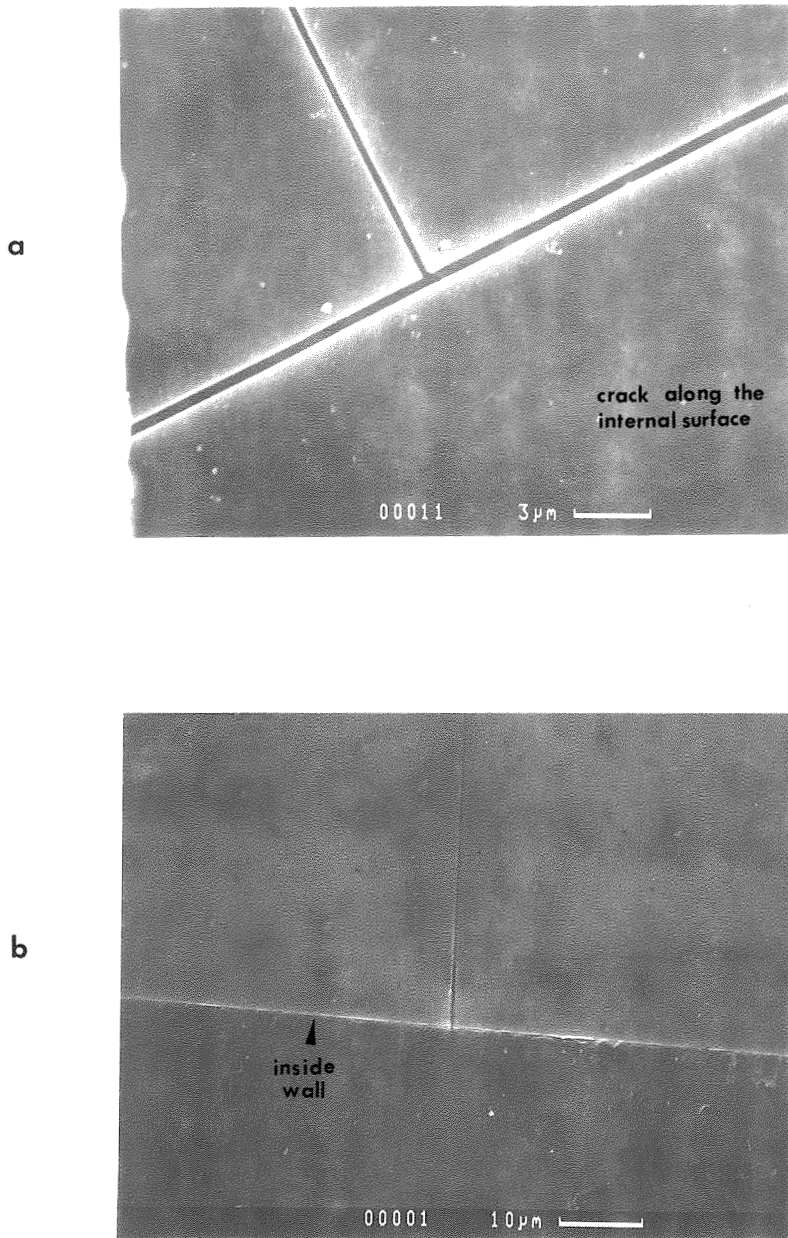


Figure 4.6 Morphology of cracks developed during thermal cycling of membranes with substantial deposition at the outside surface. **a**: planar view, **b**: cross section.

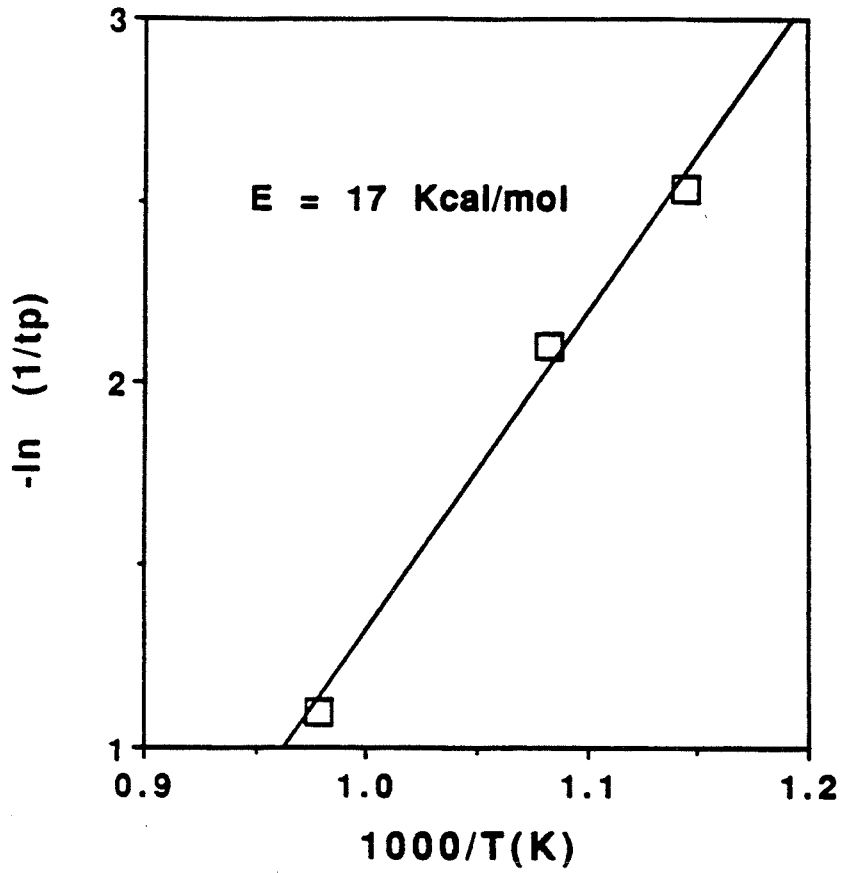


Figure 4.7 Arrhenius plot of  $1/tp$  for OSG deposition using 2.7%  $\text{SiCl}_4$  and 13%  $\text{H}_2\text{O}$ .

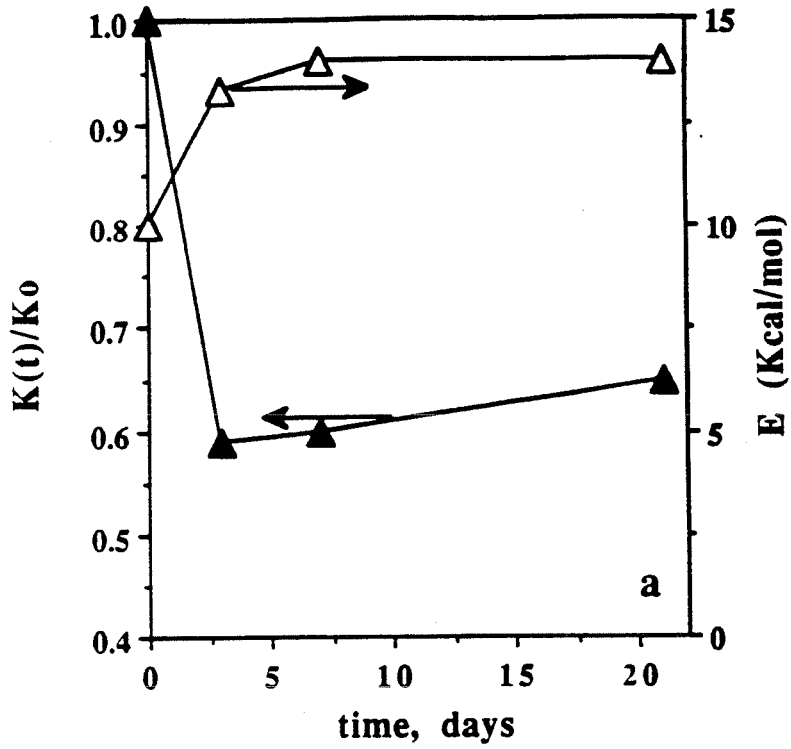


Figure 4.8 Evolution of  $H_2$  permeance at  $600^\circ C$ ,  $K(t)$ , and its activation energy during thermal treatment under dry  $N_2$  at  $550^\circ C$ .  $K_0$ : permeance immediately after pore plugging. Membrane formed by a 5 min deposition at  $750^\circ C$  using 2.7%  $SiCl_4$  and 13%  $H_2O$ .

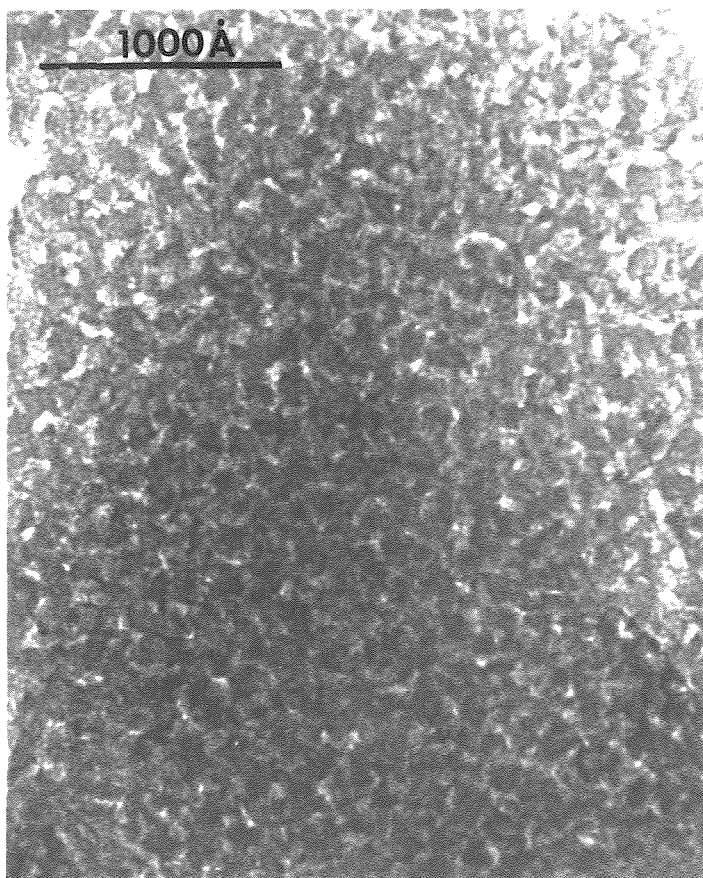


Figure 4.9 Transmission Electron Micrograph of untreated porous Vycor glass.

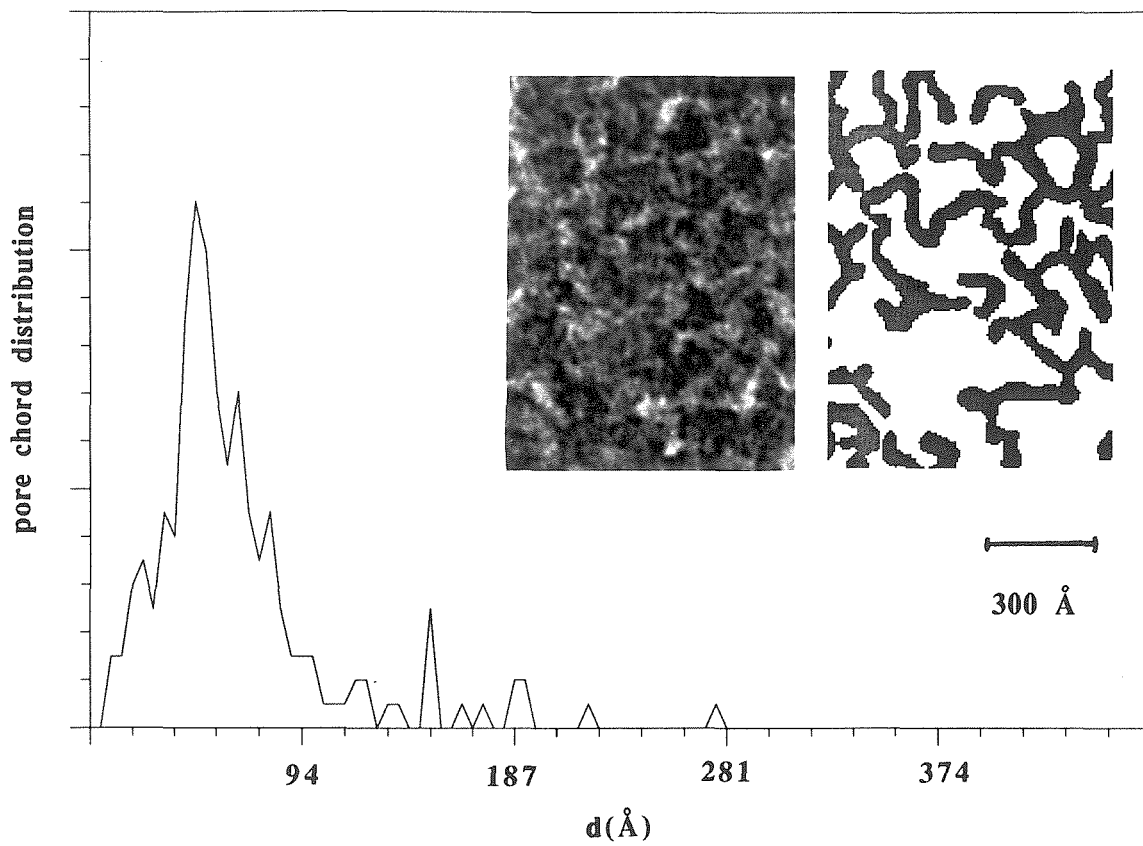


Figure 4.10 Transmission Electron Micrograph of untreated Vycor with the binary image (the pore structure in black) and the pore chord distribution.

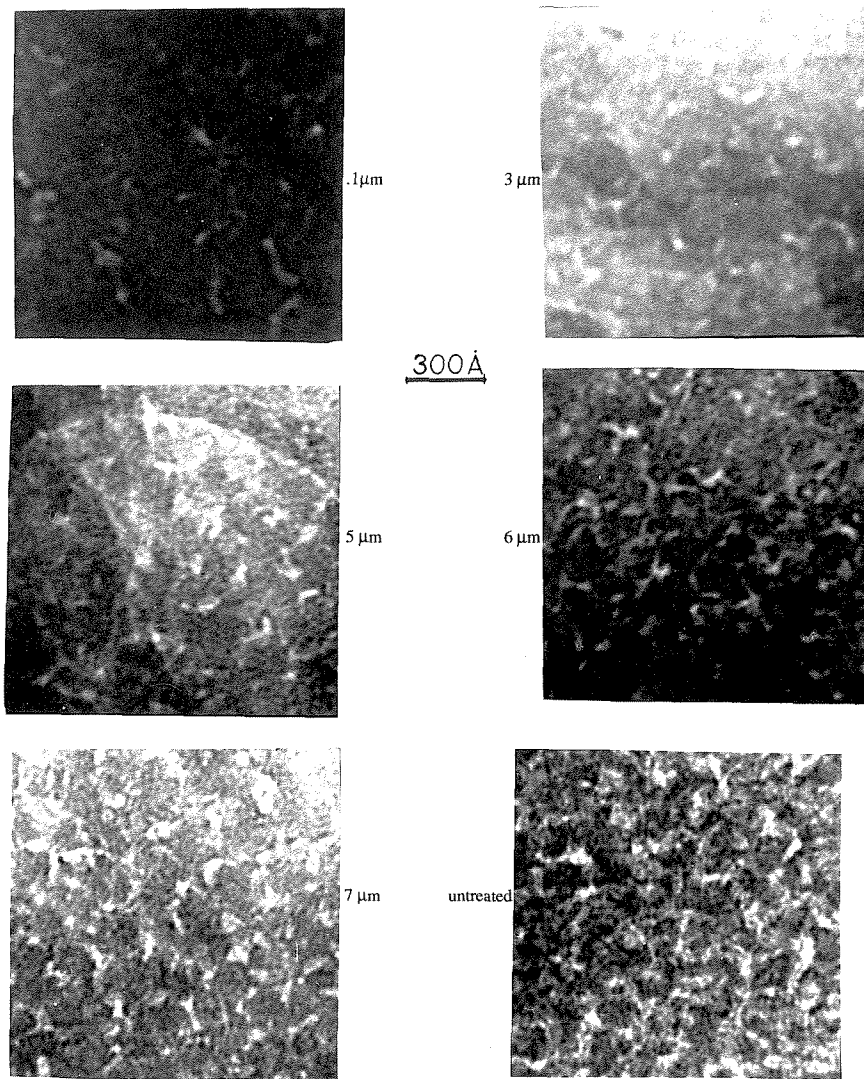


Figure 4.11 Transmission Electron Micrograph of thin sections of the composite membrane at various distances from the side of reactants flow. Deposition conditions:  $T = 600\text{ }^{\circ}\text{C}$ , 13%  $\text{H}_2\text{O}$  and 2.7%  $\text{SiCl}_4$  in  $\text{N}_2$ .

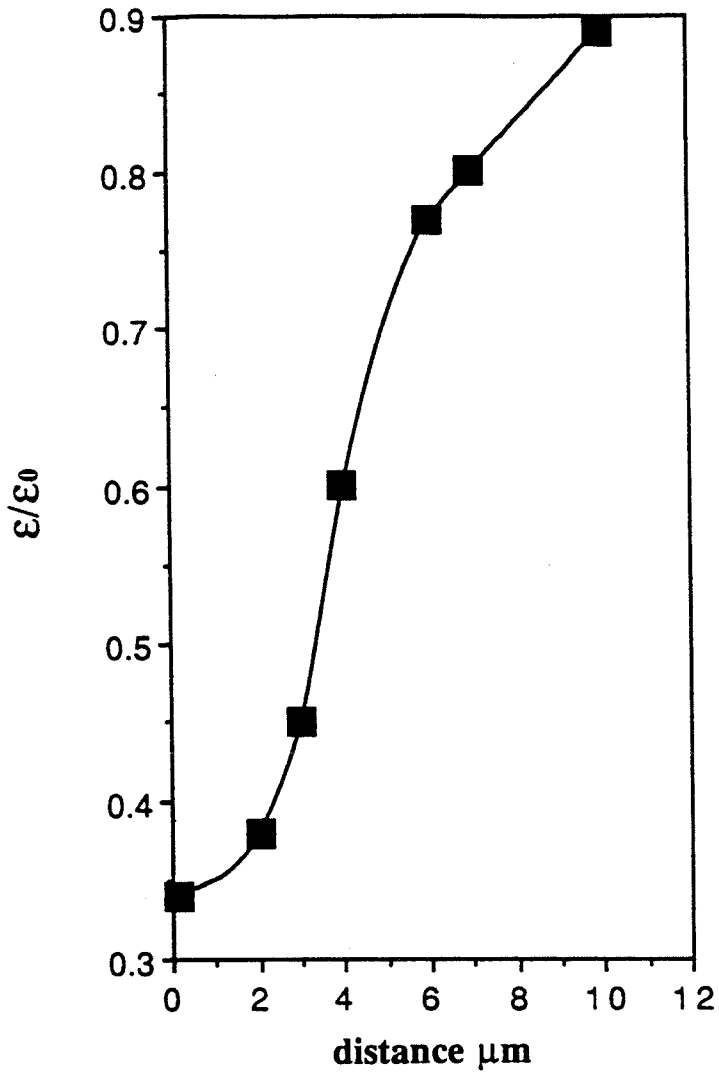


Figure 4.12 Void fraction normalized by initial void fraction,  $\epsilon/\epsilon_0$ , versus distance from the side of reactants flow. Deposition conditions as in Figure 4.11.

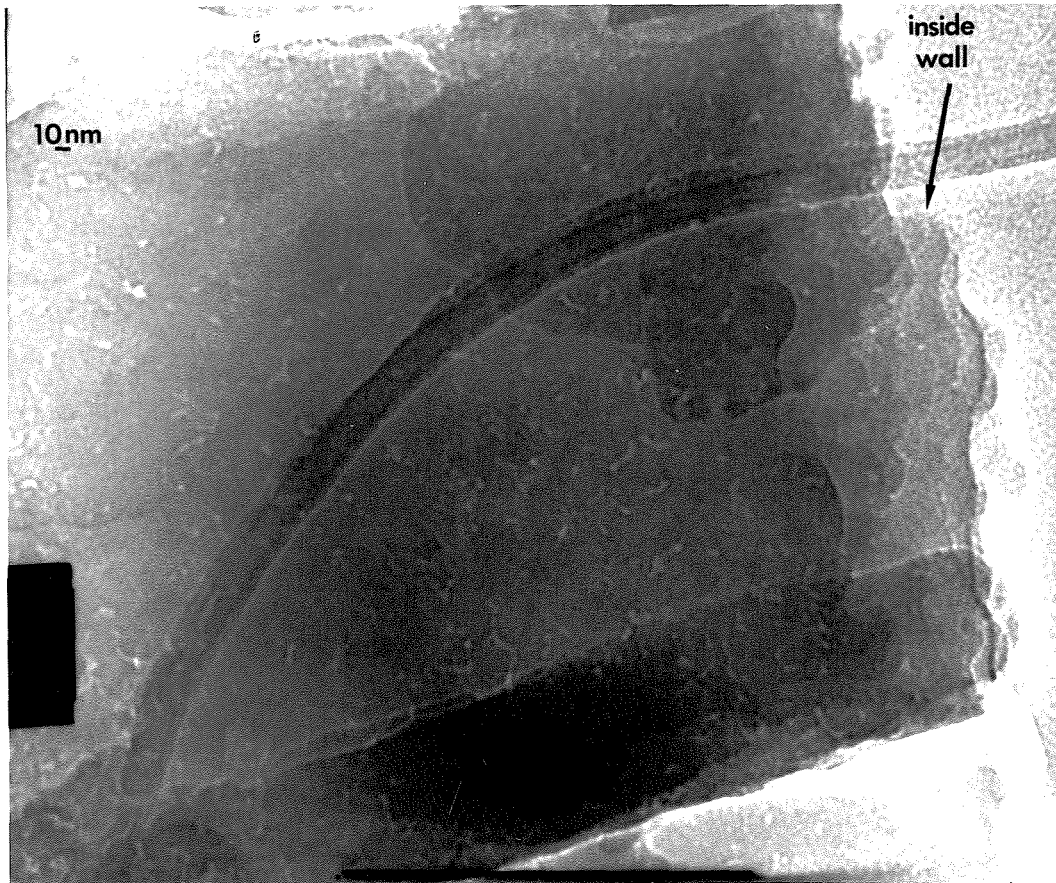


Figure 4.13 Transmission Electron Micrograph of the membrane region close to the side of reactants flow (region of maximum deposition). Deposition conditions as in Figure 4.11.

## **CHAPTER 5**

### **Mathematical Modeling of SiO<sub>2</sub> Deposition in Porous Vycor. Effects of Transient Heterogeneous Kinetics and Pore Connectivity Evolution**

# **Mathematical Modeling of SiO<sub>2</sub> Deposition in Porous Vycor. Effects of Transient Heterogeneous Kinetics and Pore Connectivity Evolution**

**Michael Tsapatsis and George Gavalas**

*Department of Chemical Engineering, California Institute of Technology,  
Pasadena, CA 91125*

## **ABSTRACT**

A mathematical model is developed for SiO<sub>2</sub> deposition in porous Vycor using SiCl<sub>4</sub> hydrolysis. The model describes reaction, diffusion and evolution of the pore structure due to accumulation of the solid product. The deposition reaction is described by transient heterogeneous kinetics in terms of the concentrations of silanol and chloride groups in the product layer as well as the concentrations of the gaseous reactants. Pore structure evolution is modeled by incorporating results of percolation theory. It is shown that for typical deposition conditions the pseudosteady state approximation for surface species could lead to erroneous predictions. Pore connectivity interruption at a nonzero void fraction leads to thinner deposits and shorter deposition times for pore plugging compared to the corresponding ones for an infinitely connected medium.

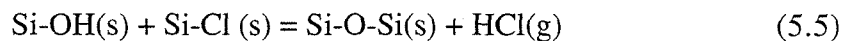
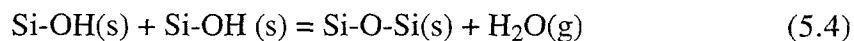
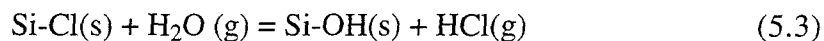
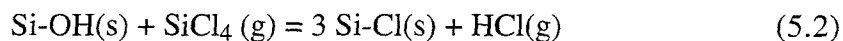
## 5.1 INTRODUCTION

Chemical vapor deposition of thin oxide films inside porous substrates has been used to prepare composite inorganic membranes (1,2,3). Carolan and Michaels (1) have modeled the deposition of yttria stabilized zirconia by chloride hydrolysis describing the kinetics with a phenomenological reaction rate of the form:

$$r = k (C_{\text{chloride}})^a (C_{\text{water}})^b \quad (5.1)$$

In their model the variation of pore size and diffusivity was not taken into account in formulating the transport equations. Lin and Burggraaf (3) developed a more realistic description of the deposition process using a similar rate expression but taking into account the effect of pore restriction on diffusion coefficients. A pseudohomogeneous description in terms of macroscopic diffusivities and tortuosity factors was used to relate the diffusivity with the average pore radius. The effects of pore size distribution on the connectivity of the pore medium were not considered.

We have developed various thin oxide films in porous Vycor for H<sub>2</sub>-permselective membranes (2). Characterization of these deposited oxides has been presented elsewhere (4,5). In reference 4 a model has also been developed describing the deposition process of SiO<sub>2</sub> in porous Vycor in an opposing reactants geometry (ORG) where the chloride and water reactants are introduced from opposing sides of the Vycor substrate. In that model the kinetics were described by the following simplified heterogeneous mechanism:



where Si-OH(s) represents a surface hydroxyl group (silanol), Si-Cl(s) a surface chloride group, and Si-O-Si(s) a siloxane bridge on the solid. In this notation we are counting surface -OH and -Cl groups and not silicon atoms. The model gave predictions of deposit

profiles in qualitative agreement with experimental results. The inability of a phenomenological rate expression in the form of equation (5.1) to describe the deposition process was also noticed. Recent kinetic results from our laboratory provide a more accurate description of deposition kinetics (6). Here we use these results to simplify the reaction scheme and eliminate the uncertainty involved in several kinetic parameters used in the previous model. The emphasis of this report, though, is in the description of the pore structure evolution by use of percolation theory concepts. The motivation for this treatment comes from recent results from transmission electron microscopy (5) and thermogravimetric experiments (6) revealing that at the end of the deposition process a substantial amount of porosity which is open but inaccessible to reactants remains in the region of pore blockage confirming our previous interpretation of electron microprobe analysis data (4). We have also shown that this remaining porosity although trapped can modify significantly the permeabilities of hydrogen and other gases. In that respect the deposition process inside the pores of the substrate is a percolation phenomenon.

Mohanty et al. (7) were the first to describe reaction and transport in a porous medium using percolation concepts by representing the porous medium as a network of interconnected pores which can be blocked at random. More detailed treatments which follow more consistently the evolution of connectivity have also been developed (8).

During deposition a large open pore can be surrounded by smaller pores already plugged. Therefore, the process is characterized by a transition point, called the percolation threshold at which the properties of the porous medium suddenly change because previously connected sample-spanning clusters of open pores suddenly become disconnected.

Sahimi (9) and Sahimi and Tsotsis (10) were the first to point out an important difference between random percolation and deposition processes in their treatment of catalyst deactivation. In random percolation a pore is picked at random and is blocked

regardless of whether or not it can be reached by reactants. In reality isolated pores cannot be reached by reactants and therefore they cannot become blocked. This trapping effect (the term is after Sahimi (9)) was treated elegantly by Yu and Sotirchos (11) in their treatment of gas solid reactions and is also discussed here in the following section. Yu and Sotirchos (11) and Yortsos and Sharma (12) have studied gas solid reactions with pore closure by solving the continuum equations of diffusion and reaction in which the effective diffusivity is estimated using random percolation. This approach although criticized for its validity near the percolation threshold by Arbabi and Sahimi (13) is a significant advancement over the pseudohomogeneous description which also uses continuum equations. Arbabi and Sahimi (13) have developed lattice models which do not rely on continuum equations. Matters regarding continuum vs. network description of the pore structure are fully discussed by Sahimi et al. (14). Here we note only that since the development of the deposit profile takes place mainly when the pore structure is far from its percolation threshold, a continuum description should give good results concerning the evolution of the deposit layer.

Therefore, here we implement the transport model developed by Yu and Sotirchos (11) to examine the effect of connectivity evolution on the deposit profile and on the time of deposition required to block the pores of the Vycor substrate. In order to predict permeation properties one needs the microstructure of the composite material which depends on the details of deposition very close to the percolation threshold where the continuum description used here is not valid.

## 5.2 MODEL FORMULATION

The deposition of silica on Vycor glass can be described by Equations (5.2) to (5.5). The rate constants  $k_1$  to  $k_4$  have been estimated by Kim and Gavalas (6). Here we ignore reactions (5.4) and (5.5) since  $k_3$  and  $k_4$  were found to be very small (6). In the

previous model (4) we used the assumption that all chloride and hydroxyl groups were accessible to the reactants. Here we impose a constraint to the maximum number of OH and Cl groups that are exposed to the reactants.

The balances for OH and Cl groups in a cylindrical pore can be written:

$$\frac{d(S S_{OH})}{dt} = -S k_1 C_1 S_{OH} + S k_2 C_2 S_{Cl} - F S_{OH} \quad (5.6)$$

$$\frac{d(S S_{Cl})}{dt} = 3 S k_1 C_1 S_{OH} - S k_2 C_2 S_{Cl} - F S_{Cl} \quad (5.7)$$

where  $S$  is the surface area of the pore in ( $\text{cm}^2$ ),  $S_{OH}$  and  $S_{Cl}$  are surface concentrations of hydroxyl and chlorine groups in ( $\text{mol} / \text{cm}^2$ ),  $C_1$  and  $C_2$  are gas phase concentrations of chloride and water respectively in ( $\text{mol} / \text{cm}^3$ ), and  $F$  is an unknown function describing the disappearance of sites due to inaccessibility.

The rate of increase of the deposit solid layer thickness is :

$$\frac{dq}{dt} = v k_1 C_1 S_{OH} \quad (5.8)$$

where  $v$  is the molar volume of the deposit in ( $\text{mol}/\text{cm}^3$ ), and  $q$  the deposit thickness in cm.

We assume that at some point after the beginning of the reaction the total accessible reacting groups will reach steady state:

$$\frac{d(S_{Cl} + S_{OH})}{dt} = 0. \quad (5.9)$$

This constraint implies a steady state of total surface sites (OH and Cl),  $S^*_{(OH+Cl)}$ , at some point during the growth of the deposit, while  $S_{OH}$  and  $S_{Cl}$  are allowed to vary as long as the constrain is satisfied. In order for the constraint to be satisfied the function  $F$  should be:

$$F = \frac{2 k_1 C_1 S S_{OH}}{S^*_{(OH+Cl)}} - \frac{dS}{dt} \quad (5.10)$$

Then equations (5.6) and (5.7) become:

$$\frac{d S_{OH}}{dt} = -k_1 C_1 S_{OH} + k_2 C_2 S_{Cl} - \frac{2}{v S^*_{(OH+Cl)}} S_{OH} \frac{dq}{dt} \quad (5.11)$$

$$\frac{d S_{Cl}}{dt} = 3k_1 C_1 S_{OH} - k_2 C_2 S_{Cl} - \frac{2}{v S^*_{(OH+Cl)}} S_{Cl} \frac{dq}{dt} \quad (5.12)$$

The reaction diffusion problem is now formulated as follows:

$$\frac{\partial C_1}{\partial t} - \frac{\partial}{\partial x} \left[ D_1(\epsilon) \frac{\partial C_1}{\partial x} \right] = -k_1 C_1 S S_{OH} \quad (5.13)$$

$$\frac{\partial C_2}{\partial t} - \frac{\partial}{\partial x} \left[ D_2(\epsilon) \frac{\partial C_2}{\partial x} \right] = -k_2 C_2 S S_{Cl} \quad (5.14)$$

$$\frac{\partial S_{OH}}{\partial t} = -k_1 C_1 S_{OH} + k_2 C_2 S_{Cl} - \frac{2}{S^*_{(OH+Cl)}} v k_1 C_1 S_{OH}^2 \quad (5.15)$$

$$\frac{\partial S_{Cl}}{\partial t} = 3k_1 C_1 S_{OH} - k_2 C_2 S_{Cl} - \frac{2}{S^*_{(OH+Cl)}} S_{Cl} v k_1 C_1 S_{OH} \quad (5.16)$$

$$\frac{dq}{dt} = v k_1 C_1 S_{OH} \quad (5.17)$$

The above equations will be made dimensionless using the variables listed in the Nomenclature in order to assess the magnitude of certain terms. The dimensionless equations are:

$$\frac{\partial u_1}{\partial \tau^*} - \frac{\partial}{\partial z} \left( D_1(\epsilon) \frac{\partial u_1}{\partial z} \right) = -\Phi_1^2 u_1 s s_{OH} \quad (5.18)$$

$$\frac{\partial u_2}{\partial \tau^*} - \frac{\partial}{\partial z} \left( D_2(\epsilon) \frac{\partial u_2}{\partial z} \right) = (k_2/k_1) (D_{10}/D_{20}) \Phi_1^2 u_2 s s_{Cl} \quad (5.19)$$

$$\frac{\partial s_{OH}}{\partial \tau^*} = -\psi \Phi_1^2 u_1 s_{OH} + (k_2/k_1) \psi \Phi_1^2 u_2 s_{Cl} - \frac{2S^0_{OH}}{S^*_{(OH+Cl)}} \psi \Phi_1^2 u_1 s_{OH}^2 \quad (5.20)$$

$$\frac{\partial s_{Cl}}{\partial \tau^*} = 3\psi \Phi_1^2 u_1 s_{OH} - (k_2/k_1) \psi \Phi_1^2 u_2 s_{Cl} - \frac{2S^0_{OH}}{S^*_{(OH+Cl)}} \psi \Phi_1^2 u_1 s_{Cl} s_{OH} \quad (5.21)$$

$$\frac{\partial \theta}{\partial \tau^*} = \frac{v S^0_{OH}}{a} \psi \Phi_1^2 u_1 s_{OH} \quad (5.22)$$

The parameter  $\psi$  defined by:

$$\psi = \frac{C_1^0}{S^0 S_{OH}^0} \quad (5.23)$$

is the ratio of gaseous and surface species concentrations and is much smaller than unity for typical deposition conditions. This means that  $s_{Cl}$ ,  $s_{OH}$  and  $\theta$  change on a time scale significantly longer than the time scale for gaseous concentrations changes, suggesting that the quasi-steady state approximation may be applied to the gaseous concentrations. Thus the equations in dimensional form are simplified to:

$$\frac{\partial}{\partial x} \left[ D_1(\epsilon) \frac{\partial C_1}{\partial x} \right] = k_1 C_1 S S_{OH} \quad (5.24)$$

$$\frac{\partial}{\partial x} \left[ D_2(\epsilon) \frac{\partial C_2}{\partial x} \right] = k_2 C_2 S S_{Cl} \quad (5.25)$$

$$\frac{\partial S_{OH}}{\partial t} = -k_1 C_1 S_{OH} + k_2 C_2 S_{Cl} - \frac{2}{S^*_{(OH+Cl)}} v k_1 C_1 S_{OH}^2 \quad (5.26)$$

$$\frac{\partial S_{Cl}}{\partial t} = 3k_1 C_1 S_{OH} - k_2 C_2 S_{Cl} - \frac{2}{S^*_{(OH+Cl)}} S_{Cl} v k_1 C_1 S_{OH} \quad (5.27)$$

$$\frac{dq}{dt} = v k_1 C_1 S_{OH} \quad (5.28)$$

For typical conditions of deposition, the term  $\frac{v S^0_{OH}}{a}$  in Equation (5.22) is of order 0.1 to 1 suggesting that the pseudosteady state approximation for the surface species cannot be used. This is the case here because the typical pore radius,  $a$ , of porous Vycor is about 2 nm. For a deposition on a macroporous substrate, this term will be much smaller than unity justifying the elimination of Equations (5.20) and (5.21). In that case the equations would be:

$$\frac{\partial}{\partial x} \left[ D_1(\epsilon) \frac{\partial C_1}{\partial x} \right] = k_1 C_1 S S_{OH, SS} \quad (5.29)$$

$$\frac{\partial}{\partial x} \left[ D_2(\epsilon) \frac{\partial C_2}{\partial x} \right] = k_2 C_2 S_{Cl,ss} \quad (5.30)$$

$$\frac{dq}{dt} = v k_1 C_1 S_{OH,ss} \quad (5.31)$$

where the steady state concentrations of surface species would be given by:

$$S_{OH,ss} = \frac{-1 - b + (b^2 + 1 + 10b)^{1/2}}{4c} \quad (5.32)$$

$$S_{Cl,ss} = S^*(OH+Cl) - S_{OH,ss} \quad (5.33)$$

$$\text{with } b = \frac{k_2 C_2}{k_1 C_1} \text{ and } c = \frac{4 S_{OH}^0}{S^*(OH+Cl)}$$

The initial and boundary conditions associated with Equations (5.24) through (5.28) are:

$$t = 0 : S_{OH} = S_{OH}^0, S_{Cl} = S_{Cl}^0 \quad (5.34)$$

$$t = 0 : q = q^0 \quad (5.35)$$

$$x = 0 : l_1 (C_{10} - C_1) = -D_1 \frac{\partial C_1}{\partial x} \quad (5.36)$$

$$l_2 C_2 = D_2 \frac{\partial C_2}{\partial x} \quad (5.37)$$

$$x = L : l_2' (C_{20} - C_2) = D_2 \frac{\partial C_2}{\partial x} \quad (5.38)$$

$$l_1' C_1 = -D_1 \frac{\partial C_1}{\partial x} \quad (5.39)$$

where the bulk values of  $C_2$  and  $C_1$  at the chloride side and the water side, respectively, are zero,  $l_1$  and  $l_2$  are the mass transfer coefficients from the chloride side (tube interior), and  $l_1'$  and  $l_2'$  are the same coefficients at the water side (annulus):

$$l_i = Nu D_{i,bulk} / d$$

$$l_i' = Nu' D_{i,bulk} / d'$$

Equations (5.35) through (5.39) are the initial and boundary conditions associated with Equations (5.29) to (5.31) which are based on the pseudosteady state approximation for the surface species. Model predictions in that case do not depend on the initial condition of the substrate surface described by Equation (5.34).

To calculate the accessible surface area and effective diffusion coefficients we follow the developments of Yu and Sotirchos (11). The basic equations are derived as follows.

The porous medium element is represented by a network of bonds and sites with coordination number  $z$ . We assign negligible volume to the sites and a cylindrical capillary of constant length and radius to each bond. Capillary radius and capillary length are distributed randomly and independently of each other. Thus the number fraction of pores of a certain radius is equal to their length fraction. Yu and Sotirchos (11) developed models for both discrete and continuous pore size distribution.

Here a discrete pore size distribution is used consisting of the radii:

$$R_{0\min}=R_{01}<R_{02}<\dots<R_{0N}=R_{0\max} \text{ with lengths } l_{01}, l_{02}, \dots, l_{0N} \text{ and total length } L_0 = \sum_{i=1}^N l_{0i}$$

A pore will be regarded as closed when its radius reaches a specific value  $r^*$ . This value is somewhat arbitrary but can be chosen, for example, as the kinetic radius of  $\text{SiCl}_4$ . It is assumed that the diffusion of both  $\text{SiCl}_4$  and  $\text{H}_2\text{O}$  is negligible in pores of radius  $r^*$ . At any given point in the porous material, let  $t_j$  be the time at which the open accessible pores with initial radius  $R_{0j}$  become closed due to the chemical reaction. Following Yu and Sotirchos we define the discrete length densities  $l_{(i,j)}^a, l_{(i,j)}^n$  where  $l_{(i,j)}^a$  is the length of open and accessible pores of initial radius  $R_{0i}$  immediately after the pores with initial radius  $R_{0j}$  close (at time  $t_j$ ). Similarly  $l_{(i,j)}^n$  is the corresponding length of open inaccessible pores. At time  $t = t_j^+$  one has open and accessible pores of radii

$$R_{0j+1} - (R_{0j} - r^*), R_{0j+2} - (R_{0j} - r^*), \dots, R_{0N} - (R_{0j} - r^*)$$

and lengths

$$l_{(j+1,j)}^a, l_{(j+2,j)}^a, \dots, l_{(N,j)}^a$$

and  $j$  groups of inaccessible pores with radii

$$\{R_{02} - (R_{01} - r^*), \dots, R_{0N} - (R_{01} - r^*)\}, \{R_{03} - (R_{02} - r^*), \dots, R_{0N} - (R_{02} - r^*)\}, \dots,$$

$$\{R_{0j+1} - (R_{0j} - r^*), \dots, R_{0N} - (R_{0j} - r^*)\} \quad \text{and lengths}$$

$$\{l_{(2,1)}^n, \dots, l_{(N,1)}^n\}, \{l_{(3,2)}^n, \dots, l_{(N,2)}^n\}, \dots, \{l_{(j+1,j)}^n, \dots, l_{(N,j)}^n\}$$

At  $t_j$  the open and accessible pores with initial radius  $R_{0j}$  become closed. They have radius  $r^*$  and length  $l_{(j,j-1)}^a$ . The fraction of open pores (accessible and inaccessible)  $X(t_j)$  is then given by

$$X(t_j) = 1 - \frac{\sum_{i=1}^j l_{(j,j-1)}^a}{L_0} \quad (5.39)$$

Percolation theory gives the fraction of open and accessible pores (accessibility function) as a function of the fraction of open pores assuming that the removal of pores is random. In order to use these results we define  $X^*(t_j)$  to be the fraction of open pores if reaction continued to take place on all pores, both accessible and inaccessible. The accessibility function  $f(X^*)$  is then well defined and has been computed for various lattices. We have  $X > X^*$  because an open inaccessible pore would not become closed due to the trapping effect, but it can be removed in random percolation. The important point to be noted is that open and accessible pores in percolation with trapping effect are also open and accessible in random percolation and vice versa. Therefore, the open and accessible pores at  $t_j$  will have lengths:

$$l_{(i,j)}^a = \frac{l_{oi} f(X^*)}{X^*} \quad (5.40)$$

where

$$X^*(t_j) = 1 - \frac{\sum_{i=j+1}^N l_{oi}}{L_o} \quad (5.41)$$

The lengths  $\{ l_{(j+1,j)}^n, \dots, l_{(N,j)}^n \}$  of open inaccessible pores of radii  $\{ R_{oj+1} - (R_{oj} - r^*), \dots, R_{oN} - (R_{oj} - r^*) \}$  that are formed at  $t_j$  are given by

$$l_{(i,j)}^n = l_{(i,j-1)}^a - l_{(i,j)}^a \quad (5.42)$$

Equations (5.40), (5.41) and (5.42) give all the information required for the computation of accessible and inaccessible lengths at each time that a new group of pores becomes closed. At  $t=0$   $l_{(i,0)}^n = 0$  and  $l_{(i,0)}^a = l_{io}$ .

Using the parallel pore formulation the accessible surface area and effective diffusivities are calculated as follows.

$$S = 2 \pi \sum_{i=j+1}^N l_{(i,j)}^a (R_{oi} - q) \quad (5.43)$$

$$D_i = \frac{1}{\tau} \pi A \left( \frac{T}{M_i} \right)^{1/2} \sum_{i=j+1}^N l_{(i,j)}^a (R_{oi} - q)^2 (R_{oi} - q - r^*) \quad (5.44)$$

where  $M_i$  is the molecular weight,  $A$ , the constant in the Knudsen diffusion coefficient and  $\tau$ , the empirical tortuosity.

For simplicity and in keeping with the qualitative nature of the analysis a Bethe-type lattice was chosen to represent the pore network. As has been pointed out before, treating the coordination number,  $z$ , of the Bethe lattice as an adjustable parameter affords sufficient flexibility to mimic the behavior of more realistic networks. Accessibility functions of

various Bethe lattices are given in Figure 5.1. In order to model high percolation thresholds decorated Bethe lattices were used where a bond of the regular Bethe lattice is replaced by a bond graph. The calculations were performed based on the results of Fisher and Essam (15).

### 5.3 NUMERICAL RESULTS AND DISCUSSION

Simulations were performed for SiO<sub>2</sub> deposition in the opposing reactants geometry (ORG) at 400 - 800 °C. The rate constants as estimated in reference (6) are:

$$k_1 = (1.76 \times 10^{15}) e^{-29700/RT} \quad \text{and} \quad k_2 = (1.09 \times 10^{11}) e^{-19800/RT} .$$

The surface concentration of silanol groups (-OH) on Vycor glass after heating at 600 °C was estimated as 1.5 OH/nm<sup>2</sup> in reference (6). Other reports, however, give values as high as 5 OH/nm<sup>2</sup>. The initial -OH concentration depends also on the time of dehydroxylation. In the simulations we used values between 1.5 and 3 -OH/nm<sup>2</sup>. The Nusselt number was estimated around 4 as in reference (4). The kinetic parameter  $S^*_{(OH+Cl)}$  was varied between 5 and 10 sites/nm<sup>2</sup>. Due to the lack of sufficient experimental data refinement of this parameter was not attempted. Permeation data suggest that the deposited material is highly defective immediately after deposition; therefore, values for the deposit density were varied between 1.5 and 1.8 g/cm<sup>3</sup> considerably lower than typical SiO<sub>2</sub> densities of 2.1 g/cm<sup>3</sup>.

The time evolution, Equations (5.26) to (5.28), were integrated by the fourth-order Runge-Kutta routine. Each evaluation of the right hand side of these equations required solution of the linear boundary value problem (5.24) - (5.25), (5.36)-(5.39). This solution was carried out by spatial discretization (finite differences) and solution of the resulting linear system by Gaussian elimination.

Diffusivities and accessible surface area are needed for each deposition time and are calculated by the following procedure. It is first noticed that the percolation problem can be solved independently of Equations (5.24)-(5.28). A table is thus created giving local diffusivities and accessible surface areas as functions of the deposit thickness,  $q$ , for various lattices by use of Equations (5.40)-(5.44). For these calculations the pore size distribution of Vycor, estimated from gas adsorption data by the manufacturer (Corning Inc.) was discretized in increments of 1 Å. The tabulated values of diffusivities and accessible surface area are retrieved during the simulation given the local value of  $q$  at a particular time. Each run was terminated when interruption of connectivity took place at some point in the substrate. Simulations were performed for infinitely connected networks ( $z=\infty$ ), *regular* Bethe lattices with coordination number 3 ( $z=3$ ) and *decorated* Bethe lattices with coordination number 3 where a bond of the regular Bethe lattice is replaced by a bond graph consisting of  $n$  bonds in series ( $z=3, d=n$ ).

Figure 5.2 shows calculated dimensionless flux,  $F$ , of any inert gas versus time of deposition at 800 °C using 30% chloride and 10% water. Two different deposit densities were used in the simulations,  $v= 1.5$  and  $1.8 \text{ g/cm}^3$ , corresponding to deposit molar volumes of 40 and  $33 \text{ cm}^3/\text{mol}$  respectively. The influence of pore structure connectivity is demonstrated by including results for infinitely connected network  $z=\infty$  and a Bethe lattice ( $z=3, d=4$ ) for each deposit density. As expected the lower density deposit leads to faster pore constriction and pore plugging. Faster pore plugging takes place also when the finite connectivity of the pore structure is taken into account.

Figure 5.3a shows the calculated deposit densities normalized by the substrate density ( $R$ : deposit over substrate weight ratio) for  $z=\infty$  and ( $z=3, d=4$ ) using  $v=40 \text{ cm}^3/\text{mol}$ . The normalized density is smaller for the decorated Bethe lattice due to pore plugging at a non zero void fraction. Moreover, the deposit around the region of maximum deposition is thinner. Pore connectivity effects manifest themselves during the final stages

of deposition and thus no differences in the profiles are observed in the deposit profile tail which is far from the percolation threshold. Using the lower molar volume,  $v=33 \text{ cm}^3/\text{mol}$  yields a qualitatively similar profile but with a higher peak, as expected (Figure 5.3b). Previous measurements have given the maximum deposit density (5). The experimental density can be matched by many combinations of lattices and  $v$ . In order to meaningfully compare experimentally determined profiles with simulation, these two parameters should be independently estimated.

Figure 5.4 shows the influence of the parameter  $S^*_{(\text{OH}+\text{Cl})}$  on the deposit profiles. Two values were used corresponding to a maximum of 5 and 10 accessible surface sites per  $\text{nm}^2$ . As  $S^*_{(\text{OH}+\text{Cl})}$  increases pore plugging takes place faster and the deposit profile moves towards the chloride side.

Figure 5.5 shows the influence of the initial concentration of OH species on the final deposit profile. A lower initial OH concentration leads to faster pore plugging. This result demonstrates the complicated interplay of transport and transient kinetics during deposition. It can be understood by considering the role of initial OH species in consuming gaseous chloride inside the substrate in the absence of water. That reaction leads to the formation of the sublayer that consists the deposit tail. As the initial number of OH species is decreased this retardation effect is less pronounced and the chloride diffuses faster inside the substrate decreasing the overall deposition time. A pseudosteady state approximation for the surface species cannot predict such behavior. Equations (5.29)-(5.33) although physically more meaningful than the empirical Equation (5.1), do not include any information regarding the initial concentration of surface species on the substrate. To demonstrate the importance of transient kinetics further, a more extreme case was examined. Before the ORG deposition the substrate surface was pretreated by reaction with  $\text{SiCl}_4$  in the absence of water so that all OH groups were replaced with Cl groups according to reaction (5.2). The deposition was then started. The resulting profile shown

in Figure 5.6 is considerably different than the profile calculated for deposition without prior chlorination. Qualitatively similar behavior has been observed experimentally as reported in reference (4).

Finally the influence of temperature of deposition is shown in Figure 5.7. Lower temperatures decrease the reaction rate and thicken the reaction region. At 400 °C the deposit is spread over the whole thickness of the substrate. Temperatures higher than 600 °C are needed for the formation of a thin deposit layer.

## 5.4 CONCLUSIONS

A model has been developed for the deposition of silica in porous Vycor using  $\text{SiCl}_4$  hydrolysis in an opposing reactants geometry. A deposition mechanism suggested from previous studies has been adopted involving reaction of the gaseous chloride with silanol groups on the surface and reaction of water vapor with chloride groups of the surface. Inaccessibility of surface groups due to deposit growth has been introduced into the model by assuming a maximum number of surface species per surface area exposed to gas reactants. The transient kinetics associated with these reactions were introduced into a continuum model describing diffusion and pore closure making use of percolation theory concepts. It was found that for typical deposition conditions the connectivity evolution of the microporous substrate influences the time for pore plugging and the deposit thickness at the region of maximum deposition but not the position of the deposit. It was also shown that in order to describe the heterogeneous deposition reaction in the microporous Vycor substrate, it is necessary to use the transient kinetics. The pseudosteady state approximation for surface species is not valid.

**ACKNOWLEDGMENTS**

The authors appreciate funding of this project by the Department of Energy under the University Coal Research Program, Grant DE-FG22-92PC92525. Professor Sotirchos provided helpful suggestions.

## REFERENCES

1. Carolan, M. and J. N. Michaels, "Chemical Vapor Deposition of Yttria Stabilized Zirconia on Porous Substrates," *Solid State Ionics* **25**, 207 (1987)
2. Tsapatsis, M., S. Kim, S.W. Nam and G.R. Gavalas, "Synthesis of Hydrogen Permselective SiO<sub>2</sub>, TiO<sub>2</sub>, Al<sub>2</sub>O<sub>3</sub> and B<sub>2</sub>O<sub>3</sub> Membranes from the Chloride Precursors," *I&EC Research* **30**, 2152-2159 (1991) .
3. Lin, Y.S. and A.J. Burggraaf, "Modeling and Analysis of CVD Processes in Porous Media for Ceramic Composite Fabrication," *Chem. Eng. Sci.* **46**, 3067-3080 (1992)
4. Tsapatsis, M. and G.R. Gavalas, "A Kinetic Model for Membrane Formation by CVD of SiO<sub>2</sub> and Al<sub>2</sub>O<sub>3</sub>," *AIChE Journal* **38**, 847-856 (1992).
5. Tsapatsis, M. and G.R Gavalas, "Structure and Aging Characteristics of H<sub>2</sub>-permselective SiO<sub>2</sub>-Vycor Membranes," (accepted for publication *Journal of Membrane Science*).
6. Kim, S.J. and G. R. Gavalas, "Thermogravimetric study of the reactions of chlorosilanes with the surface of Vycor glass," (accepted for publication *J. of Colloid and Interface Sci.*).
7. Mohanty, K.K., J.M. Ottino and H.T. Davis, "Reaction and Transport in Disordered Media: Introduction of Percolation Concepts," *Chem. Eng. Sci.* **37**, 905-924 (1982).

8. Mace, O. and J. Wei, "Diffusion in Random Particle Models for Hydrodemetalation Catalysts," *Ind. Eng. Chem. Res.* **30**, 909-918 (1991).
9. Sahimi, M., "Fractal dimension in a percolation model of fluid displacement," *Phys. Rev. Lett.* **55**, 1698 (1985).
10. Sahimi, M. and T.T. Tsotsis, "A Percolation Model of Catalyst Deactivation by Site Coverage and Pore Blockage," *J. Catal.* **96**, 552-562 (1985).
11. Yu, H.-C. and S.V. Sotirchos, "A Generalized Pore Model for Gas-Solid Reactions Exhibiting Pore Closure," *AIChE J.* **33** (3), 382-393 (1987).
12. Yortsos, Y.C. and M. Sharma, "Application of Percolation Theory to Noncatalytic Gas-Solid Reactions," *AIChE J.* **32** (1), 46-55 (1986).
13. Arbabi, S. and M. Sahimi, "Computer Simulations of Catalyst Deactivation-I. Model Formulation and Validation," *Chem. Eng. Sci.* **46**, 1739-1747 (1991).
14. Sahimi, M., G.R. Gavalas and T.T. Tsotsis, "Statistical and Continuum Models of Fluid-Solid Reactions in Porous Media," *Chem. Eng. Sci.* **45**, 1443-1502 (1990).
15. Fisher, M.E. and J.W. Essam, "Some Cluster Size and Percolation Problems," *Journal of Mathematical Physics* **2** (4), 609-619 (1961).

## NOTATION

$a$ :	characteristic pore radius, cm
$C_1$ :	gas phase chloride concentration, mol/cm <sup>3</sup> pore volume
$C_2$ :	gas phase water concentration, mol/cm <sup>3</sup> pore volume
$C_i^0$ :	chloride or water concentration at the bubbler, mol/cm <sup>3</sup>
$d$ :	outside diameter of Vycor tube, cm
$d'$ :	equivalent hydraulic diameter of outside flow, cm
$f(X^*)$ :	accessibility function
$F$ :	dimensionless inert flux
$D_i$ :	Knudsen diffusivity of species $i$ , cm <sup>2</sup> /min
$D_{i,bulk}$ :	binary diffusivity of species $i$ , cm <sup>2</sup> /min
$D_i$ :	dimensionless diffusivity
$k_1, k_2$ :	reaction rate constants, cm <sup>3</sup> pore volume/min-mol
$L$ :	thickness of substrate Vycor tube, cm
$l_{(i,j)}^a$ :	length of open and accessible pores with initial radius $R_{oi}$ when pores with initial radius $R_{oj}$ close, cm/cm <sup>3</sup>
$l_{(i,j)}^n$ :	length of open inaccessible pores with initial radius $R_{oi}$ when pores with initial radius $R_{oj}$ close, cm/cm <sup>3</sup>
$L_o$ :	total initial length of pores, cm/cm <sup>3</sup>
$l_{oi}$ :	initial length of pores with initial radius $R_{oi}$ , cm/cm <sup>3</sup>
$M_i$ :	molecular weight of species $i$
$Nu$ :	Nusselt number
$q$ :	thickness of deposit layer perpendicular to pore wall, cm
$q_o$ :	initial thickness of deposit layer perpendicular to pore wall, cm
$R$ :	gas constant
$\mathbf{R}$ :	normalized deposit density

$r^*$ :	L-J radius of $\text{SiCl}_4$ , cm
$R_{oi}$ :	initial radius of pores of group i, cm
$S$ :	accessible surface area, $\text{cm}^2/\text{cm}^3$
$S_{\text{OH}}$ :	-OH concentration, $\text{mol}/\text{cm}^2$ or sites/ $\text{nm}^2$
$S_{\text{Cl}}$ :	-Cl concentration, $\text{mol}/\text{cm}^2$ or sites/ $\text{nm}^2$
$S_{\text{OH,ss}}$ :	steady state -OH concentration, $\text{mol}/\text{cm}^2$ or sites/ $\text{nm}^2$
$S_{\text{Cl,ss}}$ :	steady state -OH concentration, $\text{mol}/\text{cm}^2$ or sites/ $\text{nm}^2$
$S_{\text{OH}}^0, S_{\text{Cl}}^0$ :	initial concentrations of OH and Cl, $\text{mol}/\text{cm}^2$ or sites/ $\text{nm}^2$
$S^*(\text{OH+Cl})$ :	maximum number of surface species accessible to gas reactants, $\text{mol}/\text{cm}^2$ or sites/ $\text{nm}^2$
$s$ :	dimensionless accessible surface area
$s_{\text{OH}}$ :	dimensionless -OH concentration
$s_{\text{Cl}}$ :	dimensionless -Cl concentration
$T$ :	temperature, K
$u_j$ :	dimensionless gas concentration
$v$ :	molar volume of deposit, $\text{cm}^3/\text{mole}$
$x$ :	distance measured from inside wall of substrate tube, cm
$X$ :	fraction of open pores
$X^*$ :	fraction of open pores for random percolation
$z$ :	dimensionless distance measured from inside wall of substrate tube (chloride side)

### Greek letters

$\epsilon_0$ :	initial void fraction of substrate
$\epsilon$ :	void fraction of substrate
$\theta$ :	dimensionless deposit thickness
$\tau$ :	tortuosity

- $\tau^*$ : dimensionless time
- $\Phi_1$ : Thiele modulus
- $\psi$ : ratio of gaseous to surface species concentration

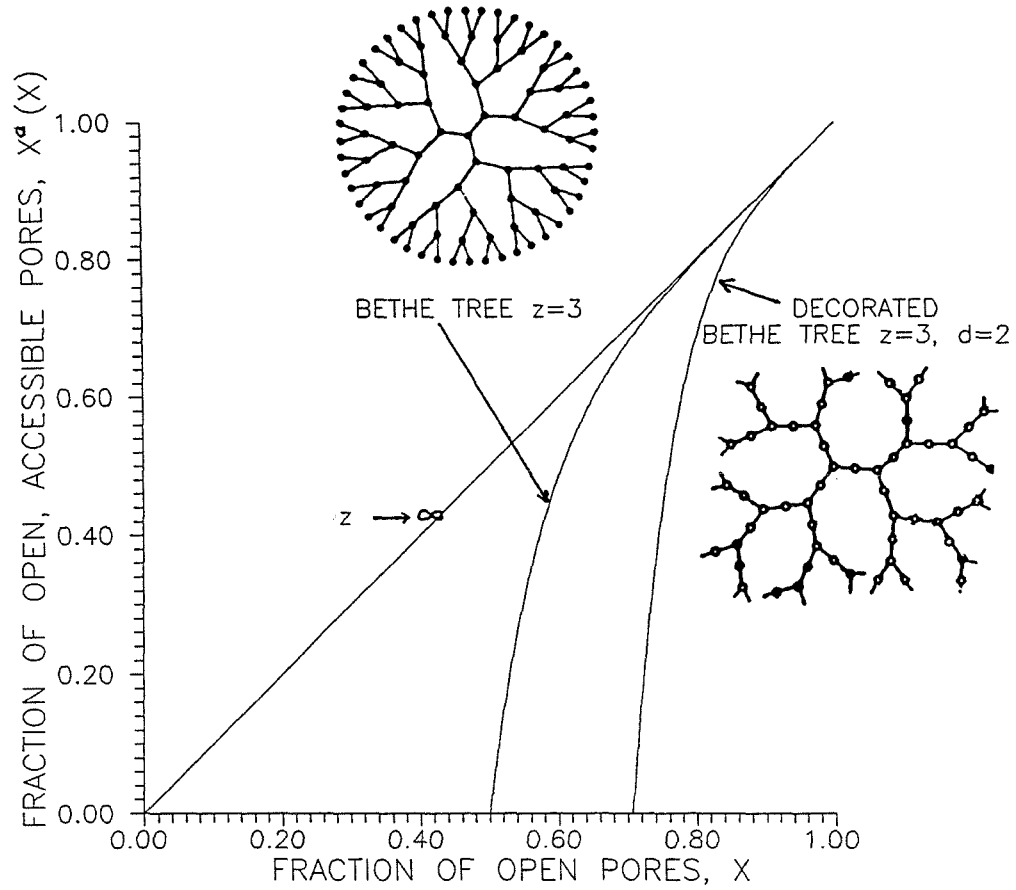


Figure 5.1 Accessibility functions of various lattices

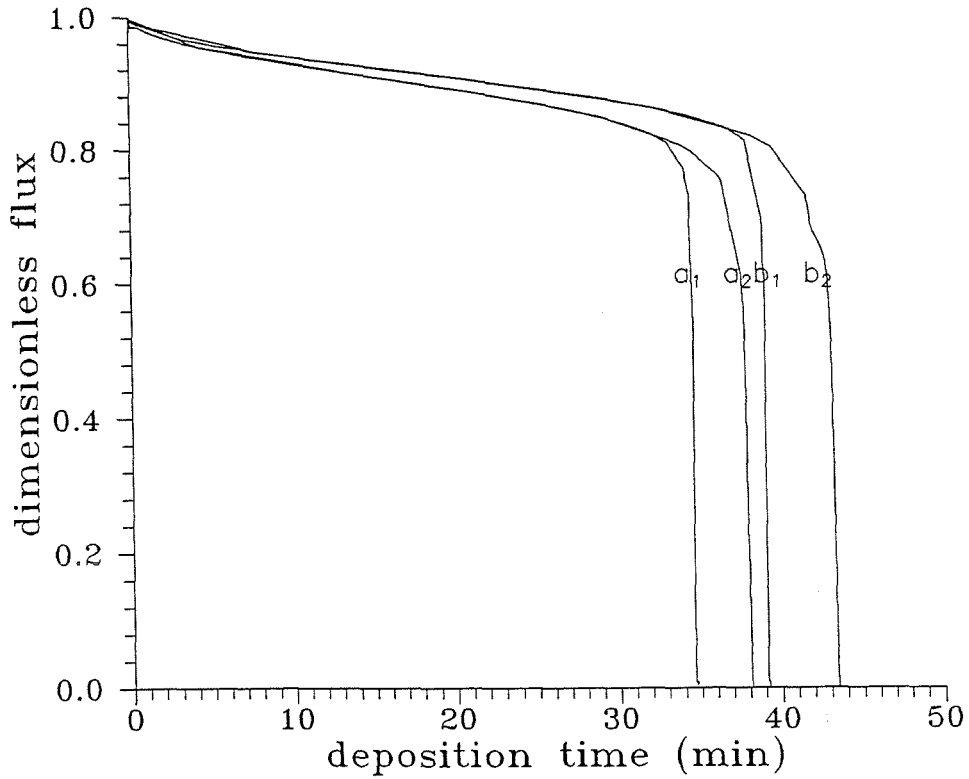


Figure 5.2 Evolution of the normalized permeance for ORG deposition at 800 °C, using 10% water and 30% chloride. Parameters used:  $v = 40 \text{ cm}^3/\text{mol}$  ( $\mathbf{a_1, a_2}$ ) and  $33 \text{ cm}^3/\text{mol}$  ( $\mathbf{b_1, b_2}$ ),  $S_{\text{OH}}^0 = 3/\text{nm}^2$ ,  $S^*_{(\text{OH}+\text{Cl})} = 5/\text{nm}^2$ . Lattices used:  $z = \infty$  ( $\mathbf{a_2, b_2}$ ), and decorated Bethe lattice ( $z=3, d=4$ ) ( $\mathbf{a_1, b_1}$ ).

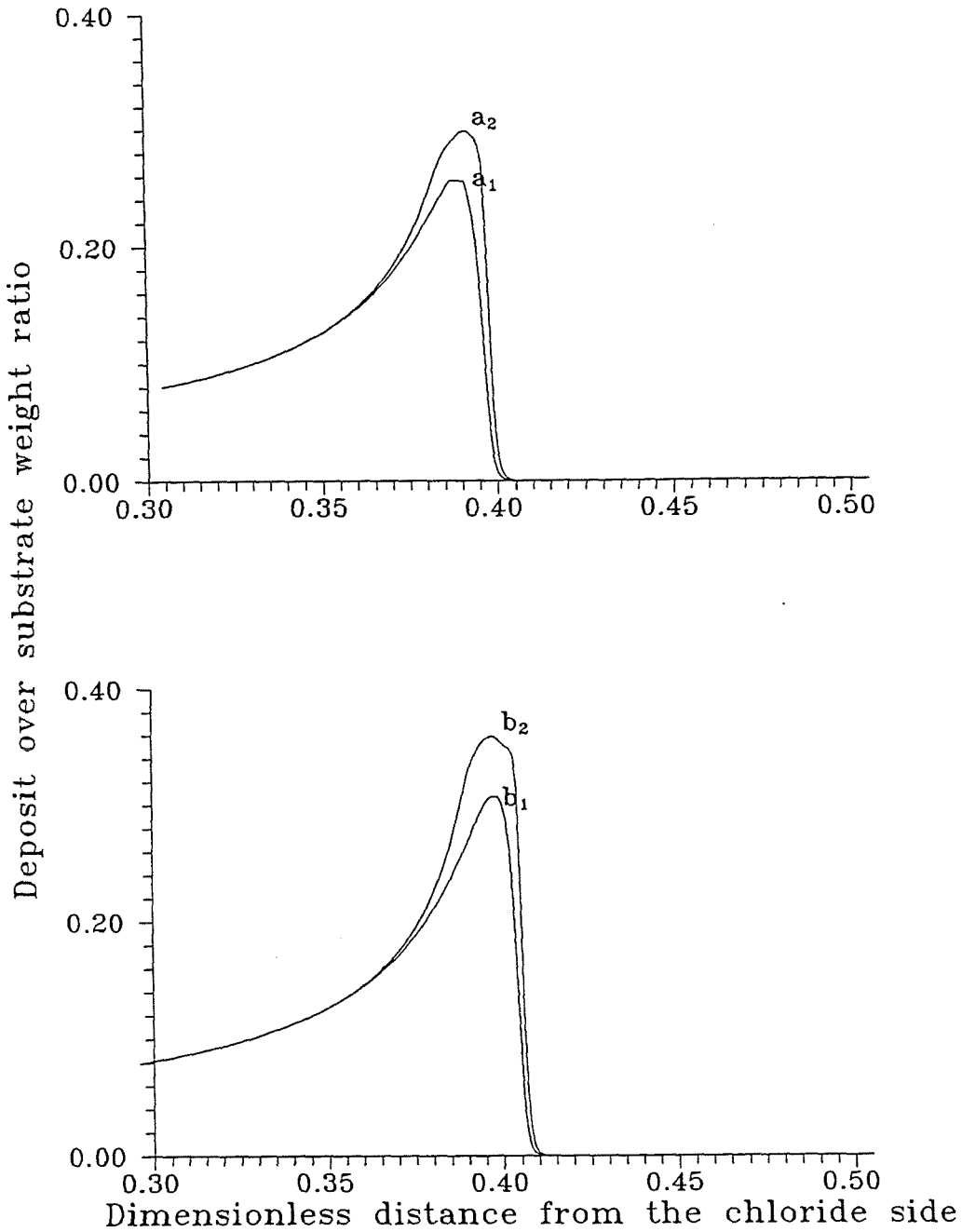


Figure 5.3 Deposit profiles at the end of deposition from the simulations of Figure 5.2.  $a_1$ :( $z=3, d=4$ ),  $v=40\text{cm}^3/\text{mol}$ ;  $a_2$ :( $z=\infty$ ),  $v=40\text{cm}^3/\text{mol}$ ;  $b_1$ :( $z=3, d=4$ ),  $v=33\text{cm}^3/\text{mol}$ ;  $b_2$ :( $z=\infty$ ),  $v=33\text{cm}^3/\text{mol}$ .

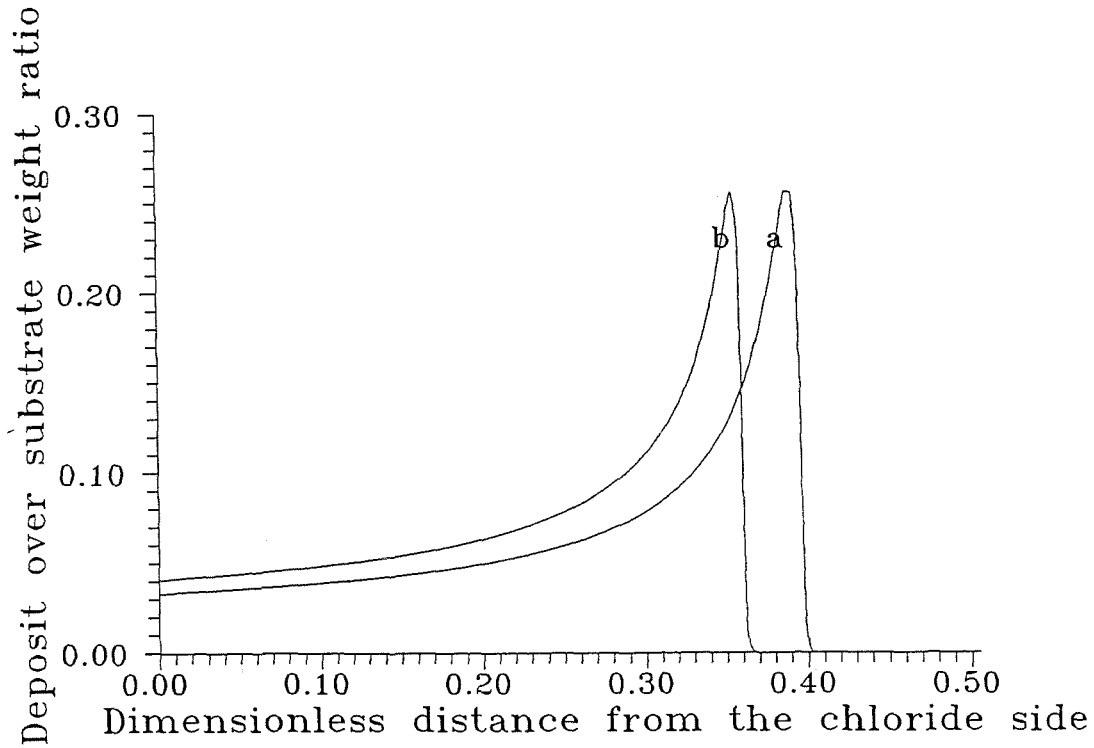


Figure 5.4 Influence of the kinetic parameter  $S^*_{(\text{OH}+\text{Cl})}$  on the deposit profiles. **a**:  $S^*_{(\text{OH}+\text{Cl})}=5/\text{nm}^2$  (time for pore plugging=34.5min), **b**:  $S^*_{(\text{OH}+\text{Cl})}=10/\text{nm}^2$  (time for pore plugging=32.5min), using  $v=40\text{cm}^3/\text{mol}$  and a ( $z=3, d=4$ ) lattice. Other parameters as in Figure 5.2.

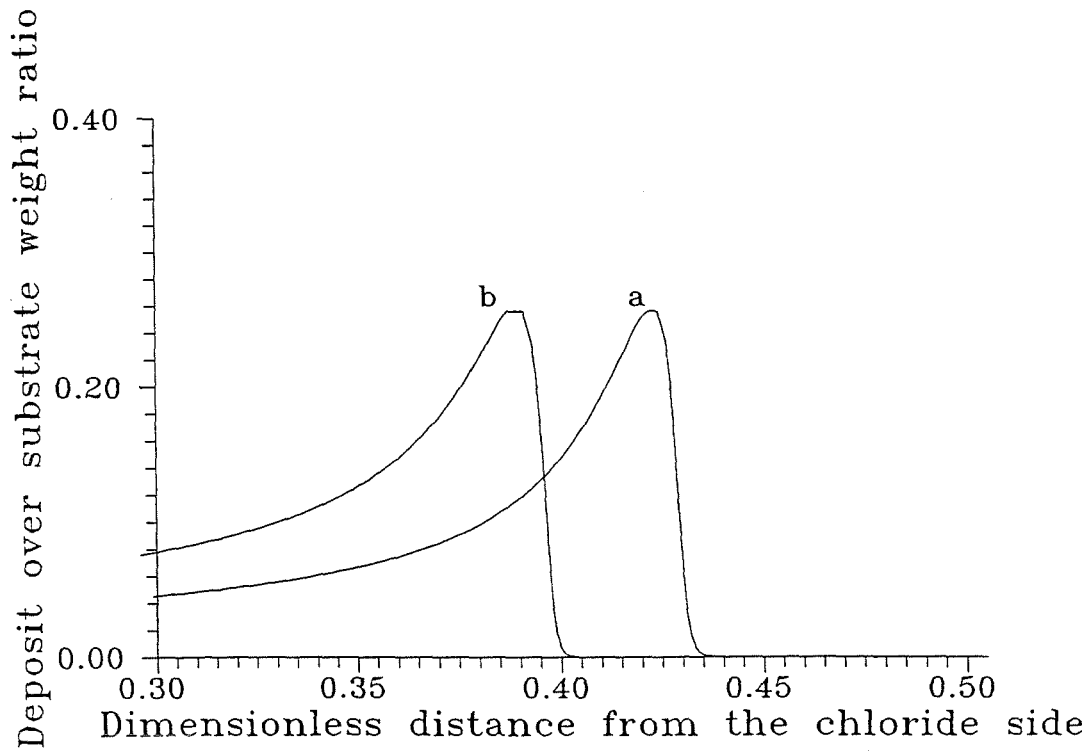


Figure 5.5 Influence of initial OH concentration on the deposit profiles. **a**:  $1.5\text{OH}/\text{nm}^2$  (time for pore plugging=29min), **b**:  $3\text{OH}/\text{nm}^2$  (time for pore plugging=34.5min).  $S^*_{(\text{OH}+\text{Cl})}=5/\text{nm}^2$ . Other parameters as in Figure 5.4.

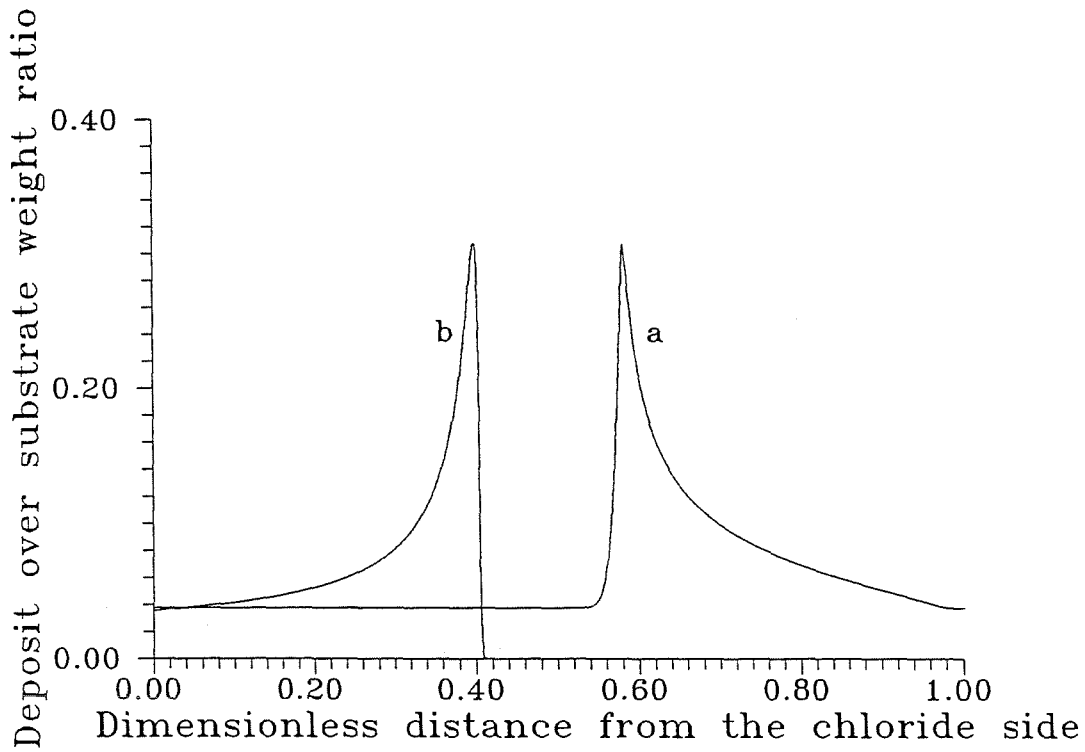


Figure 5.6 a: deposit profile at the end of deposition after dehydroxylation (time for pore plugging=66.5min), b: corresponding profile at the end of deposition without prior dehydroxylation (time for pore plugging=39min).  $S^*_{(OH+Cl)}=5/\text{nm}^2$ ,  $v=33\text{cm}^3/\text{mol}$ . Other parameters as in Figure 5.4.

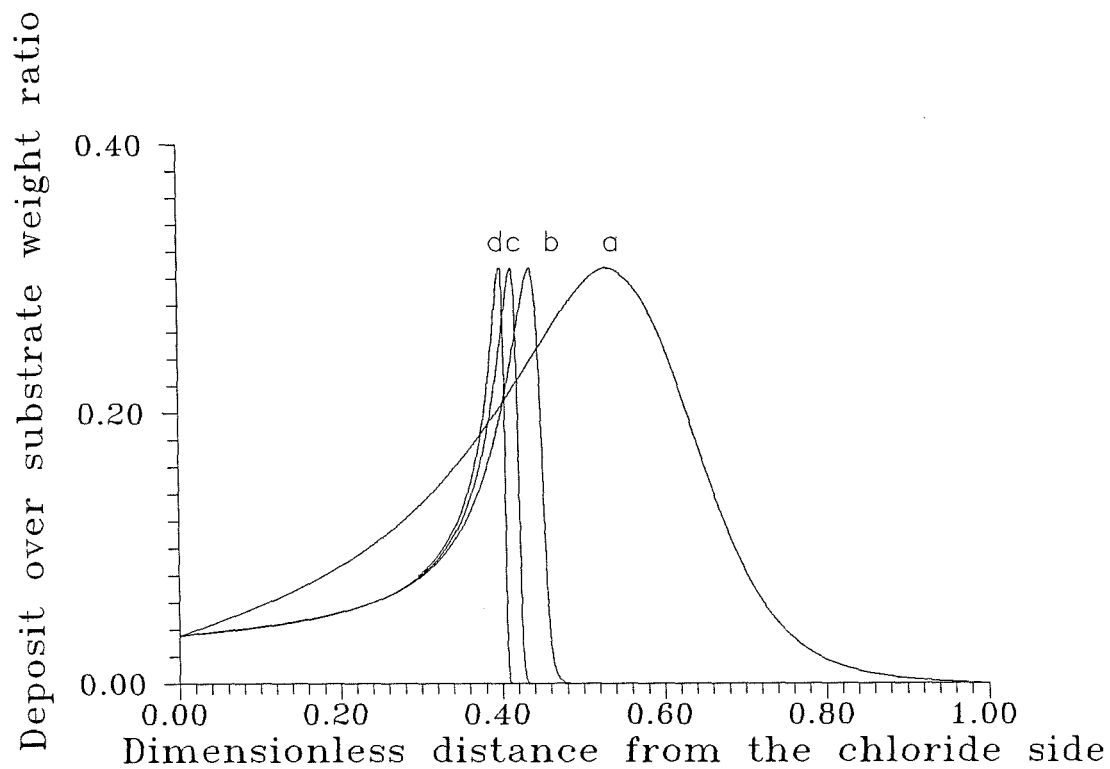


Figure 5.7 Influence of deposition temperature on deposit profiles. **a**:400°C, **b**:600 °C, **c**:700 °C, **d**:800 °C.  $3\text{OH}/\text{nm}^2$ . Other parameters as in Figure 5.6.

## **CHAPTER 6**

### **A Study on the Formation of Supported Zeolite NaA Films from a Clear Solution**

## **A Study on the Formation of Supported Zeolite NaA Films from a Clear Solution**

**Michael Tsapatsis, George Gavalas and Mark E. Davis**

*Department of Chemical Engineering, California Institute of Technology,*

*Pasadena, CA 91125*

### **ABSTRACT**

The growth of zeolite NaA films on various inorganic substrates from a clear solution with composition  $10 \text{ Na}_2\text{O}-0.2 \text{ Al}_2\text{O}_3-1\text{SiO}_2-200 \text{ H}_2\text{O}$  was followed by XRD, SEM and TEM. Deposition geometries and conditions are identified for the development of uniform polycrystalline thin ( $<5\mu\text{m}$ ) films consisting of intergrown crystals of zeolite NaA on porous and nonporous  $\text{Al}_2\text{O}_3$  disks. The films exhibit high crystallinity good adhesion to the substrate and thermal stability. The deposition technique demonstrates potential for developing molecular sieve membranes.

## 6.1 INTRODUCTION

The industrial interest in zeolite thin films is based on the unique molecular sieving properties of zeolites which confer upon them potential uses as dense layers of asymmetric inorganic membranes for separations and catalysis. Other more advanced applications of molecular sieves for electronic materials (1), sensors (2) and photocatalytic applications (3) have been proposed. For the realization of such devices, versatile methods of preparing thin zeolite films on various substrates are required.

Since the first report on inorganic composite zeolite membranes (4), considerable research has been devoted exploring various approaches for the preparation and characterization of zeolite films on inorganic substrates (5,6 and references therein). We have previously reported the preparation and characterization of H<sub>2</sub>-permselective SiO<sub>2</sub>-Vycor composite membranes (7,8,9). In search of other interesting membrane separations of common gases (for instance O<sub>2</sub>/N<sub>2</sub>), we have been exploring the use of a small pore zeolite (zeolite A) in the form of a thin film. As shown bellow a significant selectivity is expected. Up to 5 atm N<sub>2</sub> at O<sub>2</sub> have a linear isotherm in zeolite A. Thus the permeability can be written:

$$P = D \cdot K \quad (6.1)$$

where K is the Henry coefficient and D is the diffusivity.

Using the values of K and D reported in reference 14 we calculate P. The values used and the estimated permeability are given in Table 6.1.

**Table 6.1.** Diffusivity and Henry coefficient for O<sub>2</sub> and N<sub>2</sub> in zeolite NaA from reference 14 and estimated permeabilities.

	K at 27°C mol/cm <sup>3</sup> /atm	D at 0°C m <sup>2</sup> /s	E <sub>act.</sub> for D kJ/mol	Permeability at 27°C cc(STP)-cm/cm <sup>2</sup> -min-atm
N <sub>2</sub>	332	2 x 10 <sup>-14</sup>	20	2.33 x 10 <sup>-7</sup>
O <sub>2</sub>	155	1.65 x 10 <sup>-12</sup>	24	7.60 x 10 <sup>-6</sup>

Thus at 27 °C the predicted selectivity for O<sub>2</sub> over N<sub>2</sub> is 33. For a 3 μm thick film of zeolite NaA, the expected O<sub>2</sub> permeance at 27 °C is .025 cc(STP)/min-atm-cm<sup>2</sup>.

Here we report the preparation of thin (<5μm) films of zeolite NaA on porous and non-porous substrates. Film evolution is monitored by X-ray Diffraction and Electron Microscopy and some aspects of the film formation mechanism are discussed.

## 6.2 EXPERIMENTAL

### 6.2.1 Synthesis of Zeolite NaA From a Clear Solution

Clear solutions were prepared according to the method described in reference (10). Aluminum foil (99.98%, Aldrich), NaOH (Aldrich) and sodium silicate solution (14%NaOH-27% SiO<sub>2</sub>, Aldrich), were used throughout this study. The sodium aluminate solution prepared was filtered in order to remove undissolved impurities contained in the aluminum foil (mainly iron) and then mixed under vigorous stirring with the sodium silicate solution. The clear solution composition was 10 Na<sub>2</sub>O- 0.2 Al<sub>2</sub>O<sub>3</sub>- 1 SiO<sub>2</sub>- 200 H<sub>2</sub>O. The reaction mixture was loaded into Teflon autoclaves and statically heated at temperatures ranging from room temperature to 70 °C in a constant temperature water bath. The resulting solid products were recovered by centrifugation (13,000 rpm for 1hour), washed with deionized water and dried in air at 70 °C before characterization.

### 6.2.2 Preparation of Supported Zeolite NaA Films

Growth of zeolite films was attempted on porous Al<sub>2</sub>O<sub>3</sub> disks (5cm diameter, Coors) and non-porous Al<sub>2</sub>O<sub>3</sub> disks (2cm diameter, Coors). During the initial experiments the substrate was placed vertically, inclined, or facing the bottom of the Teflon bottle containing the reaction mixture. The deposit layers accumulated on the substrate in these geometries were of variable thickness consisting of porous agglomerates, mainly due to incorporation of precipitated particles in the growing film. To avoid the incorporation of particles during film growth, the arrangement shown in Figure 6.1 was used for most of the experiments reported. The substrate was held horizontally and only one side was wetted by the reaction mixture. In some experiments the substrate was rotated with speeds of 1 to 45 rpm.

After a certain crystallization time the Teflon autoclave was removed from the heating bath and left to cool to room temperature. The substrate was then removed, washed thoroughly with deionized water, dried at 120 °C overnight and activated at 350 °C for 8 hours. A heating rate of 1 °C/min was used throughout drying and activation to avoid crack formation.

An attempt to prepare films of zeolite NaA by growing seeds of the zeolite deposited by filtration on a porous substrate (thin skin asymmetric Al<sub>2</sub>O<sub>3</sub> membranes, U.S. Filter) is described in detail at the *Results and Discussion* section.

### 6.2.3 Characterization

Solid products and films were examined by X-ray diffraction (XRD) using Cu-K<sub>α</sub> radiation on a Scintag XDS 2000 diffractometer, Scanning Electron Microscopy (SEM) on a CamScan electron microscope operating at 15 kV and Transmission Electron Microscopy

(TEM) using a Phillips 430 electron microscope operating at 200kV. For the XRD analysis of the supported films, the substrate was placed horizontally on the diffractometer stage with the film side exposed to the X-ray beam. For SEM the samples were coated with gold (~20 nm thick).

## 6.3 RESULTS AND DISCUSSION

### 6.3.1 *Synthesis of Zeolite NaA Powder From Clear Solution*

Figure 6.2 shows SEM micrographs of the solids collected after various times of hydrothermal treatment at 70 °C. In about 1 hour some turbidity was observed and after centrifugation the submicron particles shown in Figure 6.2a were collected. Gradually larger particles were formed and eventually a precipitated cake was observed at the bottom of the Teflon bottle. Figures 6.2a-f follow the evolution of the suspended particles from sub micrometer size to about 2  $\mu\text{m}$  size attained after 3 hours and 30 minutes in the autoclave. SEM micrographs of the precipitated cake formed after 8 hours and 35 minutes of crystallization are shown in Figure 6.3. The upper surface of the precipitate (exposed to the synthesis mixture) consists of spherical agglomerated particles (Figure 6.3a), while as one approaches the lower surface resting on the bottom of the autoclave, crystal facets and well developed cubic crystals are observed (Figure 6.3b-c). After 17 hours and 30 minutes of crystallization, almost all the particles have the appearance of fully developed crystals (Figure 6.3d).

In reference (11) it was claimed that using similar crystallization conditions unsupported zeolite NaA films were obtained. Our observations suggest that although continuous film structures are formed, they are of poor quality, in terms of variations in thickness and existence of interzeolitic porosity. Figure 6.4a shows SEM images of the lower surface after 10 hours and 30 minutes at 70 °C. A smooth surface is apparent but

with substantial interzeolitic porosity. Similar film-like deposits are occasionally observed forming on the vertical walls of the autoclave as reported in reference 11 but still with considerable interzeolitic porosity and variable thickness (Figure 6.4b).

The crystallinity evolution of the collected solids as followed by XRD is shown in Figure 6.5. A mixture of zeolite NaA and X-ray amorphous phase formed initially is succeeded by pure zeolite NaA. Even for the submicron particles shown in Figure 6.2a, collected immediately after turbidity is observed in the reaction mixture (1hour 15minutes at 70 °C), small peaks corresponding to zeolite NaA reveal the existence of crystalline phase. TEM of particles collected during the initial stages of crystallization reveals a mixture of submicron zeolite NaA and amorphous particles.

The above observations are consistent with zeolite NaA crystals nucleating in a previously formed amorphous phase. The growing zeolite crystals are initially surrounded by the amorphous phase which gives the spherical appearance to the collected solids. At the final stages of crystallization, the nutrients concentration in solution decreases, the formation of amorphous phase ceases and the transformation of the amorphous phase to zeolite NaA extends to the surface of the particles. At 70 °C the transformation from the amorphous phase to zeolite is so fast that one cannot collect completely amorphous solids even before any precipitation is observed. As the temperature of crystallization is decreased, precipitation of amorphous (by XRD and electron diffraction) solids is observed before any zeolite crystals appear. For instance, at room temperature after 2 days, an amorphous cake is formed before the appearance of zeolite. This can be explained considering the higher activation energy for crystallization compared to the activation energy for the precipitation of the amorphous phase.

### 6.3.2 *Film Preparation*

Based on the information presented above regarding crystal growth from a clear solution, the following two approaches for supported film formation were explored: film growth after deposition of zeolite seeds and in-situ growth.

#### 6.3.2.1 Film Growth After the Deposition of Seeds

After 3 hours of crystallization at 70 °C the suspension consisting of zeolite NaA-amorphous phase particles was filtered through a porous Al<sub>2</sub>O<sub>3</sub> membrane (U.S. Filter asymmetric Al<sub>2</sub>O<sub>3</sub> membrane with a thin skin of 50 Å pores) forming a loose cake which upon drying has the appearance shown in Figure 6.7a. The technique described in reference 12 was used to carry out this filtration. Subsequently the substrate with the deposited partially crystallized particles was immersed in a freshly prepared synthesis mixture and hydrothermally treated at 70 °C for 30 minutes. During that time the solution remained clear. The substrate was then removed from the solution, washed thoroughly with freshly prepared solution and reimmersed in fresh synthesis mixture for another 30 minutes treatment cycle. Several such cycles were repeated. Figure 6.7b-d shows SEM top views of the deposit. Even after 6 hours (12 cycles) at 70 °C, only partially crystallized particles are present on the surface of the film. Below the surface and towards the substrate-film interface, well crystallized particles were observed. Examination of deposit cross sections reveals that the layer thickness increased from 3 μm after filtration to 10-15 μm after 6 hours at 70 °C.

The above results suggest that the initially deposited particles crystallize further to zeolite NaA but the film thickness continues increasing due to additional deposition from the clear solution. This deposition cannot be eliminated even for the very short cycles of contact with the clear solution (30 minutes). As a result the films are relatively thick, not fully crystallized, and very often susceptible to cracks formed during activation. We need

to investigate the use of more dilute solutions for the growth cycles in order to suppress the nucleation rates from the clear solution and consequently slow down the additional deposition.

### 6.3.2.2 In-situ Film Preparation

#### *Growth on non porous substrates*

Using the arrangement shown in Figure 6.1, film growth on a non porous  $\text{Al}_2\text{O}_3$  substrate was first studied. Figure 6.8 shows XRD patterns obtained for disks treated for various times. Up to 2 hours no peaks other than those corresponding to the  $\alpha\text{-Al}_2\text{O}_3$  substrate are present. The morphology evolution of the deposited films as revealed by top view SEM micrographs is shown in Figure 6.8. An initial nucleation of small particles on the substrate is followed by the growth of a polycrystalline film consisting of intergrown zeolite NaA crystals. After 6 hours at 70 °C, a fully crystallized zeolite film is formed. Further hydrothermal treatment leads to the deposition of crystals of other zeolites (mainly faujasite) on top of the zeolite NaA layer. Cross section views are shown in Figure 6.9. Figure 6.9a shows the highly crystalline 3  $\mu\text{m}$  zeolite NaA film obtained after 6 hours at 70 °C. The thickness of the zeolite NaA layer does not change with additional hydrothermal treatment but a layer of large faujasite crystals starts to develop on top as shown in Figure 6.9b. If the substrate is immersed in the crystallizing solution after 5 hours of hydrothermal treatment only the large faujasite crystals are formed with further crystallization.

The zeolite NaA films when fully crystallized (after 6 hours at 70 °C) do not develop cracks upon drying and activation. Good adhesion to the substrate is demonstrated by a Scotch tape test and sonication. Both fail to induce any changes observable by SEM

(resolution 500 Å). On the contrary, partially crystallized films, during drying, develop cracks detectable by SEM.

In a few experiments the substrate was rotated during hydrothermal treatment. Three rotation speeds were used: 1, 6 and 45 rpm. In all cases zeolite NaA films were formed as revealed by the XRD patterns. The SEM micrographs are shown in Figure 6.10. The convective transport towards and along the substrate induces changes to the crystal morphology. The crystal size decreases with increasing speed of rotation, but film thickness remains the same for the rotation speeds used. The velocity profile of a fluid near a rotating substrate has been studied in the context of the rotating disk electrode (13 and references therein). The process is complicated here by the presence of suspended particles and the growing deposit. An extensive treatment requires more experimentation which has not been carried out. Nevertheless our results show that the flow field can have an effect on the morphology of zeolite crystals. The constant film thickness suggests that for the rotation speeds used, the particles that were convected towards the substrate could not be incorporated to the growing film and were eventually carried away to the solution.

Finally, the influence of temperature was examined. At lower temperatures the nucleating particles spent more time in the vicinity of the substrate before precipitation, therefore one expects a decreasing thickness with increasing temperature of crystallization. Three temperatures were used, 60, 70 and 90 °C. Indeed, the expected trend is observed. At 60 °C a 6 μm film of NaA is formed, at 70 °C the film thickness decreases to 3 μm, while at 90 °C the zeolite NaA deposit does not form a continuous film.

#### *Growth on porous Al<sub>2</sub>O<sub>3</sub>*

Similar films were developed on porous Al<sub>2</sub>O<sub>3</sub> (pore size 1 μm) using the arrangement of Figure 6.1. A SEM micrograph from the cross section of a zeolite NaA

alumina membrane is shown in Figure 6.11. A 3  $\mu\text{m}$  polycrystalline layer consisting of intergrown zeolite NaA crystals follows the roughness contour of the external surface of the substrate. A few zeolite crystals were observed at a depth up to 10  $\mu\text{m}$  inside the support. Permeability measurements of these asymmetric membranes will be reported in a future communication.

## **ACKNOWLEDGMENT**

Michael Tsapatsis is grateful to the North American Membrane Society for a NAMS Fellowship.

## REFERENCES

1. Jelinek, R., B. F. Chmelka, A. Stein and G.A. Ozin, "Multinuclear Magic-Angle Spinning and Double Rotation NMR of the Synthesis and Assembly of a Sodalite Semiconductor Supralattice," *J. Phys. Chemistry* **96**, 6744-6752 (1992).
2. Yan, Y.G. and T. Bein, "Molecular Recognition on Acoustic-Wave Devices - Sorption in Chemically Anchored Zeolite Monolayers," *J. Phys. Chem.* **96(23)**, 9387-9393 (1992).
3. Beer, R., B. Frank and G. Galzaferrri, "Photochemical Oxidation of Water on a  $1\mu\text{m}$   $\text{Ag}^+$  Zeolite Layer," *J. Photochem. Photobiol. A: Chem.* **69**, 67-72 (1992).
4. Suzuki H., "Composite Membrane Having a Surface Layer of an Ultrathin Film of Cage-Shaped Zeolite and Processes for Production Thereof," *US Patent* 4,699,892 (1987).
5. Geus, E.R., H. van Bekum, J.W. Baker and J. A. Moulijn, "High Temperature Stainless Steel Supported Zeolite (MFI) Membranes: Preparation, Module Construction and Permeation Experiments," *Microporous Materials* **1**, 131-147 (1993).
6. Bein, T., K. Brown and C.J. Brinker, "Molecular Sieve Thin Films from Zeolite Silica Microcomposites," in: Jacobs P.A., van Santen R.A. (Eds.), *Zeolites: Facts, Figures, Future*, Elsevier, Amsterdam (1989).

7. Tsapatsis, M., S. Kim, S.W. Nam and G.R. Gavalas, "Synthesis of Hydrogen Permselective SiO<sub>2</sub>, TiO<sub>2</sub>, Al<sub>2</sub>O<sub>3</sub> and B<sub>2</sub>O<sub>3</sub> Membranes from the Chloride Precursors," *I&EC Research* **30**, 2152-2159 (1991).
8. Tsapatsis, M. and G.R. Gavalas, "A Kinetic Model for Membrane Formation by CVD of SiO<sub>2</sub> and Al<sub>2</sub>O<sub>3</sub>," *AIChE Journal* **38**, 847-856 (1992).
9. Tsapatsis, M. and G.R. Gavalas, "Structure and Aging Characteristics of H<sub>2</sub>-permselective SiO<sub>2</sub>-Vycor Membranes," (accepted for publication *Journal of Membrane Science*).
10. Wenqin, P., S. Ueda and M. Koizumi, "The Synthesis of Zeolite NaA from Homogeneous Solutions and Studies of its Properties" in: Murakame Y., Iijima A., Ward A.W. (Eds.), *New Developments in Zeolite Science and Technology*, Kodansha, Tokyo (1986), p.177-184.
11. Myatt, G.J., P.M. Budd, C. Price and S.W. Carr, "Synthesis of a Zeolite NaA Membrane," *J. Mater. Chem.* **2(10)**, 1103-1104 (1992).
12. Okubo, T., K. Haruta, K. Kusakabe, S. Morooka and H. Anzai, "Preparation of a Sol-Gel Derived Thin Membrane on a Porous Ceramic Hollow Fiber by the Filtration Technique," *J. Membr. Sci.* **59(1)**, 73-80 (1991).
13. Bard, A.J. and R.L. Faulkner, *Electrochemical Methods. Fundamentals and Applications*, John Wiley and Sons (1980).

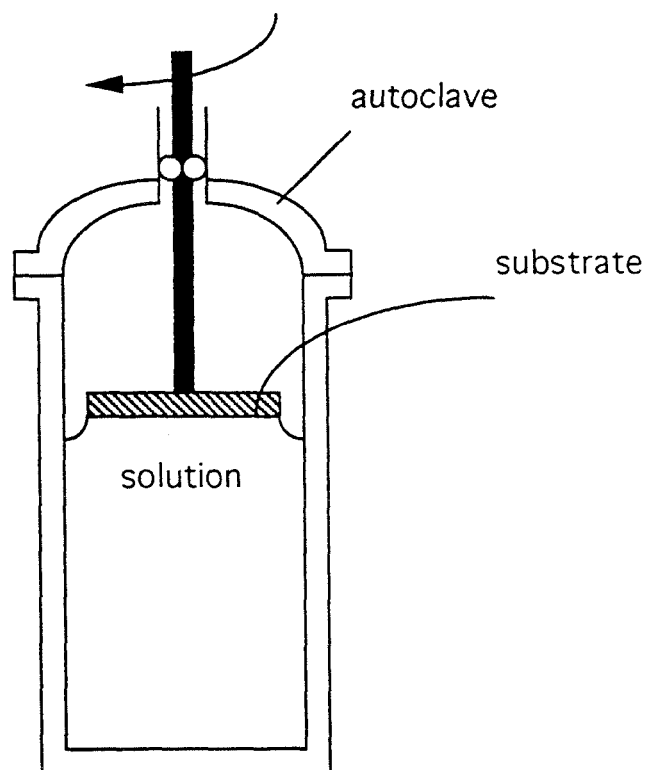


Figure 6.1 Schematic of the arrangement of the substrate and synthesis mixture for the development of zeolite NaA films on porous and nonporous substrates.

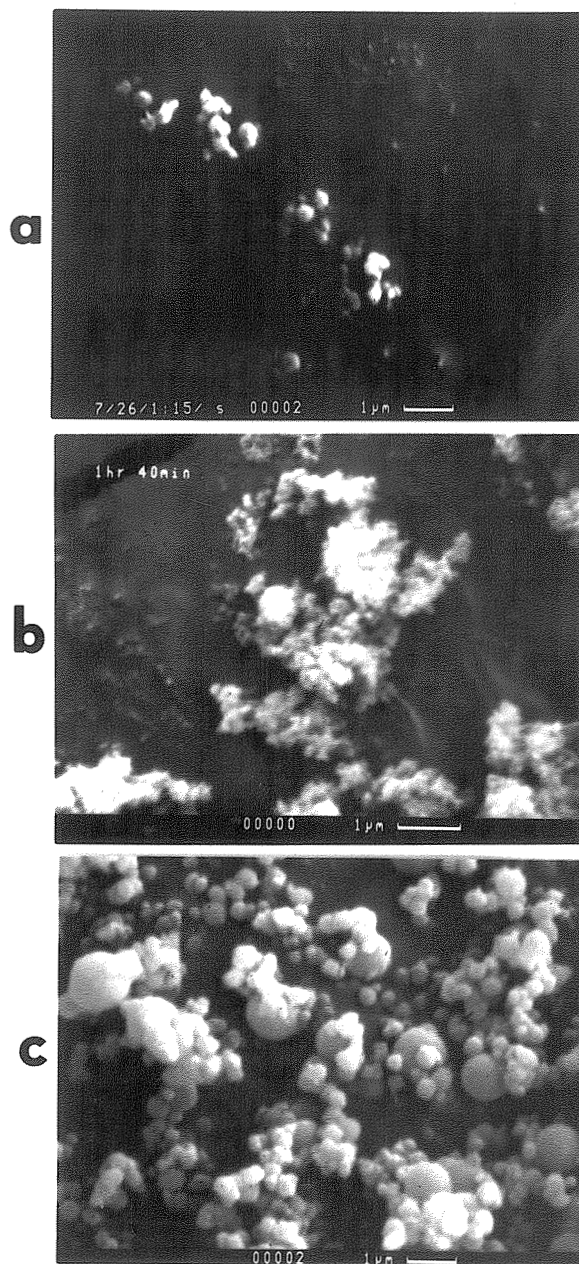


Figure 6.2 SEM micrographs of the particles collected after crystallization at 70 °C for: a, 1hr 15min; b, 1hr 40min; c, 2hrs 10min; d, 2hrs 45min; e, 3hrs; f, 3hrs 30min.

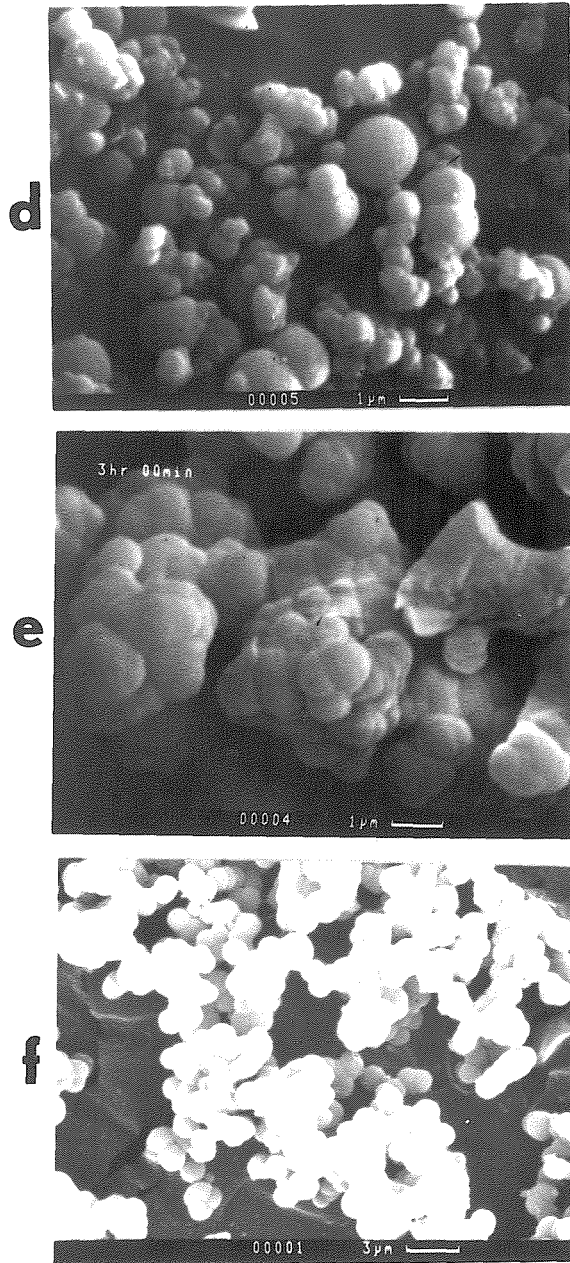


Figure 6.2 (cont.)

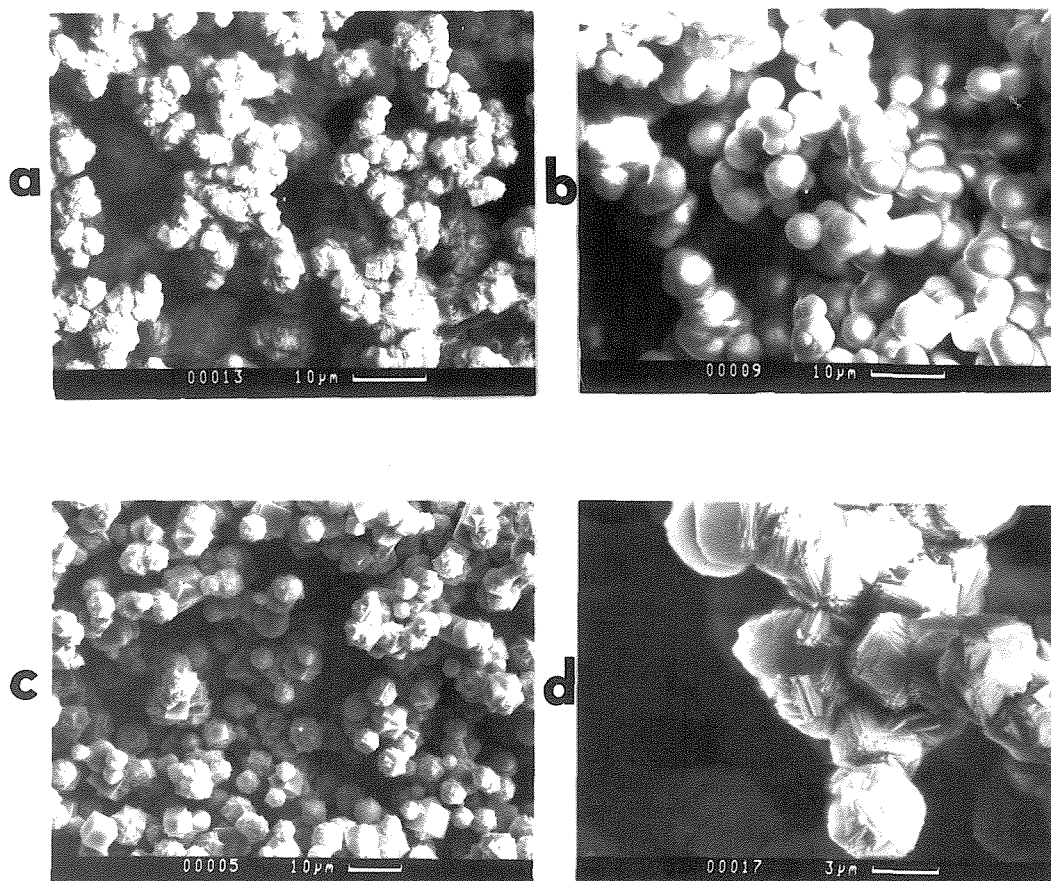


Figure 6.3 SEM micrographs of the precipitated cake after crystallization at 70 °C: **a**: 8hrs 35min, top view of the precipitate side facing the synthesis mixture (opposite to the Teflon bottle), **b**: 8hrs 35min, cross section 100 μm away from the top side, **c**: 8hrs 35min, bottom side, **d**: 17hrs 30min, top side.

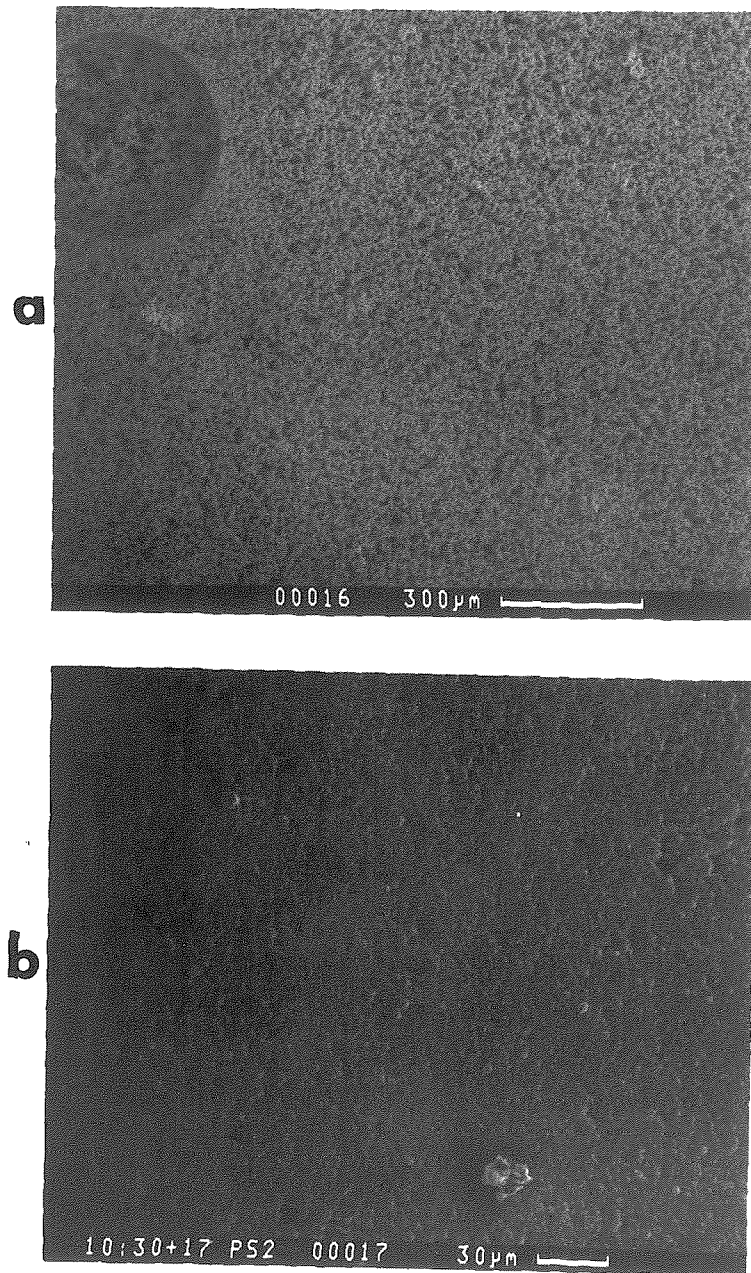


Figure 6.4 SEM micrographs of films of zeolite NaA formed after crystallization at 70 °C for 10hrs 30min: **a**: bottom side of the precipitated cake, **b**: film collected from the vertical walls of the Teflon vessel. The smooth side facing the Teflon wall is shown.

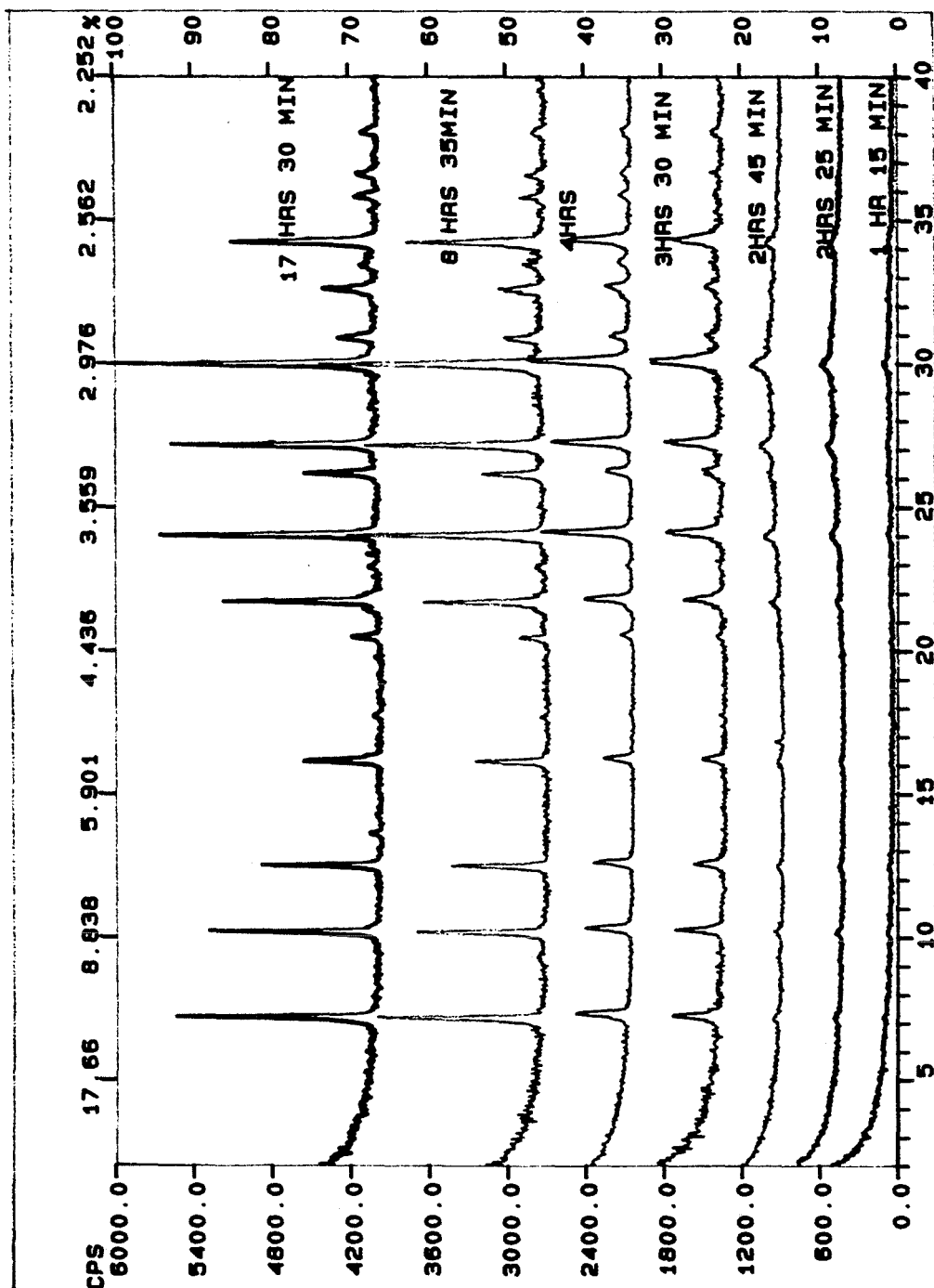


Figure 6.5 XRD patterns from the powder collected after crystallization at 70 °C for: 1hr 15min, 2hrs 25min, 2hrs 45min, 3hrs 30min, 4hrs, 8hrs 35min, and 17hrs 30 min (from the bottom to the top of the Figure).

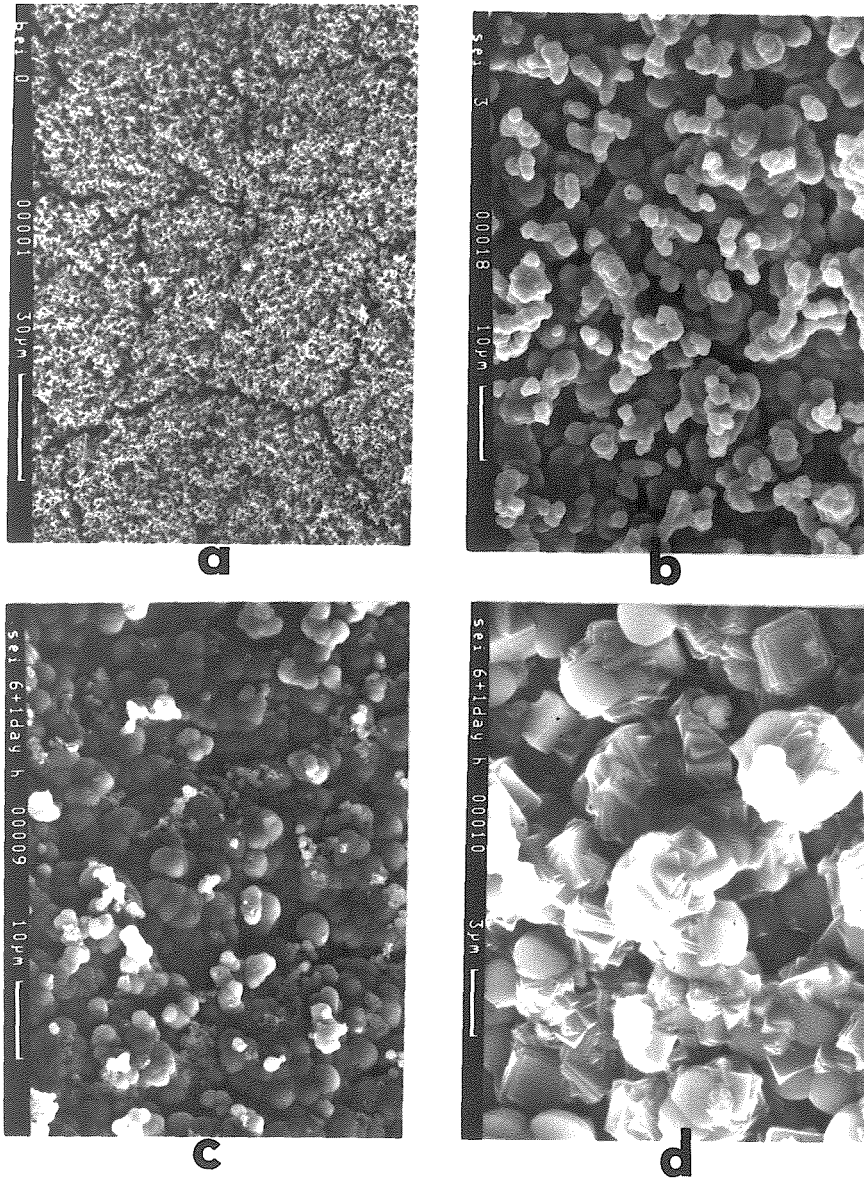


Figure 6.6 Top view SEM micrographs of film grown after deposition of seeds (see text): **a**: just after the filtration of suspended particles, **b**: after 6 30min cycles of contact with clear solution at 70 °C, **c**: after 12 30min cycles of contact with clear solution at 70 °C, **d**: deposit as in Figure 6.6c after scratching the top layer.

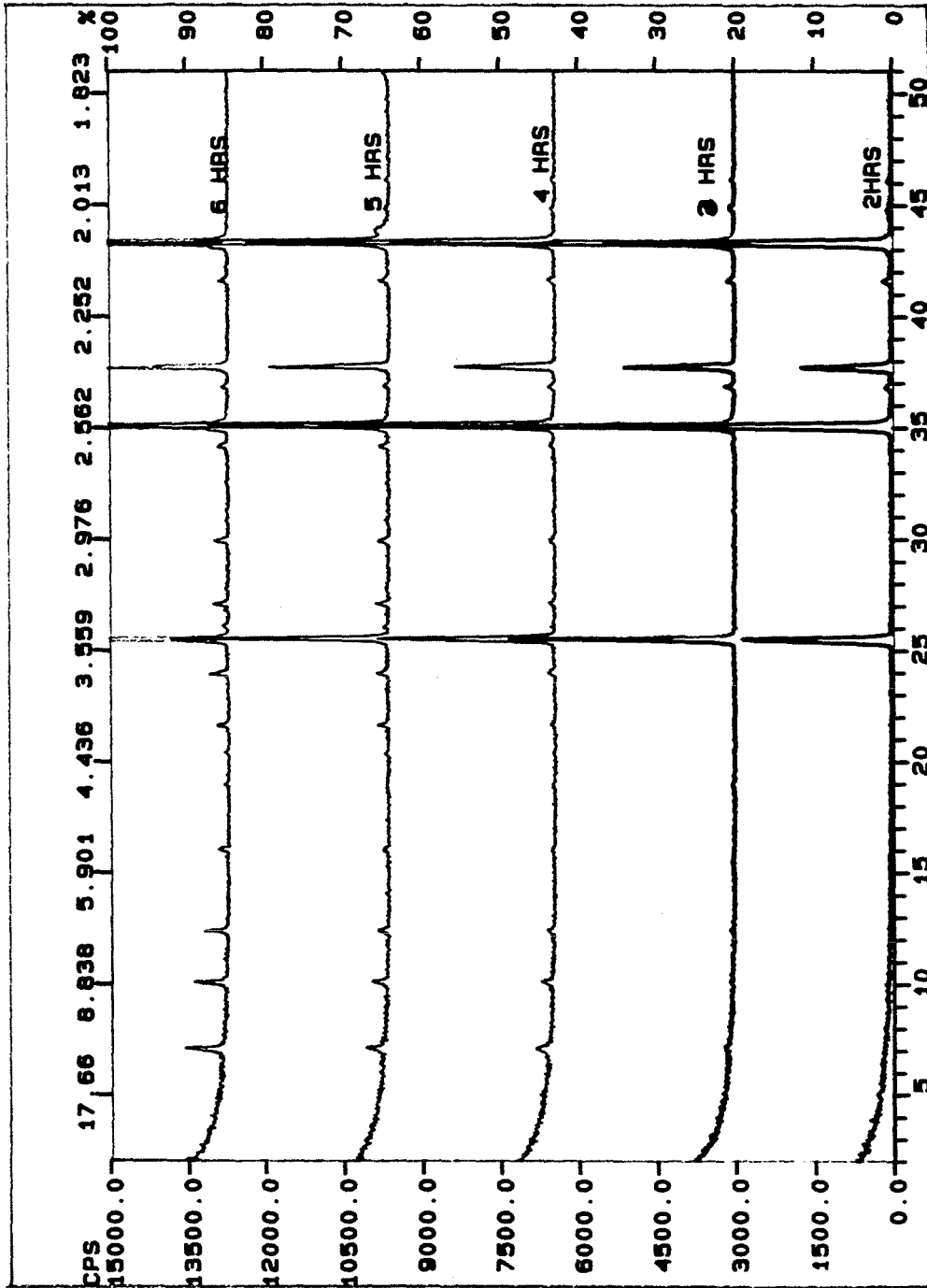


Figure 6.7 XRD patterns of  $\alpha$ - $\text{Al}_2\text{O}_3$  disks treated for various times at 70 °C in contact with the crystallizing solution in the arrangement shown in Figure 6.1. From bottom to top of the Figure: 2hrs, 3hrs, 4hrs, 5hrs, 6hrs.

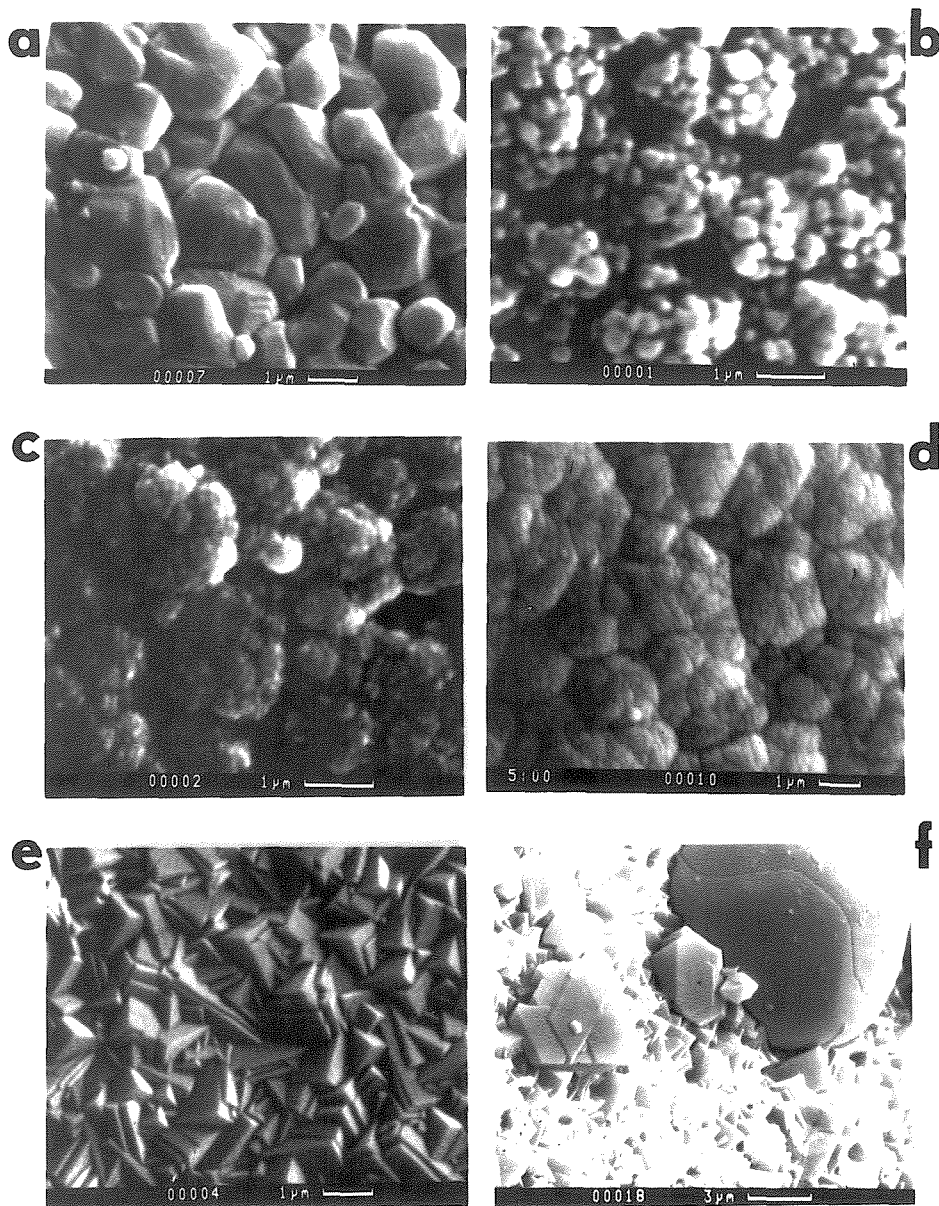


Figure 6.8 Top view SEM micrographs of deposits on  $\alpha$ - $\text{Al}_2\text{O}_3$  non porous disks after crystallization at 70 °C in the arrangement shown in Figure 6.1: **a**:  $\text{Al}_2\text{O}_3$  substrate, **b**: 2hrs 45min, **c**: 3hrs 30 min, **d**: 5hrs, **e**: 6hrs, **f**: 8hrs, **g**: lower magnification of (6.8.a), **h**: lower magnification of (6.8.e).

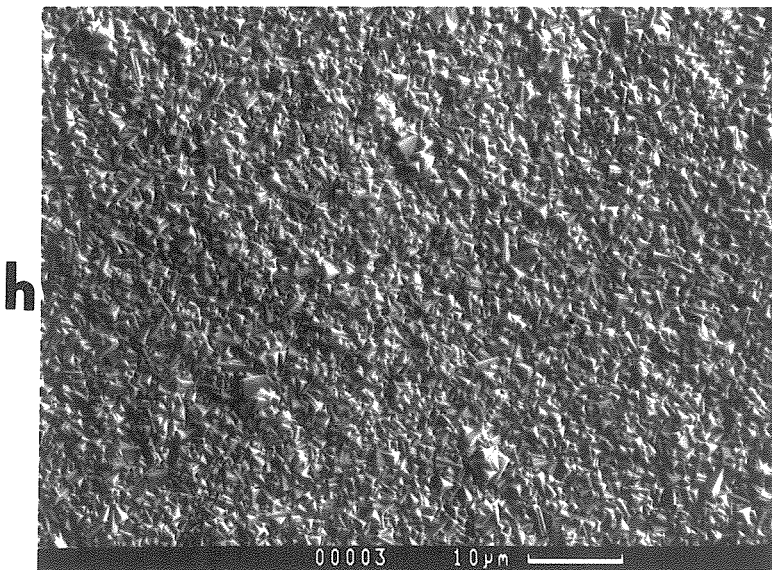
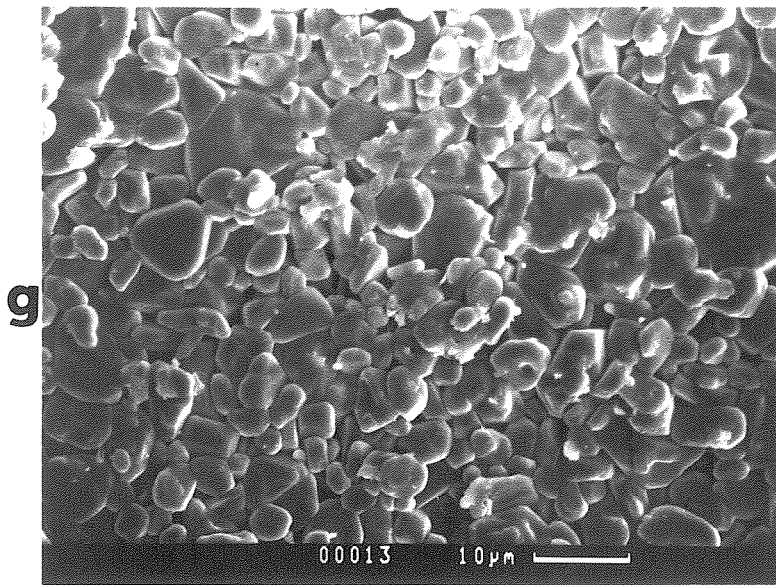


Figure 6.8 (cont.)

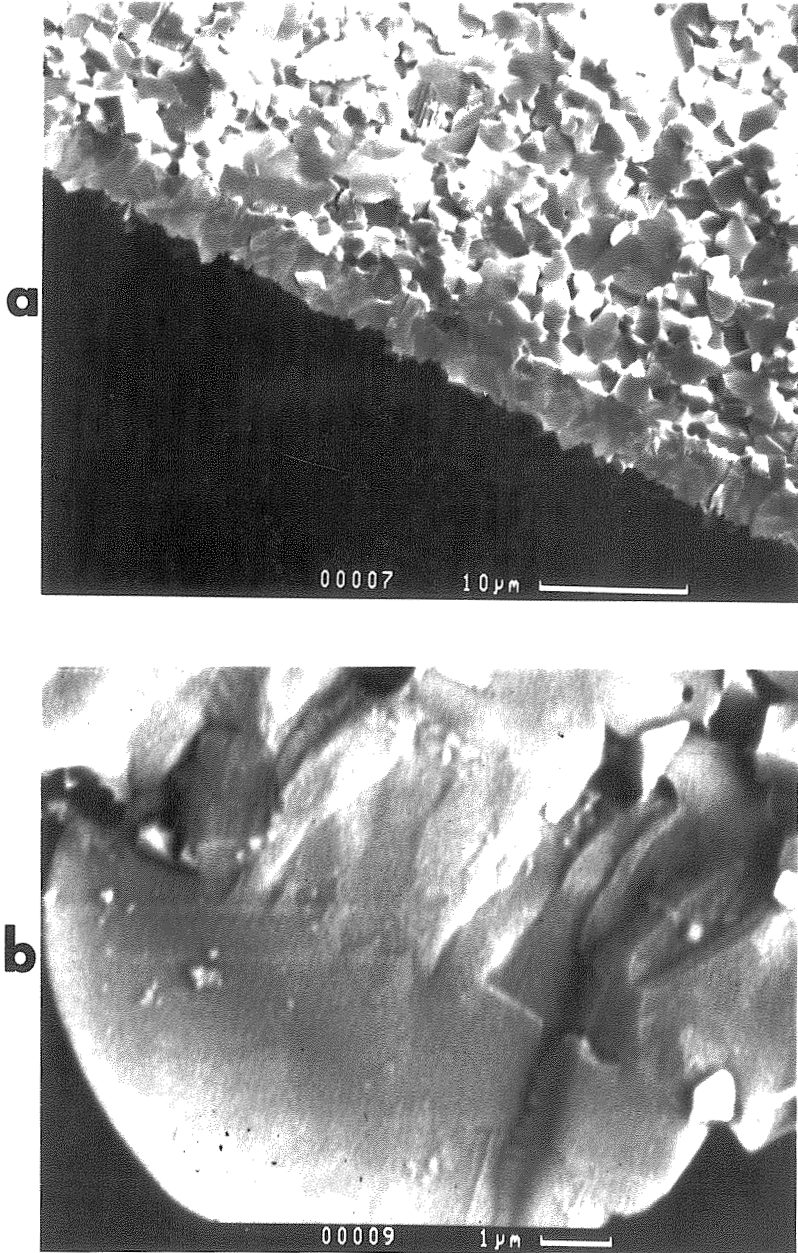


Figure 6.9 Cross section SEM micrographs of disks treated as described in Figure 6.8:

a: 6hrs, b: 8hrs.

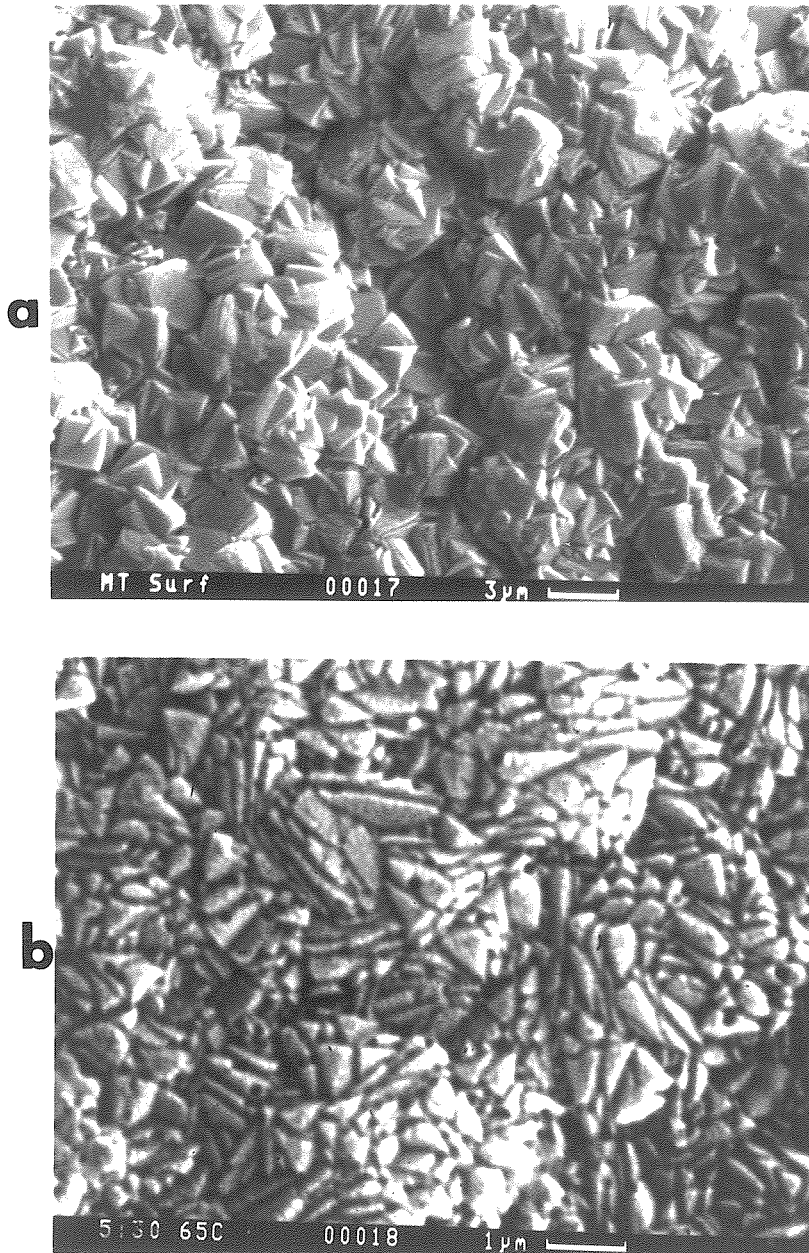


Figure 6.10 Top view SEM micrographs of films developed after 6hrs at 70 °C with rotation speed: **a**: 6 rpm, **b**: 45 rpm.

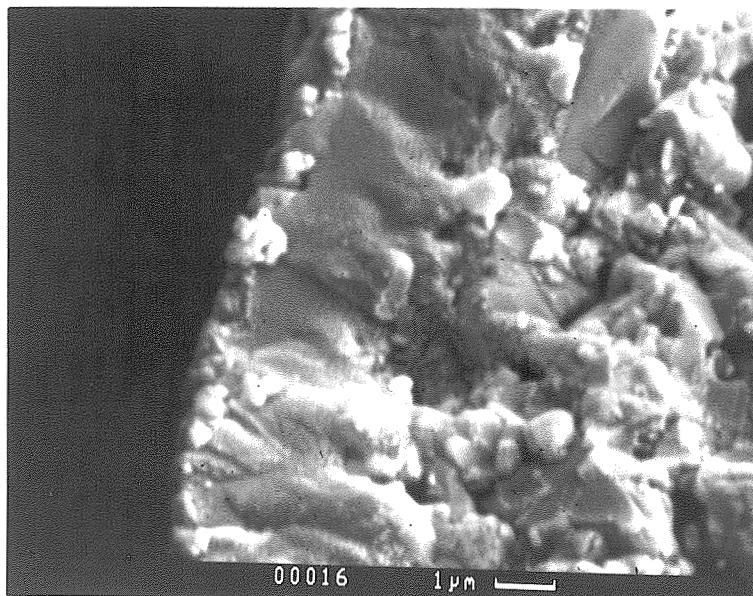
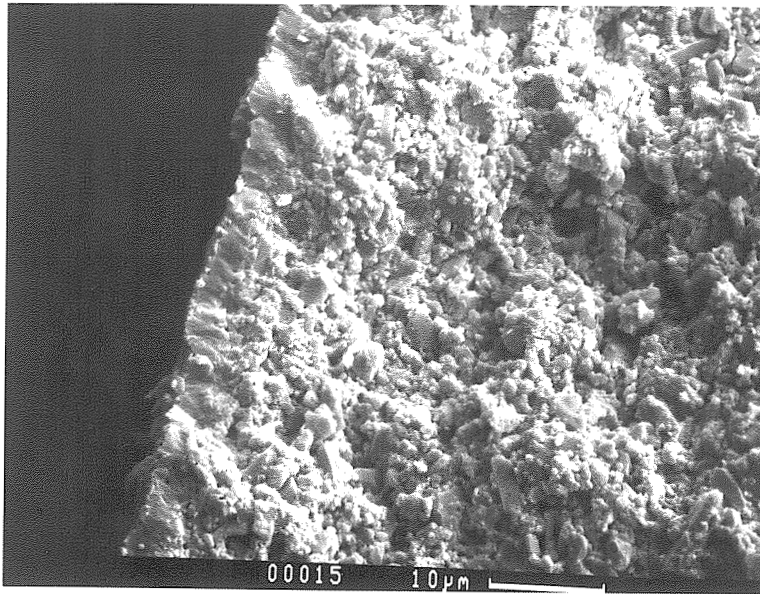


Figure 6.11 Cross section SEM micrograph of film developed on porous  $\text{Al}_2\text{O}_3$  after 7hrs at  $70\ ^\circ\text{C}$ .

## **CHAPTER 7**

### **Conclusions**

Hydrogen permeable membranes were synthesized by depositing layers of amorphous  $\text{SiO}_2$ ,  $\text{TiO}_2$ ,  $\text{Al}_2\text{O}_3$  and  $\text{B}_2\text{O}_3$  within the pores of Vycor tubes using the reaction of the respective chloride vapors ( $\text{SiCl}_4$ , etc.) with water vapor. Permselective  $\text{SiO}_2$  and  $\text{B}_2\text{O}_3$  layers could be formed in either the one-sided or the two-sided (opposing reactants) geometry, while within the range of conditions employed, titania and alumina membranes were obtained only in the opposing reactants deposition, the one-sided deposition failing to produce pore plugging.

A direct heterogeneous mechanism is responsible for the opposing reactants deposition of all four oxides. It also explains the one-sided deposition of  $\text{SiO}_2$ . However, the rapid homogeneous reaction between  $\text{TiCl}_4$  and  $\text{H}_2\text{O}$  or  $\text{AlCl}_3$  and  $\text{H}_2\text{O}$  seems to interfere with the one-sided deposition of  $\text{TiO}_2$  and  $\text{Al}_2\text{O}_3$ .

Membranes prepared by one-sided deposition have higher permeances. The permeances at  $450^\circ\text{C}$  were 0.3 and 0.1  $\text{cm}^3/\text{cm}^2\text{-min-atm}$  for  $\text{SiO}_2$  membranes produced in the one-sided and two-sided geometries respectively. The  $\text{H}_2:\text{N}_2$  permeance ratios were 500-5000. These permeances include the resistance of the Vycor tube wall as well as the resistance of the deposited layer. The membranes containing the other oxides have lower permeances.

Silica and alumina layers prepared in the opposing reactants geometry possess highly asymmetric shape. The deposit density increases gradually from the chloride side, passes through a maximum and steeply decreases to zero well before the water side. Pore plugging is attained at a nonzero void fraction, evidently due to a percolative interruption of connectivity.

The  $\text{SiO}_2$  deposit density in membranes developed using one-sided deposition is maximum in a region about 0.5  $\mu\text{m}$  thick adjacent to the bore surface and gradually declines

to zero within a depth of about 10  $\mu\text{m}$  from the surface. The thin region of maximum deposit density is responsible for permselectivity, for it essentially blocks the permeation of nitrogen and larger molecules while allowing substantial permeation of hydrogen. This region contains about 10% by volume trapped voids and as a result has relatively high permeability as suggested by percolation theory.

Annealing at high temperatures causes densification of the deposited material as evidenced by increased activation energy for  $\text{H}_2$  permeation and correspondingly reduced permeance. The presence of  $\text{H}_2\text{O}$  vapor accelerates the densification process. The densified membranes had an  $\text{H}_2$  permeance as high as  $0.1 \text{ cm}^3(\text{STP})/\text{min-atm-cm}^2$  at  $500^\circ\text{C}$  and a  $\text{H}_2/\text{N}_2$  permeance ratio above 500.

When the deposit was confined inside the pores of the Vycor substrate, the membranes were mechanically stable, but when it extended substantially outside of the porous matrix the stresses induced by thermal cycling led to crack formation and propagation.

A mathematical model describing the deposition process has been developed. A deposition mechanism suggested from previous studies has been adopted involving reaction of the gaseous chloride with silanol groups on the surface and reaction of water vapor with chloride groups of the surface. Inaccessibility of surface groups due to deposit growth has been introduced into the model by assuming a maximum number of surface species per surface area exposed to gas reactants. The transient kinetics associated with these reactions were introduced into a continuum model describing diffusion and pore closure making use of percolation theory concepts. The model is capable of generating deposit profiles in good agreement with the experiment and predicting times of deposition required for pore plugging. It was found that for typical deposition conditions the connectivity evolution of the microporous substrate influences the time for pore plugging and the deposit thickness at the region of maximum deposition but not the position of the

deposit. It was also shown that in order to describe the heterogeneous deposition reaction in the microporous Vycor substrate, it is necessary to use the transient kinetics. The pseudosteady state approximation for surface species is not valid.

The growth of zeolite NaA films on various inorganic substrates from a clear solution with composition  $10 \text{ Na}_2\text{O}-0.2 \text{ Al}_2\text{O}_3-1\text{SiO}_2-200 \text{ H}_2\text{O}$  was followed by XRD, SEM and TEM. Deposition geometries and conditions are identified for the development of uniform polycrystalline thin ( $<5\mu\text{m}$ ) films consisting of intergrown crystals of zeolite NaA on porous and nonporous  $\text{Al}_2\text{O}_3$  disks. The films exhibit high crystallinity good adhesion to the substrate and thermal stability. The deposition technique demonstrates potential for developing molecular sieve membranes.